May 2019

Determination of Scatter Fractions, Albedos, and Tenth Value Layers for Shielding of Synchrotron Beamline Hutches

Bethany Lynn Broekhoven
Louisiana State University and Agricultural and Mechanical College, bbroek1@gmail.com

DETERMINATION OF SCATTER FRACTIONS, ALBEDOS, AND TENTH VALUE LAYERS FOR SHIELDING OF SYNCHROTRON BEAMLINE HUTCHES

A Thesis

Submitted to the Graduate Faculty of the
Louisiana State University and
Agricultural and Mechanical College
in partial fulfillment of the
requirements for the degree of
Master of Science

in

The Department of Physics and Astronomy

by
Bethany Lynn Broekhoven
B.S., Louisiana State University, 2013
August 2019

This work is dedicated to my parents, sister, and husband,

who have always supported and encouraged me in all of my endeavors.

Acknowledgments

Foremost, I acknowledge William Donahue for his GEANT4 expertise, which was essential to this project. Conversations with him about my work were invaluable. Additionally, I am grateful to Joseph Steiner and Krystal Kirby for laying some of the initial groundwork for this project with Dr. Matthews.

To my graduate advisory committee members: Thank you for all of the time and effort you have contributed to me during the course of my research. It is because of this my thesis project is as successful as it is. I particularly want to acknowledge Dr. Kenneth (Kip) Matthews II, chair of my graduate committee, for all of his invaluable guidance and knowledge he has imparted upon me during my graduate career and Drs. Wei-Hsung Wang, Robert Carver, and T. Gregory Guzik for their feedback and suggestions concerning my thesis.

To the faculty and staff of the LSU medical and health physics program: Thank you for making my graduate career a valuable one by teaching me the knowledge needed to receive an excellent education and the professional skills desired for my future career. Because of your dedication to me as a student, I will be prosperous in all of my future career endeavors.

To my fellow LSU medical and health physics peers: Thank you for the numerous educational discussions and social interactions during my graduate years at LSU.

To my family: Thank you for all of the unconditional love and support you have given me throughout the years. Your love and support is what has gotten me to where I am today.

This work was supported in part by a graduate fellowship from the Nuclear Regulatory Commission.

Table of Contents

Abstract

Synchrotron facilities require substantial amounts of shielding to protect facility staff and researchers. To meet mandatory exposure limits, the traditional combination of time, distance, and shielding of the radiation source are utilized. Because of continuous 24-7 operation of most synchrotrons, time is the least useful tool. The experimental stations for synchrotron x-ray beamlines, called hutches, enforce a minimum distance from the source, but shielding provided by hutch walls is still the principal tool for a synchrotron facility. Currently there is no single resource for synchrotron beamline hutch shielding design in the literature; most hutch shielding is designed through either over-simplified calculations or complex simulation models. The goal of this project is to produce data of scatter fraction, albedos, and tenth value layers (TVLs) for typical scattering and shielding materials that allows for an NCRP-style calculation of shielding requirements for synchrotron beamline hutches; NCRP-style calculation refers to the style of shielding calculations used in NCRP Report No. 151. In GEANT4, a typical beam geometry, scattering object, and shielding materials were modeled. A solid block of material (concrete, lead, or steel) was used to determine TVLs for primary and secondary radiation as well as albedos, while a disc of water was used to determine scatter fractions, all for primary beam energies from 10 keV to 100 keV. Because of the strong polarization of synchrotron light, x-ray scattering and albedo were substantially directed towards the ceiling and floor, rather than through the hutch's walls, except for x-ray energies above the K-edge of lead, where fluorescence x-rays contributed substantially to albedo. Lastly, the TVLs of shielding materials for primary and secondary radiation tracked as expected with x-ray energy, with a noticeable change in magnitude when crossing a material's K-edge.

Chapter 1. Introduction

1.1. Motivation

For over a century, the use of radiation has helped to increase our knowledge of the world around us. Shortly after the first use of radiation in the scientific community, the harmful effects of radiation to humans were noted. Because of this, the first radiation limits were put in place to limit exposure of radiation to the general public and to people working with radiation, known as radiation workers. These radiation limits have continued to evolve over the years as our understanding of radiation and its effects on the human body grew. The current radiation limits in the United States are 50 mSv/yr for radiation workers and 1 mSv/yr for the general public (NCRP 1993).

Radiation exposure can be moderated by controlling the amount of time one is exposed to the radiation source, the distance between the one exposed and the radiation source, and the amount of shielding between the one exposed and the radiation source. It follows that less time one spends in the vicinity of a radiation source lessens the dose that the person receives. The intensity of radiation falls off as the inverse square law. Increasing the distance between the radiation source and the exposed person reduces the radiation intensity. Shielding material placed between the radiation source and the exposed person reduces the radiation intensity by attenuating some radiation. The effectiveness of the shielding material between a person and a radiation source depends on the radiation type, radiation energy, and shielding composition and thickness.

In simple situations, straightforward calculations can be used to determine what amount of shielding is needed to reduce the radiation intensity to a safe limit. However, few situations are simple. Complex situations may have multiple sources of various radiation types, with limitations for utilizing time and distance that complicates the placement of shielding materials, like the

shielding of a nuclear reactor or a particle accelerator. For instances like this, the National Council on Radiation Protection & Measurements (NCRP) has produced guidelines for shielding calculations. Some examples of these reports are NCRP Report 144: Radiation Protection for Particle Accelerator Facilities, NCRP Report 147: Structural Shielding Design for Medical X-Ray Imaging Facilities, and NCRP Report 151: Structural Shielding Design and Evaluation for Megavoltage X- and Gamma-Ray Radiotherapy Facilities. These reports contain calculation guidelines and relevant radiation physics data for their specific situations. Typical data includes scatter fractions for typical object materials, albedos for typical shielding materials, and attenuation coefficients, usually characterized by tenth value layers (TVLs), for typical shielding materials.

One area lacking these specific data resources for shielding design is synchrotron beamline hutches. In these instances, either overly-simplified calculations or simulations are done to determine how much shielding material is needed; simplified calculations typically overestimate how much shielding material is required to ensure staying within the radiation limit. The goal of this project is to fill this gap in knowledge by generating data of scatter fractions, albedos, and TVLs that will allow for an NCRP-style method for shielding calculations for synchrotron beamline hutches. Specific aims to address this goal are described in the following section. Subsequent sections then review pertinent details about synchrotron accelerators and radiation interactions.

1.2. Specific Aims

The first specific aim was to determine scatter fractions from a typical beamline target for primary beam energies between 10 keV and 100 keV. A scatter fraction is the fraction of the

primary beam's absorbed dose that scatters from the target at a particular direction from the incident beam (NCRP 2005).

The second specific aim was to determine albedos for concrete, lead, and steel for primary beam energies between 10 keV and 100 keV. Albedo is defined as the proportion of the incident radiation that is reflected in a particular direction from the surface of a barrier (NCRP 2005).

The third specific aim was to determine primary TVLs for concrete, lead, and steel as well as secondary TVLs for lead and steel for primary beam energies between 10 keV and 100 keV. A primary TVL is the thickness of material needed to reduce the primary beam's original intensity to one-tenth of its initial value, while a secondary TVL is the thickness of material needed to reduce scattered radiation intensity to one-tenth of its initial value.

Figure 1.1. illustrates the typical layout of a synchrotron beamline hutch as well as what these shielding parameters visually represent. The blue arrows are primary beam particles that scattered within the target, contributing to scatter fractions while the green arrows are primary beam particles that reflected from the primary barrier, which are used to determine albedos for a primary barrier material. The primary barrier attenuates the remaining primary beam to an acceptable level, while the secondary barriers attenuate the scattered and reflected (secondary) radiation.

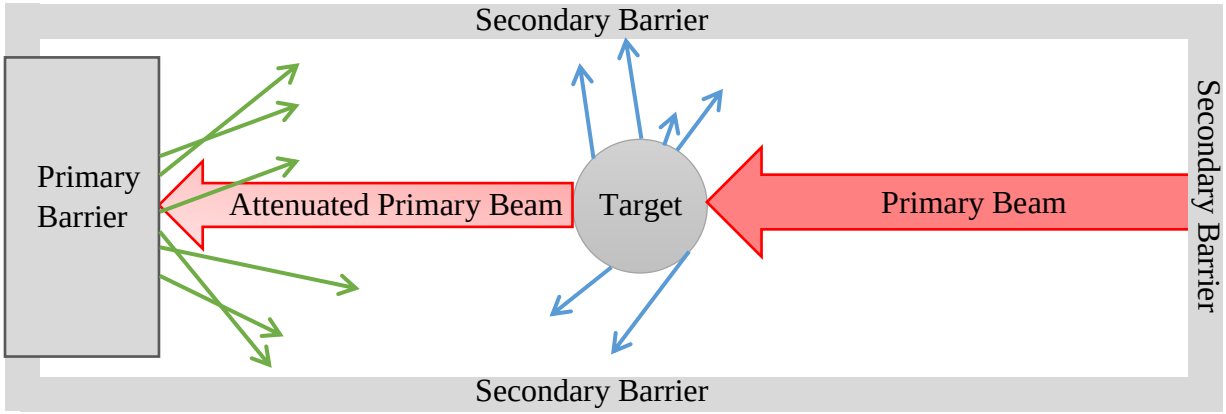

Figure 1.1. Overhead view of a typical synchrotron beamline hutch.

1.3. Synchrotron Accelerator

Synchrotron light sources consist of three main components, an injector, a storage ring, and beamlines. The injector is typically composed of one or more electron accelerators, which initially accelerates bunches of electrons for insertion into the storage ring. Once the electrons reach the end of the injector, they are injected into the ring and then accelerated further to the synchrotron's operating energy. In the storage ring, the electrons travel in a pseudo-circular path. The storage ring contains multiple straight sections connected by curved sections. These curved sections are made up of bending magnets, while insertion devices such as wigglers or undulators occupy some straight sections. These devices accelerate the electrons in the storage ring, causing synchrotron radiation, also known as synchrotron light, to be emitted tangentially to the electron beam's path. The synchrotron light then travels to experiment end-stations along beamlines to be used in scientific research. (NCRP 2003)

Synchrotron radiation is emitted by particles that undergo acceleration, such as when caused to travel in a circular path by a magnetic field in an accelerator (Cember 2009). Each time the beam passes through a bending magnet or an insertion device, a small fraction of its energy is radiated away (Knoll 2010). This radiation appears as an intense and highly directional beam of photons with energies ranging from a few eV (visible light) to hundreds of keV (Knoll 2010). For experimental uses, this radiation is directed toward experimental areas, or beamline hutches, by beamlines that are tangential to the storage ring (NCRP 2003). While some beamlines use a wide range of the radiation's energy spectrum for experiments, many beamlines use a nearly monoenergetic beam. These pseudo-monoenergetic beams, which have a very high intensity, are created using monochromators (Knoll 2010).

1.4. Radiation Interactions

Multiple types of radiation interactions can occur among particles. However, for synchrotron beamlines, which consist of photons that have energies from a few eV to a few hundred keV, only three types of radiation interactions are of concern. These three interactions are the photoelectric effect, Compton scattering, and Rayleigh scattering. (Attix 1986)

In the photoelectric effect, a photon interacts with an atom and ejects one of its orbital electrons as demonstrated in Figure 1.2. During the interaction, all of the photon's energy is absorbed by the atom and then transferred to an orbital electron. The energy of the photon is typically transferred to an inner shell orbital electron and the kinetic energy of the ejected electron is equal to the photon's initial energy, hv, minus the binding energy of the electron, E_B, in the atom; to be ejected, an orbital electron's binding energy must be less than or equal to the energy of the photon. The ejected electron leaves behind a vacancy in the atom's orbital shells, consequently putting the atom into an excited state. For the atom to de-excite, an electron from one of the outer orbital shells drops into the vacancy while emitting a fluorescence (or characteristic) x-ray. The energy of the fluorescence x-ray is equal to the difference of the binding energies between the orbital shell with the vacancy and the orbital shell from which the donor electron came. Additional fluorescence x-rays can occur as the vacancy sequentially travels to the outer-most electron shell. (Attix 1986, Khan 2014, and Cember 2009)

An alternative to fluorescence emission is Auger electron emission. The excitation energy of the atom (with an orbital vacancy) is used to eject another orbital electron with some kinetic energy. Overall, the process is to create two lower-excitation outer shell vacancies from a single higher-excitation inner-shell vacancy.

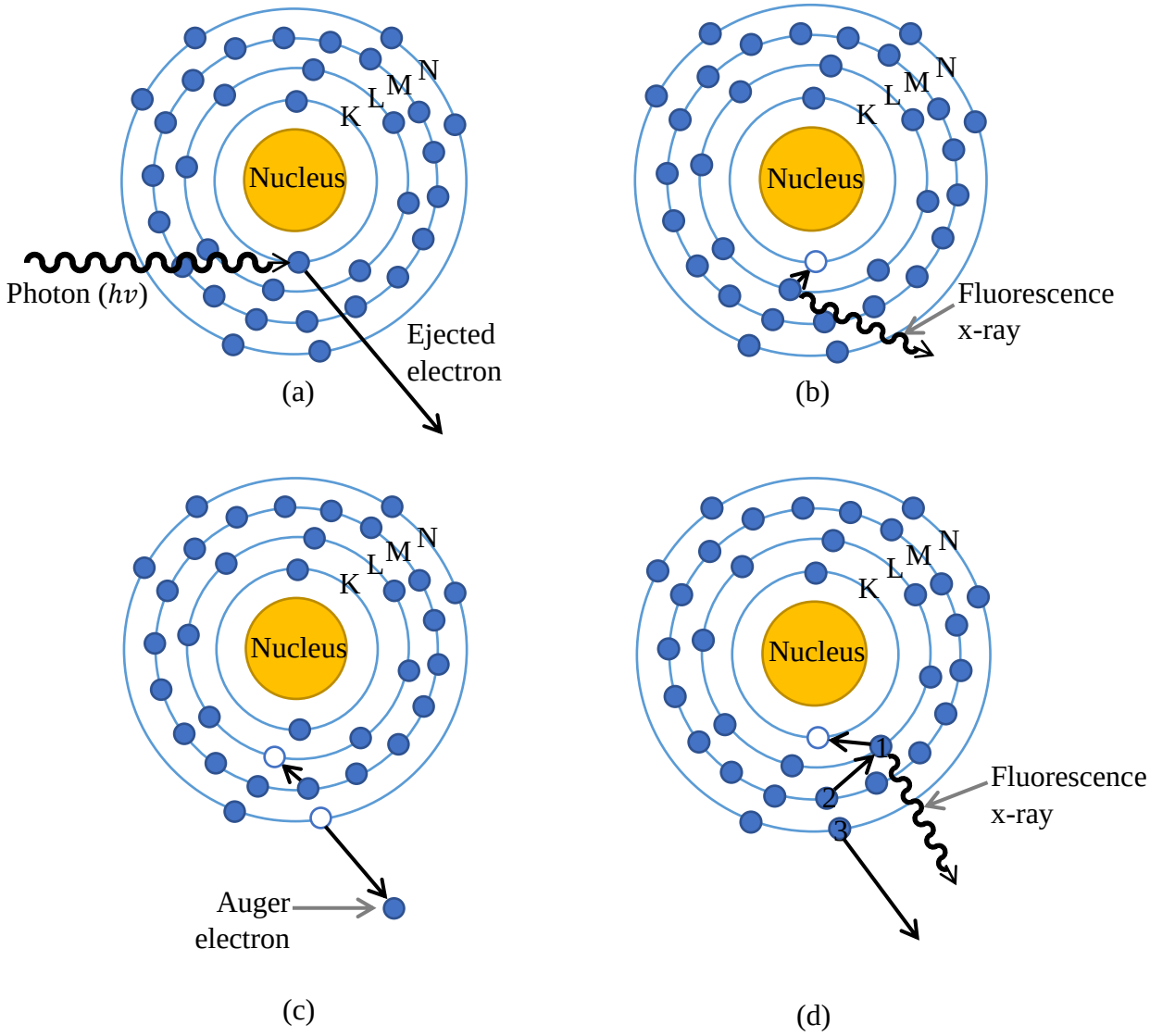

Figure 1.2. (a) A photon with energy, hv, is absorbed by an atom and its energy is transferred to a K-shell electron which is then ejected. (b) Fluorescence emission can then occur when an outer shell electron relocates to the inner shell to fill the vacancy causing a fluorescence x-ray to be produced. (c) Alternatively, Auger emission (a competitive process to fluorescence emission) can occur when an atom uses its excitation energy to fill its inner shell vacancy with an outer shell electron and eject an additional electron, an outer shell electron with respect to the vacancy's new position, to remove the remaining excitation energy. (d) Fluorescence and Auger emission can occur in tandem to de-excite an atom. In this figure, the photoelectric effect has created a vacancy in the K-shell. The electron labeled "1" moves from the L-shell to the K-shell and causes a fluorescence x-ray is emitted. With the vacancy now in the L-shell, the electron labeled "2" moves from the M-shell to the L-shell. Instead of emitting an additional fluorescence x-ray, this time the excitation energy is used to overcome the N-shell binding energy and eject the electron labeled "3"; upon ejection, the electron is known as an Auger electron. These processes will continue to occur while the orbital vacancies migrate to the outer most shells of the atom.

The binding energy of each electron orbital shell corresponds to an absorption edge. These absorption edges appear as discontinuities in a graph of interaction probability for the photoelectric effect plotted against the photon's energy. When a photon has an energy that just equals or just exceeds an orbital shell's binding energy, the probability of photoelectric absorption increases drastically. Hence, a material becomes a better absorber at a photon energy just above the material's orbital binding energy. (Khan 2014)

In Compton scattering, illustrated in Figure 1.3., a photon interacts with an outer shell electron. When the photon interacts, the photon transfers a portion of its energy to the electron and is scattered at an angle ϕ_p relative to the path of the incident photon and the electron is emitted from the atom at an angle θ_e (Khan 2014). The incident and scattered energies, ϕ_p, and θ_e (plus the residual electron binding energy) are all closely interrelated (Khan 2014). Unpolarized photons undergoing Compton scattering show an azimuthal symmetry and can be tabulated by a single Compton scatter angle, i.e. ϕ_p (Attix 1986). However, polarized photons undergoing Compton scattering require both an azimuthal angle, ϕ, and a polar angle, θ, to specify the scatter direction. The scatter directions of polarized photons are biased perpendicular to the polarization vector (Section 3.2). To find the Compton scattering angle, η, of a polarized photon relative to the direction of travel of the incident photon (i.e., $\phi = 0°$ and $\theta = 0°$ for the incident photon), first convert spherical coordinates to Cartesian coordinates:

$$x = \cos\phi \sin\theta \qquad \text{[Eq. 1]}$$

$$y = \sin\phi \sin\theta \qquad \text{[Eq. 2]}$$

$$z = \cos\theta \qquad \text{[Eq. 3]}$$

Then find the Compton scattering angle, η, using the following formula:

$$\eta = \cos^{-1}\left(\frac{z}{\sqrt{x^2+y^2+z^2}}\right) \qquad \text{[Eq. 4]}$$

Rayleigh scattering, also shown in Figure 1.3., is when the photon is redirected through a small angle with its original energy. This is because the photon is scattered by the combined action of the atom as a whole. The atom moves just enough to conserve momentum. (Attix 1986)

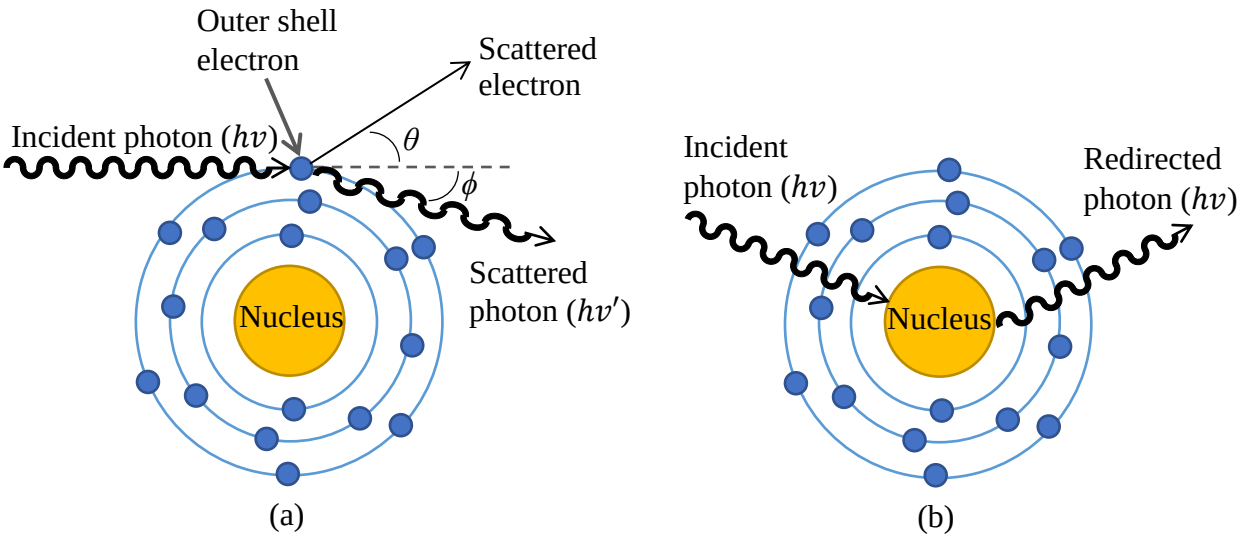

Figure 1.3. Illistration of Compton scattering (a) and Rayleigh scattering (b).

Chapter 2. GEANT4 Shielding Simulations

GEANT4 is a Monte Carlo simulation toolkit (Agostinelli *et al*. 2003), which was used to assist in the evaluation of shielding parameters needed for shielding of synchrotron beamline hutches. The shielding parameters calculated using GEANT4 simulations were scatter fractions, albedos, and both primary and secondary TVLs.

To assess the values of these shielding parameters, a beam of polarized photons was simulated entering a synchrotron beamline hutch and interacting with a target. Two types of simulation models were used in GEANT4 to determine the shielding parameters. These two models are known as the scatter setup (Section 2.1) and attenuation setup (Section 2.2).

Simulation runs were performed for beam energies between 10 keV and 100 keV in 5 keV increments. Each simulation transported one billion polarized photons with a polarization angle perpendicular to the beamline as seen in Figure 2.1. Each simulation was divided into ten smaller runs of one hundred million photons each. Initial random seeds were generated using the C++ standard library random_device utility for each run, to ensure there was no duplication. A list of the simulation runs performed to determine the shielding parameters is found in Appendix A.

Version 10.4 of GEANT4 was used for the simulations. This version enabled parallel processing, also known as multithreading, which allowed the simulation to use multiple computer cores, therefore resulting in reduced computing time (Dong *et al.* 2010). The G4EmLivermorePolarizedPhysics list was used to model the physical interactions during transport. This physics model supports the transport of polarized photons. Table 2.1. lists the physics parameters whose default values were modified for the simulations.

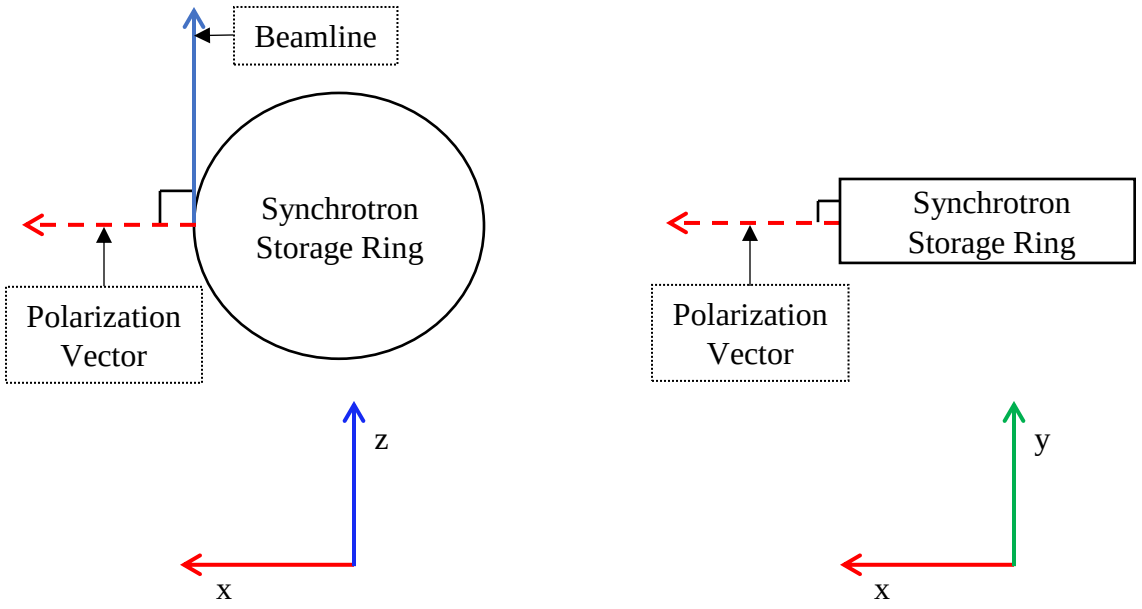

(a) (b)

Figure 2.1. (a) Simplified top down view of a synchrotron storage ring and beamline showing the orientation of the polarization vector in the GEANT4 simulations. (b) Simplified edge on view of a synchrotron storage ring again showing the polarization vector. Note the xyz axes are labeled and color coded to agree with the xyz axes found in Figure 2.2.

Table 2.1. GEANT4 parameters used in simulation runs.

Parameter Name	Value	Description
BinsPerDecade	31	Number of electron stopping power table entries spaced logarithmically
MinEnergy	100 eV	Minimum energy of interaction cross section and stopping power tables
MaxEnergy	500 MeV	Maximum energy of interaction cross section and stopping power tables
Photon Cut length	0.001 mm	Blocks creation of photons with radiation length less than value
Electron Cut Length	0.001 mm	Blocks creation of electrons with range less than value
Position Cut Length	0.001 mm	Blocks creation of positrons with range less than value

2.1. GEANT4 Scatter Setup

The scatter setup model allowed for the scatter fractions from a typical beamline target of various primary beam energies to be determined. Figure 2.2. shows the scatter setup in GEANT4. The world volume is a 3 m x 3 m x 3 m cube in which the target, a disc of water with a radius of

6 cm and height of 2 cm, is centered at x = 0 cm, y = 0 cm, and z = 0 cm. The dimensions of this disc were chosen so that the target would be large enough to induce scattering of the primary photons, but also small enough that the target did not substantially self-attenuate the scattered photons. The material of the disc was chosen as water, as a surrogate for typical samples used in microtomography or radiobiology research.

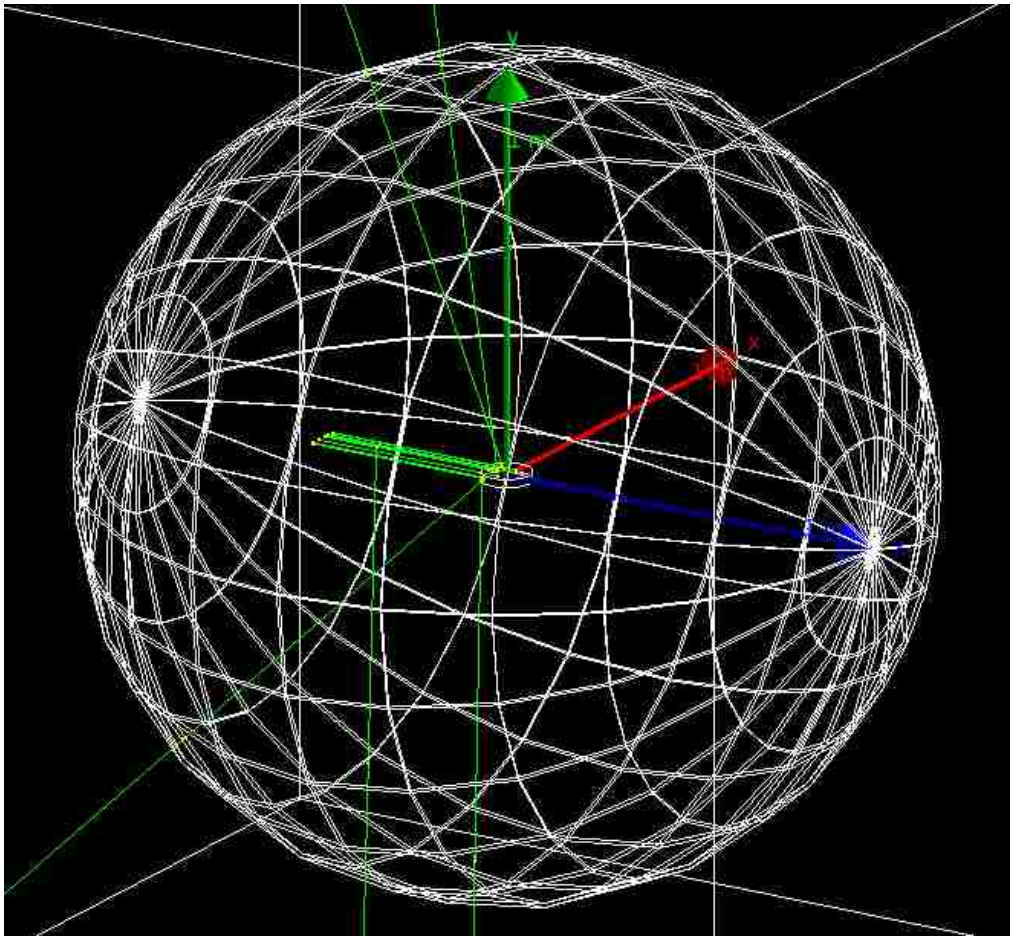

Figure 2.2. The scatter setup used for simulations. The green lines entering the disc from the left side represent individual photons in the primary beam. The mesh sphere was used to score the direction of each photon it passed through or scattered within the disc.

Within the scatter setup, a rectangular incident beam of polarized, monoenergetic photons was created inside the world volume at x = 0 cm, y = 0 cm, and z = -50 cm with a width of 10 cm and height of 2 mm. The primary beam struck the side of the disc of water, which was aligned parallel to the incident beam as shown in Figure 2.2. The disc of water either transmitted, absorbed,

or scattered the primary photons. Centered on the disc was a mesh sphere with a radius of one meter. This sphere was used to score the positions of the photons that crossed the mesh sphere, allowing the direction of travel of scattered photons to be determined.

Custom scoring was used in these simulation runs. Each simulated photon was transported from the source to the target, i.e., the disc of water. If the photon was not absorbed in the target, transport continued until the photon crossed the mesh sphere. Upon crossing the mesh sphere, the xyz coordinate on the sphere and the current kinetic energy of the photon were recorded in the simulation's common separated values (CSV) output file for later analysis; this file is referred to as the scatter file. After the photon crossed the mesh sphere, transport was terminated.

2.2. GEANT4 Attenuation Setup

The attenuation setup model allowed for the calculation of albedos as well as primary and secondary TVLs for typical shielding materials. Figure 2.3. shows the attenuation setup in GEANT4 in which the world volume is a 3 m x 3 m x 3 m cube. Inside the world volume, a beam of polarized photons is simulated to interact with a 3 m x 3 m x 1 m block of material, which is representative of a shielding barrier.

The middle of the surface of the block of material resides at x = 0 cm, y = 0 cm, and z = 0 cm within the attenuation setup. A rectangular incident beam of polarized photons was created inside the world volume at x = 0 cm, y = 0 cm, and z = -50 cm with a width of 10 cm and height of 2 mm. This beam was incident on the normal to the face of the block of material, modeling zero degrees incidence on the barrier; only zero degrees incidence on a barrier was simulated since the primary beam is always perpendicular to the primary barrier for synchrotron beamline hutches. The photons were tracked as they transmitted through, absorbed in, or reflected back from the block of material. Centered on the surface of the block of material was a mesh hemisphere with 1

m radius, which acted as a detector plane to determine the directions of the reflected photons for assessing albedo.

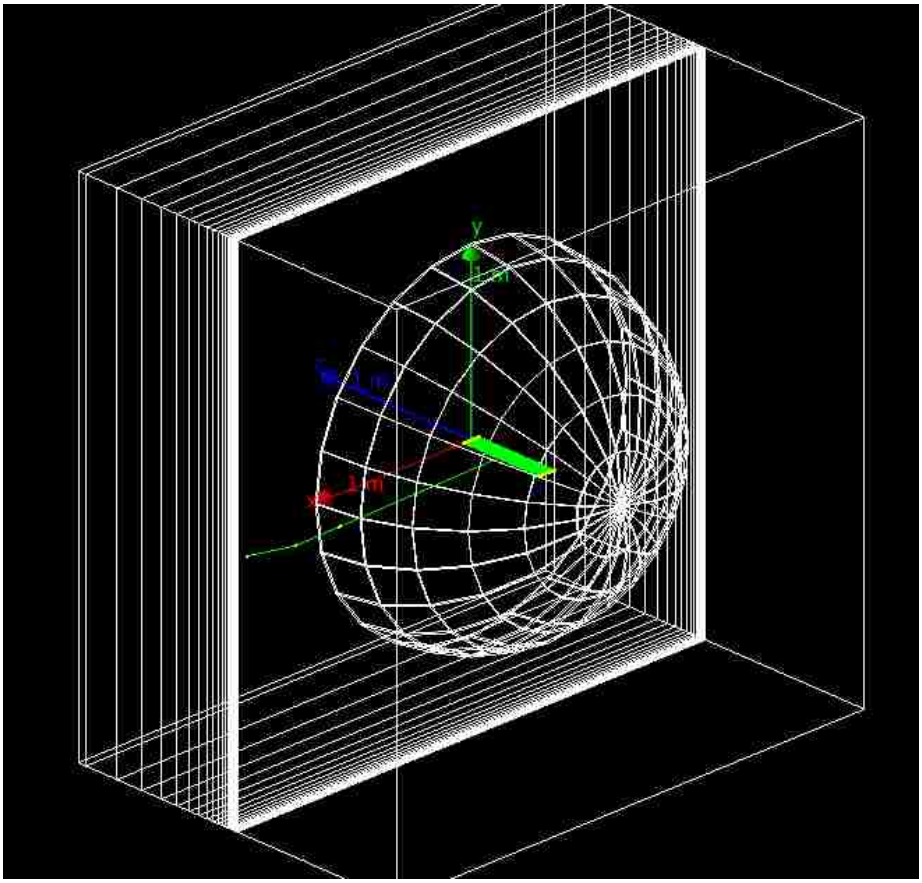

Figure 2.3. The attenuation setup used for simulations. The thick green line entering the block of material from the right side was the primary beam. The mesh hemisphere was used to score photons that backscattered from the block of material. The planes in the slab of material were used to tally transmitted photons reaching each plane.

The values of the albedos and primary TVLs were determined by simulating a primary beam of polarized, monoenergetic photons striking the block of material. The same method was used to determine the secondary TVLs, except the x-ray beam was comprised of polyenergetic photons; the energy spectrum used for the polyenergetic photons was modeled from the energy spectrum of the scattered photons produced by the scatter setup simulations. To get this energy spectrum from each scatter setup simulation, the scattered photons' energies were histogrammed and used as input to the secondary TVLs simulations.

The materials used for the determination of albedos and primary TVLs were the National Institute of Standards and Technology (NIST) definitions for concrete, lead, and steel, but only lead and steel were used when determining secondary TVLs since concrete is not a typical secondary barrier shielding material for synchrotron beamline hutches due to possible relocation of the beamline hutch. These materials were chosen since they are typical materials used for shielding as primary and secondary barriers. The compositions for NIST defined concrete and steel are provided in Table 2.2. (Geant4 Collaboration 2015).

Custom scoring was used in these simulation runs. Each photon was tracked from the source to the block of material through all interactions until either the photon's energy was absorbed, the photon was transmitted from the back of the block of material, or the photon was backscattered out through the hemispherical detector surface. Scoring of the backscattered photons occurred at the hemispherical detector plane, while attenuation was scored at logarithmically-spaced planes (depths) in the block of material. The location of each plane was calculated with the following equation:

$$x_i = \omega_0 \, 10^{i/B} - \omega_0 \qquad \text{[Eq. 5]}$$

where i ranged from 1 to 50, ω_0 was an offset of 10^{-5} m, and B had a value of 10.

The attenuation setup produced two outputs. The first was a CSV file containing the scoring data from the hemispherical detector surface. This file contained the xyz coordinate and kinetic energy of each photon that crossed the detector and is known as the albedo file, as it stored the data needed to calculate albedos. The second was a CSV file that contained the data from the target material planes. Each row of this file contained the number of photons and the total energy fluence that crossed the target material planes on a plane-by-plane basis; the number of rows in the file corresponds one-to-one with the number of target material planes. This file is known as the TVL

file as it stored the data needed to calculate the primary or secondary TVLs. The albedo file was ignored when calculating secondary TVLs.

Table 2.2. Compositions of NIST defined concrete and steel used in GEANT4 simulations.

Material	**Composition of Mixture in Percentage of Weight**
Concrete	1.0 H, 0.1 C, 52.9 O, 1.6 Na, 0.2 Mg, 3.4 Al, 33.7 Si, 1.3 K, 4.4 Ca, 1.4 Fe
Steel	8.0 Cr, 74.0 Fe, 18.0 Ni

2.3. Validation of GEANT4 Physics Model

To ensure the GEANT4 simulations were coded correctly, validation of the physics model was validated by comparing to a publication (Knights 2018) that presented experimental data of the number of polarized photons that were scattered parallel and perpendicular to the plane of the experiment's scattering object. Knight used a single cesium-137 source for the experimental setup, which emits a 661.7 keV gamma. The source was spaced 13 cm away from a first scattering object referred to as Scatterer-1. The 661.7 keV gammas interacted with Scatterer-1 to produce a partially polarized beam of scattered photons, estimated by Knights to be $56 \pm 5\%$ polarized; the experiment used the 320 keV photons that came from scattering at 80°. Scatterer-2 was 7.8 cm away from Scatterer-1. When the 320 keV photons interacted with Scatterer-2, photons that emerged 90° from Scatterer-2 had a kinetic energy of 197 keV. These 197 keV photons were detected by Detector-1, which was 7 cm from Scatterer-2 in the plane perpendicular to Scatterer-1, and Detector-2, which was 7 cm from Scatterer-2 in the plane of Scatterer-1. Both scatterers and detectors were NaI(Tl) scintillators. Scatterer-1 had a diameter of 1.91 cm and a length of 2.54 cm, Scatterer-2 had a diameter of 2.54 cm and a length of 2.54 cm, and Detectors 1 and 2 had a diameter of 5.08 cm and length of 5.08 cm. Figure 2.5. shows the layout of this experimental setup. (Knights *et al.* 2018)

The disc of water in the GEANT4 scatter setup was modified to match the orientation and size of Scatterer-2. Then, a beam of one billion polarized, monoenergetic 320 keV photons was simulated striking the target. The plane of polarization for the photons was not modified from the orientation shown in Figure 2.1., thus corresponding to the *y'* axis in Figure 2.5.

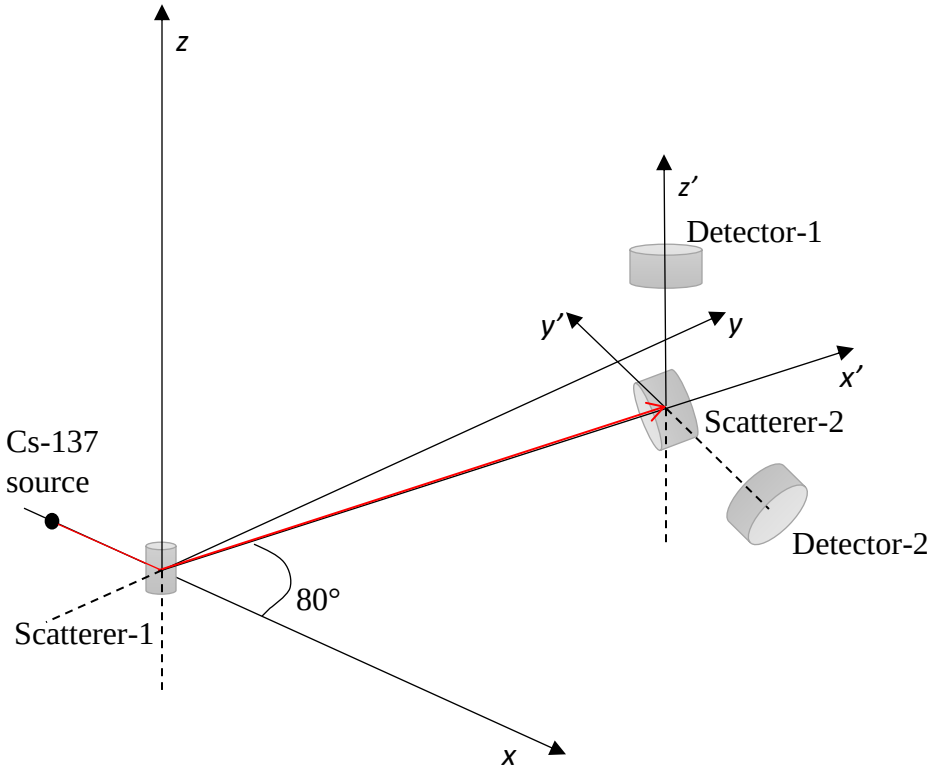

Figure 2.5. Experimental setup used by Knights. Adapted from (Knights 2018). The polarization vector lies on the *y'* axis.

The simulated scatter data was analyzed to determine the ratio of the number of scattered photons crossing Detector-1's surface to the number of photons crossing Detector-2's surface. The ratio was determined by a Python script that counted the number of photons that crossed through two circles. Each circle had a radius of 36.3 cm and was centered one meter away from the target on either the *z'*-axis or *–y'*-axis that is shown in Figure 2.5.; the radius of these circles was scaled to correspond to the sizes of Detector-1 and Detector-2 in the experimental setup, which were only

7 cm away from the target. Only the scattered photons with energies between 135 keV and 295 keV, the same energy window used by Knights, were counted in the ratio.

The verification simulation resulted in a ratio of 3.1 for photons scattered in the parallel verses perpendicular directions. Knights did not report a ratio, but gave graphical data from which the ratio could be obtained. WebPlotDigitizer (Rohatgi 2012) was used to extract the number of photons in Knights experiment that scattered towards each detector. Two screenshots showing the analysis of Knights graphical data are shown in Figure 2.6. After processing, Knights data yielded a ratio of approximately 2.5. These two ratios are generally in agreement, with the discrepancy likely due to Knights' experimental method not resulting in a 100% polarized beam.

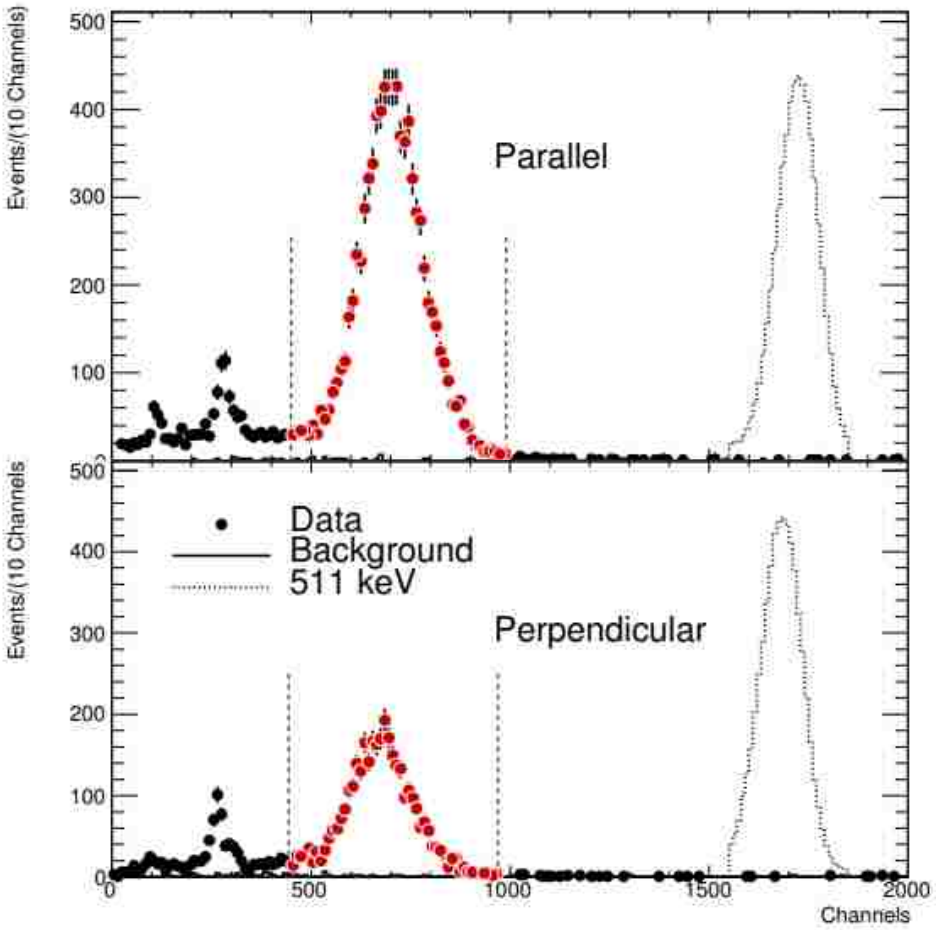

Figure 2.6. Screenshots of WebPlotDigitizer extracting data for the parallel (top) and perpendicular (bottom) scattered photons from Knights experiment.

The Klein-Nishina formula, which describes the probability of photon scattering in terms of energy and direction, indicates that Knights' experimental beam likely did not consist of a single polarization angle, but rather a distribution of polarization angles. To simulate a distribution of polarization angles in GEANT4, eight hundred million of the 320 keV simulated photons with the original polarization angle were combined with one hundred million simulated 320 keV photons with a polarization of +45° to the original polarization angle and one hundred million simulated 320 keV photons with a polarization of -45° to the original polarization angle. Analysis of this dataset produced a ratio of 2.4, which was comparable to the ratio obtained from Knights data.

Chapter 3. Specific Aim 1: Determination of Scatter Fractions

3.1. Methods and Materials: Python Analysis

Using Python version 3.6, a script was written to determine the scatter fractions from the disc of water for synchrotron x-ray energies between 10 keV and 100 keV in 5 keV increments. Recall from Section 2.1, the scatter setup in GEANT4 was used to determine scatter fractions for different monoenergetic beamlines. The Python script was executed from Windows' Command Prompt on Windows 10.

As stated in Section 2.1, the scatter files recorded the xyz coordinates where the scattered photons crossed the mesh sphere and their energies when crossing the sphere. Within the Python script, the scatter file for each simulated energy was opened; the data were read into appropriate variables and processed. As the first processing step, the azimuthal and polar angles were calculated for each scattered photon by converting Cartesian coordinates to spherical coordinates. The formulas used to determine the scattered photon's azimuthal (ϕ) and polar (θ) angles were:

$$\phi = \operatorname{arctan2}\left(\frac{y}{x}\right) = \begin{cases} \tan^{-1}\left(\frac{y}{x}\right) & \text{if } x > 0 \\ \tan^{-1}\left(\frac{y}{x}\right) + \pi & \text{if } x < 0 \text{ and } y \geq 0 \\ \tan^{-1}\left(\frac{y}{x}\right) - \pi & \text{if } x < 0 \text{ and } y < 0 \\ +\frac{\pi}{2} & \text{if } x = 0 \text{ and } y > 0 \\ -\frac{\pi}{2} & \text{if } x = 0 \text{ and } y < 0 \\ \text{undefined} & \text{if } x = 0 \text{ and } y = 0 \end{cases} \quad \text{[Eq. 6]}$$

$$\theta = \frac{\cos^{-1}(z)}{\sqrt{x^2 + y^2 + z^2}} \quad \text{[Eq. 7]}$$

where $x, y,$ and z were the Cartesian coordinates where the scattered photon crossed the sphere. After the azimuthal and polar angles were calculated, they were sorted into a two dimensional histogram, with bin widths of one degree for both angles. The bins ranged from -180.0 degrees to 180.0 degrees for the azimuthal angles and 0.0 degrees to 180.0 degrees for the polar angles.

Next, the energies of the scattered photons located in each bin of the 2D histogram were summed and stored in a 2D matrix, which had the same dimensions as the 2D histogram creating a one-to-one correspondence between the two variables. This process was repeated for all data files for the one billion events at each primary energy, creating a summed 2D energy matrix for all one billion events. This process produced the total energy of all scattered photons at each specific combination of azimuthal and polar scattering angles. The scatter fractions were then determined per angular bin by dividing the 2D summed energy matrix by the total energy of the incident beam. This is represented by the equation:

$$\text{Scatter Fraction per Bin} = \frac{\text{Bin of 2D Energy Matrix}}{\text{Initial Kinetic Energy of the Beam}} \qquad \text{[Eq. 8]}$$

Lastly, the scatter fractions were written to a text file and stored for later analysis.

3.2. Scatter Fraction Results

To compare scatter fractions between various scattering angles and primary beam energies, the scatter fractions for each primary beam energy were displayed as color contoured, polar plots. Figure 3.1. shows a representative example of the scatter fractions of a 75 keV primary beam scattering from the disc of water simulated in the GEANT4 scatter setup (Section 2.1).

At each energy, a pair of two polar plots shows all possible scatter directions. One polar plot shows the scatter fractions on the front half of the mesh sphere, corresponding to scatter in the forward direction. Similarly, the other polar plot shows the scatter fractions for scatter in the backwards direction. Radial lines denote the azimuthal angles of the scattering geometry, while concentric circles represent the polar angles. A scattering angle of 0° (the center of the forward scatter plot) corresponds to the direction of the incident beam and the outer edges of the two polar plots match one another with a scattering angle of 90°. Lastly, the rainbow color scale presents the scatter fraction magnitude.

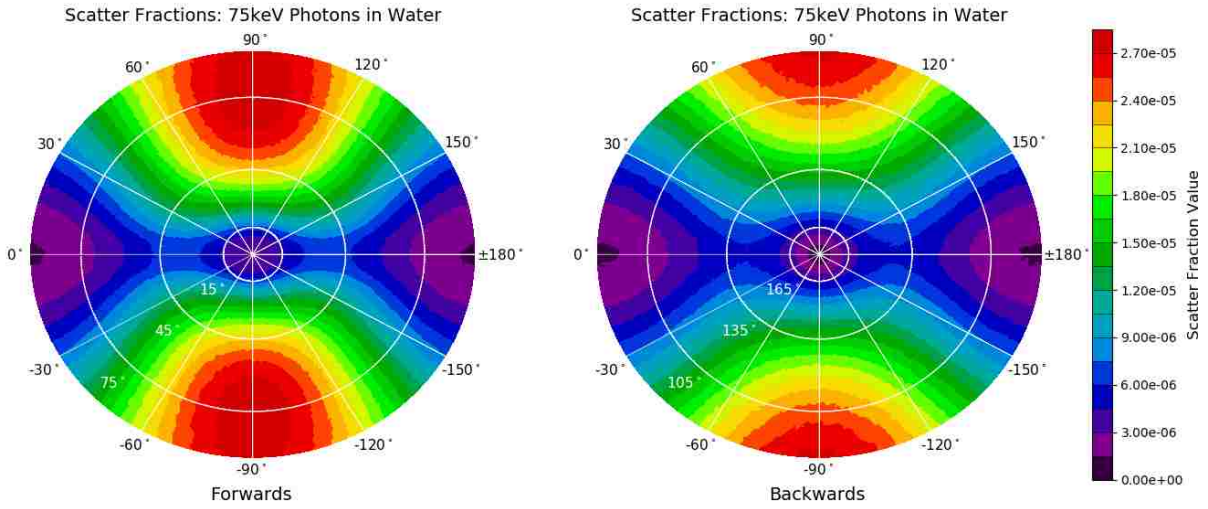

Figure 3.1. Example display of scatter fractions for a 100x2-mm^2 beam of 75 keV polarized photons scattering from a 2-cm high x 6-cm radius cylinder of water. All possible scatter directions are shown as polar plots representing the front half (left), i.e., with 0° (center of the plot) defined as the direction of the incident beam, or back half (right) of the sphere. White radial lines mark azimuthal angles of the scattering geometry, while concentric circles correspond to polar angles. The plots match at their outer edges, corresponding to a 90° scatter angle. The color scale represents scatter intensity.

Scatter fractions are plotted for a representative set of primary beam energies, using the same color scale for all plots, in Figure 3.2. One sees that the scatter in a particular direction typically increases with the primary beam energy; this is due to the increasing ratio of Compton scattering probability to photoelectric absorption as the primary beam energy increases. The polarization of the primary x-rays, along the 0° azimuthal direction, results in a large asymmetry for scattering in the horizontal (in-ring) plane verses the vertical direction. For comparison, an unpolarized x-ray beam would result in an azimuthally symmetric distribution (Attix 1986).

Figure 3.3. shows the same representative set of primary beam energies with color scaling to the individual maximum scatter fraction value; this was done to emphasize the asymmetric patterns in the plots. A consistent asymmetrical pattern was seen in the pattern of scatter fractions across the primary beam energies. Figure 3.3. also shows the scatter becoming more forward peaked at higher energies. This is the expected behavior for Compton scattering probability verses

scattering angle with increasing energy (Attix 1986). The scatter fraction plots for each primary beam energy are provided in Appendix B.

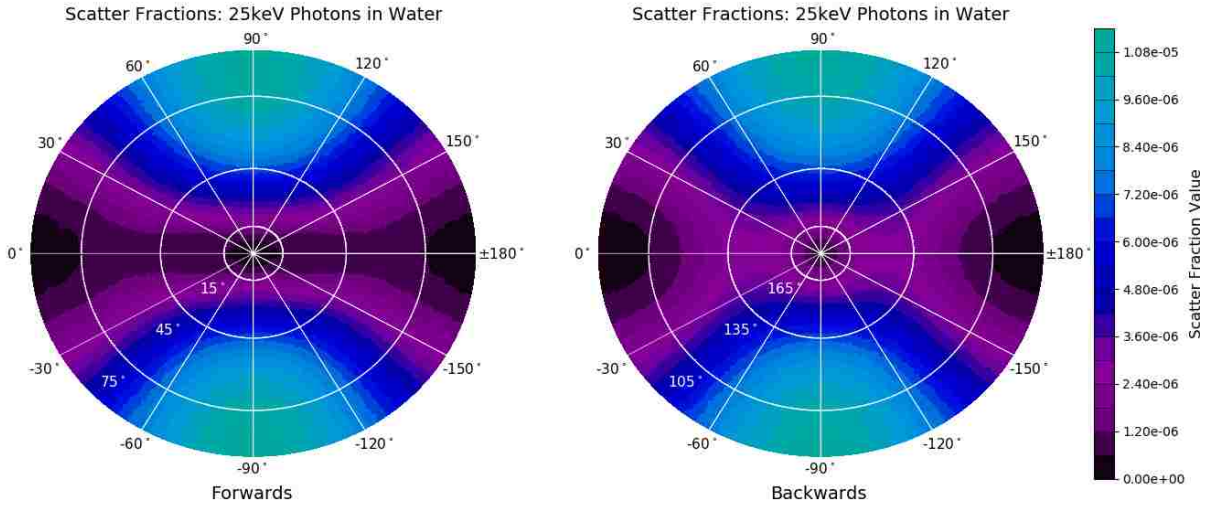

(a)

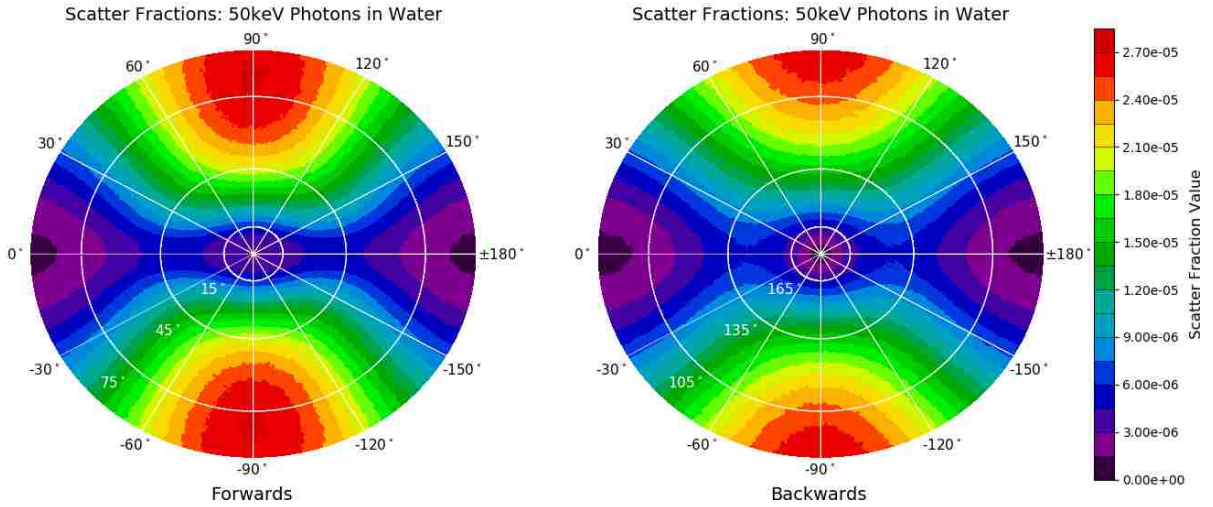

(b)

Figure 3.2. Scatter fractions for a 100x2-mm^2 beam of 25 keV (a) and 50 keV (b) polarized photons scattering from a 2-cm x 6-cm radius cylinder of water. The polarization vector lies in the 0° azimuthal direction. See Figure 3.1. for summary of plot annotations.

(fig. cont'd.)

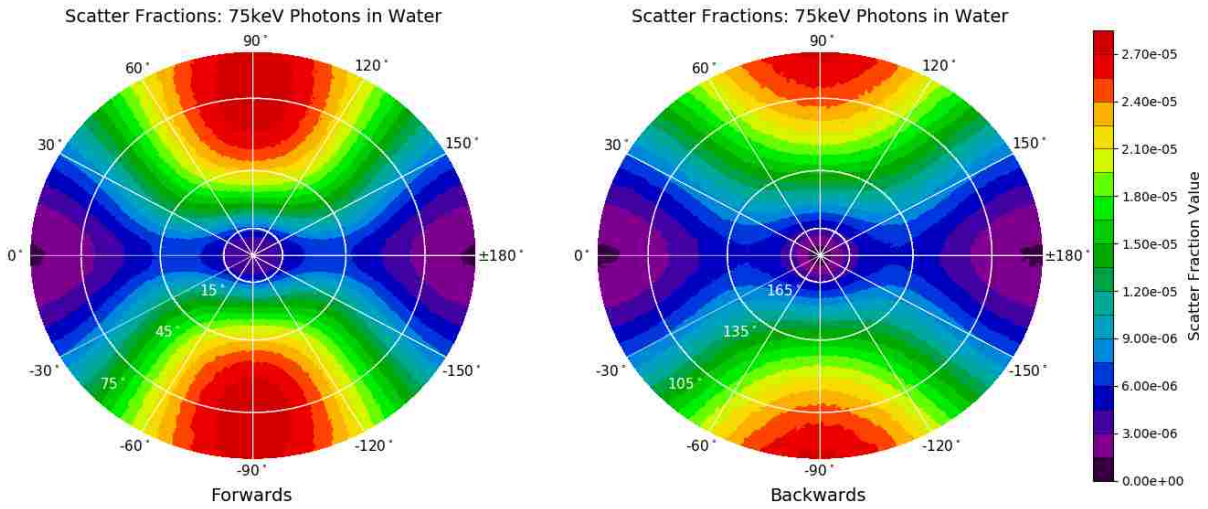

(c)

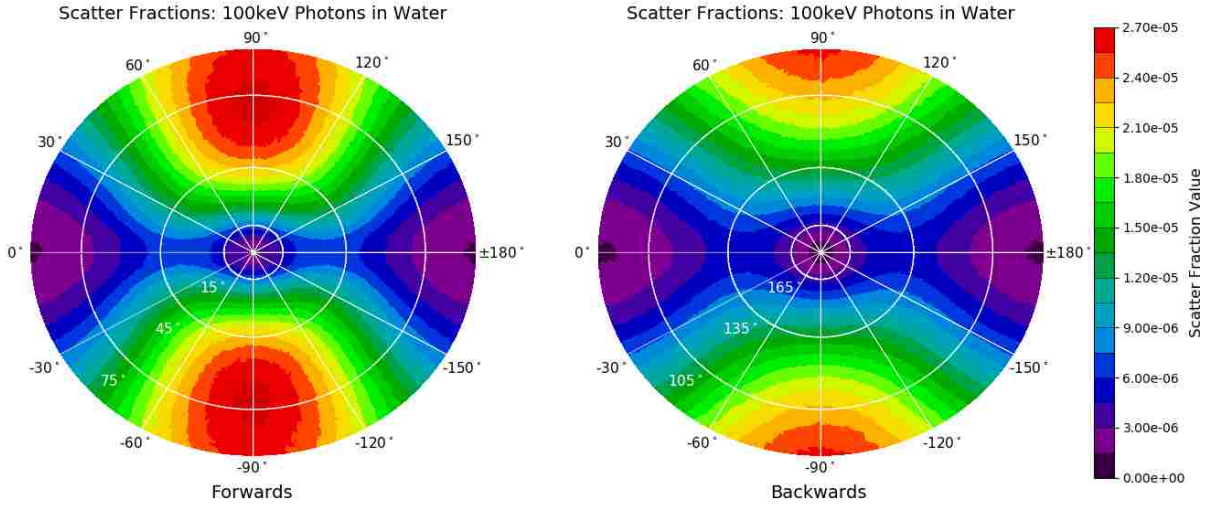

(d)

Figure 3.2. Scatter fractions for a 100x2-mm^2 beam of 75 keV (c) and 100 keV (d) polarized photons scattering from a 2-cm x 6-cm radius cylinder of water. The polarization vector lies in the 0° azimuthal direction. See Figure 3.1. for summary of plot annotations. The scatter fraction magnitude in a specific direction is typically lower at lower energies than at higer energies, as expected. The asymmetry of scatter fraction verses direction due to the primary beam polarization is clearly evident.

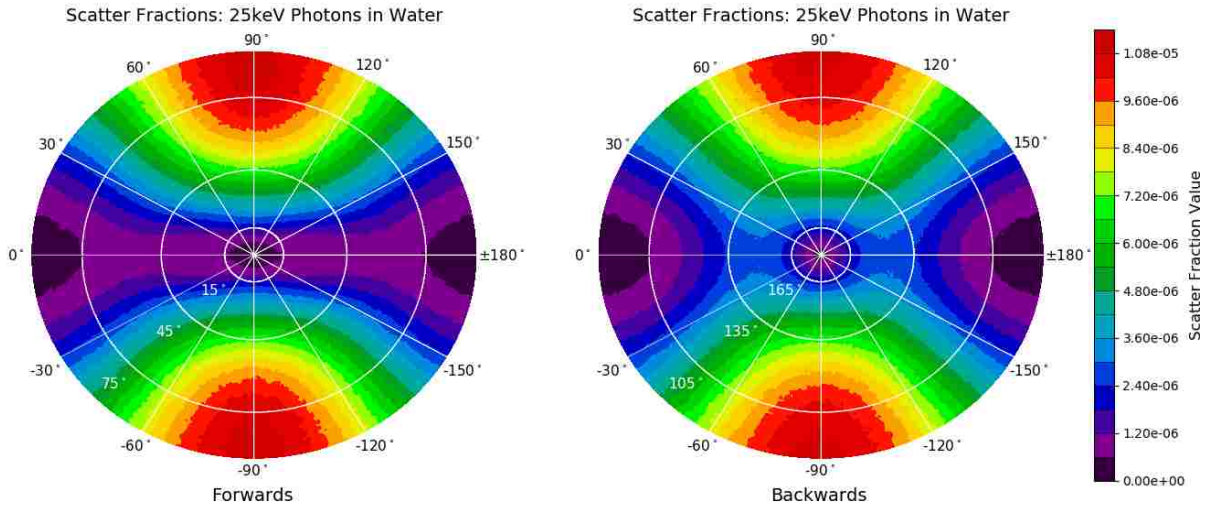

(a)

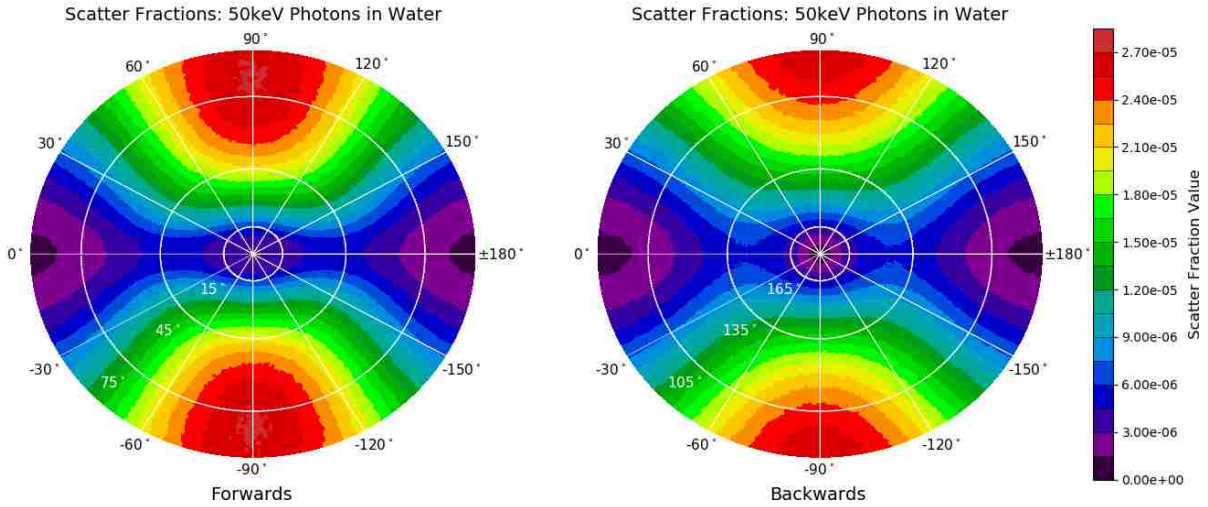

(b)

Figure 3.3. Scatter fractions for a 100x2-mm^2 beam of 25 keV (a) and 50 keV (b) polarized photons scattering from a 2-cm x 6-cm radius cylinder of water. The polarization vector lies in the 0° azimuthal direction. See Figure 3.1. for summary of plot annotations.

(fig. cont'd.)

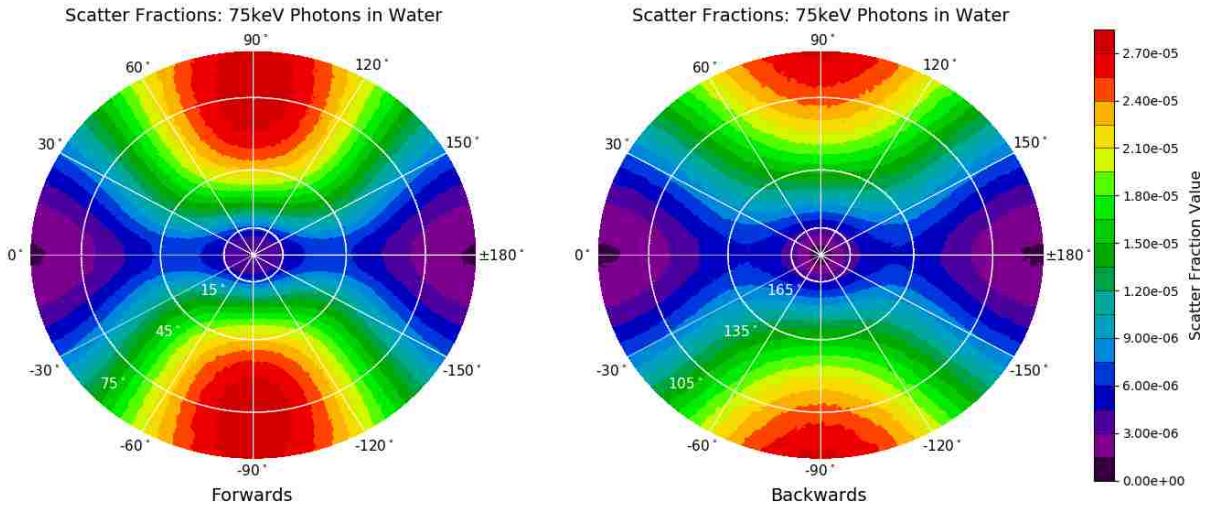

(c)

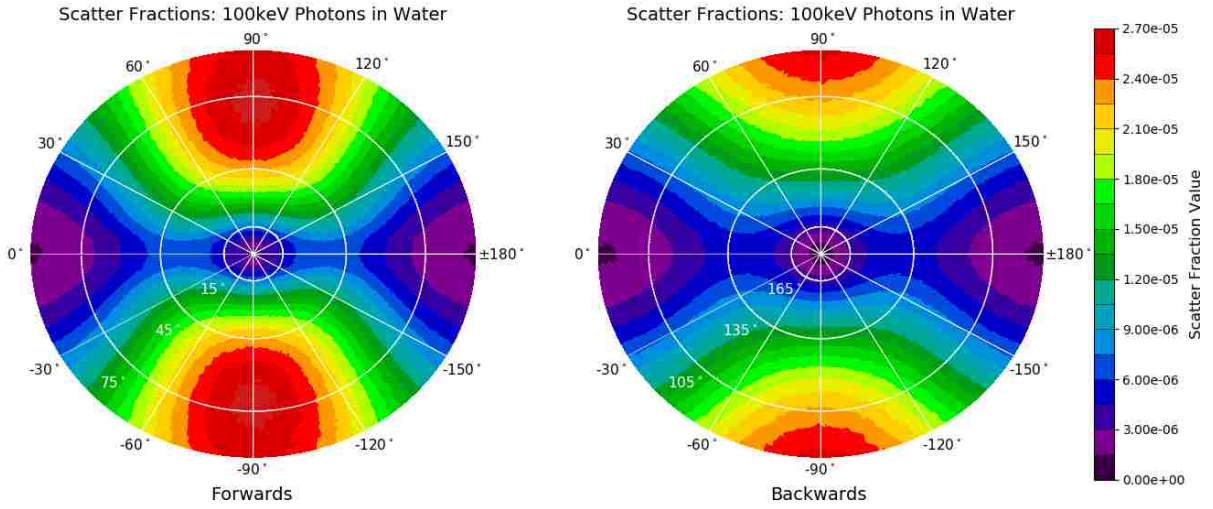

(d)

Figure 3.3. Scatter fractions for a 100x2-mm^2 beam of 75 keV (c) and 100 keV (d) polarized photons scattering from a 2-cm x 6-cm radius cylinder of water. The polarization vector lies in the 0° azimuthal direction. See Figure 3.1. for summary of plot annotations. The asymmetric pattern in scatter fraction verses direction (horizontial verses vertical) due to polarization is consistent across primary beam energies. The scatter fractions also become more forward directed at higher energies, as expected.

Although visual presentation of the scatter fraction data allows for patterns and differences to be easily compared, it is not always a practical format to utilize the data for shielding design.

Scatter fractions for 17 key locations on the walls of a beamline hutch are reported in table format. The 17 locations are listed in Table 3.1.; the scatter fractions for these locations are given in Table 3.2. The key locations are defined by the azimuthal and polar angles relative to the primary beam's direction. Due to asymmetry in the data, listed scatter fraction values in Table 3.2. can be used for the hutch's mirrored key locations. Note in Table 3.1. and Table 3.2., midpoints for the downstream and upstream wall are not reported. Reporting scatter fractions for these midpoints is nonsensical since the primary beam is incident on the downstream midpoint and the upstream midpoint corresponds to the least probable scatter direction (180° backscattered events), resulting in little to no scatter fraction; instead key locations adjacent to these midpoints have been reported.

Table 3.1. Description of key locations relative to the primary beam's incident direction.

Polar Angle, θ (°)	**Azimuthal Angle, ϕ (°)**	**Key Location Description**
5	0	Slightly left of beam, downstream wall
45	90	Middle roof, downstream wall
45	45	Junction of roof, lateral, and downstream wall, top corner
45	0	Junction of roof, lateral, and downstream wall, midpoint
45	-45	Junction of roof, lateral, and downstream wall, bottom corner
45	-90	Middle floor, downstream wall
90	90	Roof midpoint
90	45	Junction of roof and lateral wall midpoint
90	0	Lateral wall midpoint
90	-45	Junction of floor and lateral wall midpoint
90	-90	Floor midpoint
135	90	Middle roof, upstream wall
135	45	Junction of roof, lateral, and upstream wall, top corner
135	0	Junction of roof, lateral, and upstream wall, midpoint
135	-45	Junction of roof, lateral, and upstream wall, bottom corner
135	-90	Middle floor, upstream wall
175	0	Slightly left of beam, upstream wall

Table 3.2. Scatter fractions at one meter from the target, a disc of water with radius of 6 cm and height of 2 cm, for a beam size of 100x2-mm^2. Multiply each entry by the multiplication factor found in the "Multiply" row.

	Scatter Fractions represented by Polar (θ) and Azimuthal (ϕ) Angles																
θ (°)	**5**	**45**	**45**	**45**	**45**	**45**	**90**	**90**	**90**	**90**	**90**	**135**	**135**	**135**	**135**	**135**	**175**
ϕ (°)	**0**	**90**	**45**	**0**	**-45**	**-90**	**90**	**45**	**0**	**-45**	**-90**	**90**	**45**	**0**	**-45**	**-90**	**0**
Multiply	10e-6	10e-5	10e-5	10e-6	10e-5	10e-5	10e-5	10e-5	10e-6	10e-5	10e-5	10e-5	10e-5	10e-6	10e-5	10e-5	10e-6
Energy (keV)																	
10	0	0.02	0.02	0.14	0.02	0.02	0.02	0.02	0.02	0.02	0.02	0.05	0.03	0.13	0.03	0.04	0.06
15	0	0.07	0.03	0.22	0.32	0.064	0.11	0.06	0.04	0.06	0.11	0.15	0.11	0.65	0.10	0.14	0.21
20	0.03	0.30	0.16	0.37	0.16	0.29	0.50	0.23	0.15	0.22	0.49	0.37	0.25	1.40	0.24	0.37	0.39
25	0.31	0.71	0.42	0.89	0.43	0.71	1.10	0.52	0.31	0.5	1.10	0.70	0.46	2.51	0.44	0.68	0.62
30	1.03	1.14	0.73	1.91	0.72	1.15	1.67	0.81	0.57	0.78	1.69	1.02	0.68	3.45	0.68	1.00	0.81
35	1.91	1.51	1.00	2.84	0.99	1.51	2.09	1.05	0.73	1.01	2.10	1.25	0.86	4.27	0.87	1.26	0.97
40	2.48	1.74	1.20	3.71	1.18	1.77	2.41	1.21	0.96	1.16	2.36	1.39	0.99	4.86	0.98	1.41	1.09
45	3.07	1.93	1.31	4.39	1.33	1.94	2.57	1.31	1.13	1.26	2.56	1.52	1.06	5.26	1.05	1.50	1.15
50	3.32	2.06	1.42	4.80	1.41	2.06	2.70	1.37	1.19	1.32	2.67	1.55	1.12	5.64	1.11	1.54	1.18
55	3.39	2.15	1.47	5.29	1.44	2.16	2.71	1.42	1.25	1.36	2.70	1.56	1.12	5.63	1.12	1.57	1.18
60	3.51	2.16	1.52	5.54	1.50	2.17	2.73	1.41	1.26	1.37	2.74	1.58	1.13	5.81	1.11	1.57	1.18
65	3.66	2.21	1.57	5.90	1.52	2.22	2.76	1.44	1.32	1.38	2.74	1.57	1.11	5.75	1.10	1.58	1.20
70	3.52	2.25	1.56	5.99	1.56	2.26	2.75	1.44	1.37	1.41	2.74	1.54	1.11	5.66	1.09	1.55	1.20
75	3.46	2.24	1.59	6.08	1.55	2.24	2.73	1.43	1.33	1.39	2.70	1.51	1.09	5.66	1.08	1.53	1.13
80	3.37	2.25	1.63	6.17	1.58	2.23	2.71	1.42	1.33	1.37	2.71	1.51	1.09	5.61	1.07	1.49	1.04
85	3.45	2.27	1.61	6.28	1.57	2.26	2.69	1.40	1.44	1.36	2.68	1.47	1.06	5.46	1.04	1.46	1.09
90	3.27	2.27	1.62	6.26	1.58	2.29	2.67	1.39	1.38	1.33	2.62	1.43	1.05	5.41	1.03	1.40	1.01
95	3.16	2.27	1.61	6.42	1.59	2.30	2.60	1.38	1.44	1.33	2.62	1.39	1.03	5.25	1.01	1.41	1.02
100	3.06	2.30	1.62	6.32	1.60	2.29	2.56	1.35	1.48	1.31	2.58	1.38	1.00	5.10	0.99	1.37	1.00

3.3. Scattered Photons Energy Spectrum

Figure 3.4. shows the scattered energy spectrum of 100 keV primary photons that was used for determination of 100 keV secondary TVLs. This spectrum is illustrative of the other energy spectra with their features being most prominent in the 100 keV scattered energy spectrum.

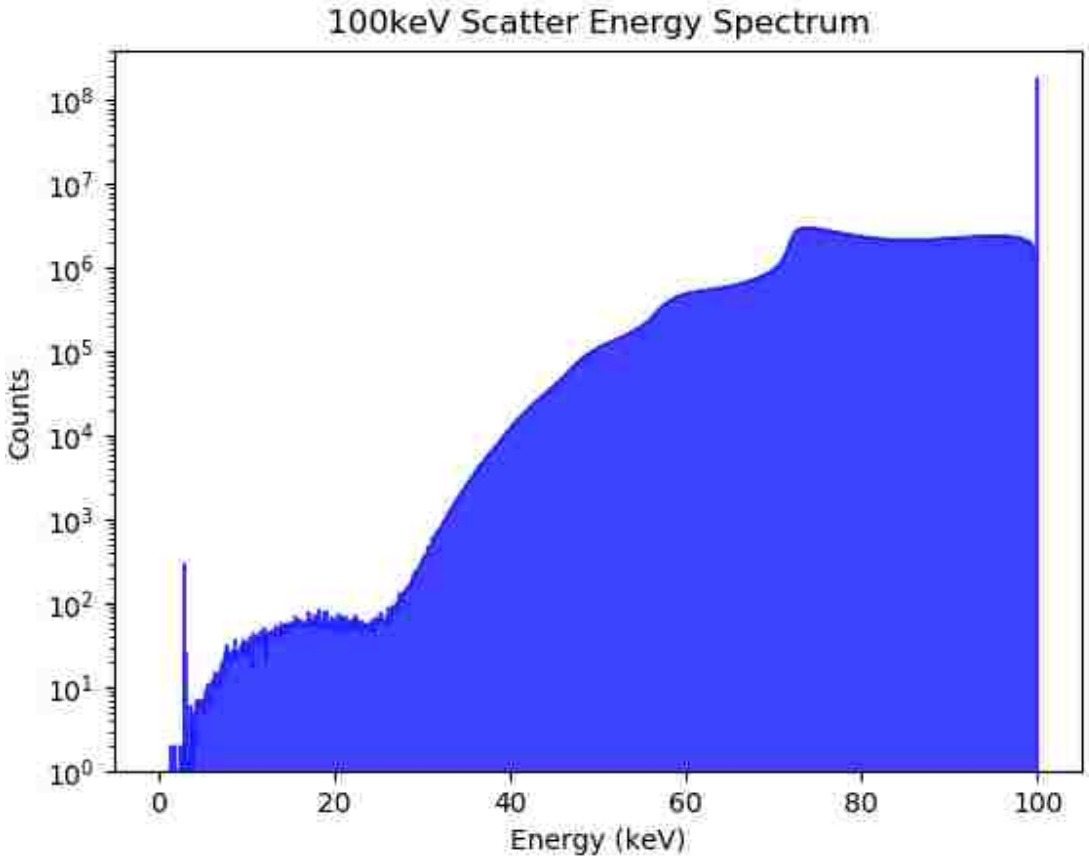

Figure 3.4. Histogram of the energy spectrum of secondary radiation used for the 100kV polyenergetic beam in the attenuation setup simulation (Section 2.2). The attenuation setup with this polyenergetic spectrum was used to determine 100 keV secondary TVLs.

In Figure 3.4., the narrow peak at the highest energy of the spectrum corresponds to the incident photons that did not scatter from the disc of water or underwent Rayleigh scattering. The adjacent flat portion of the spectrum, ranging from approximately 84 keV to just shy of 100 keV, represents the incident photons that experienced one forward Compton scattering event, while the hump in the spectrum (from ~ 72 keV to ~84 keV) corresponds to incident photons that experienced one backwards Compton scattering event. The slight drop covering energies from 63

keV to 72 keV are incident photons that have undergone two Compton scattering events, either two forward scattering events or a forwards and backwards scattering event. Interestingly, the medium sized bump from 56 keV to 63 keV agrees with an incident photon undergoing two backwards Compton scattering events. The next feature from roughly 46 keV to 56 keV relates to incident photons that have experienced three Compton scattering events, with the small bump in this region from 46 keV to 50.5 keV corresponding to those that have undergone three backwards scattering events. The extreme slope from approximately 30 keV to 46 keV match with the incident photons that have experienced more than three Compton scattering events. The remaining portion of the spectrum (30 keV and below) is quite noisy due to a low number of events falling within this region.

Chapter 4. Specific Aim 2: Determination of Albedos

4.1. Methods and Materials: Python Analysis

The methodology used to calculate the albedos for different shielding materials was the same method used to calculate scatter fractions discussed in Section 3.1. Using the previously developed Python script, albedos of typical shielding materials used for primary barriers in synchrotron beamline hutches were determined from the albedo files discussed in Section 2.2. Recall from Section 2.2 that the attenuation setup in GEANT4 was used to simulate interactions in NIST-defined concrete, lead, and steel using monoenergetic x-ray beams with energies between 10 keV and 100 keV. The attenuation setup used a hemisphere to score the backscattered photons instead of a sphere. Because of this, the 2D histogram used to bin the azimuthal and polar angles had a range of 90.0 degrees to 180.0 degrees for the polar angles. Also recall from Section 2.2 that only zero degrees incidence on a primary barrier was modeled since the beam is always perpendicular to the primary barrier for synchrotron beamline hutches.

4.2. Albedo Results

The same display method used to visualize the scatter fractions was also used to visualize the albedos. Since albedos are usually specified relative to the primary barrier's surface normal, one must mention that a polar angle of 180 degrees on the albedo plots corresponds to 0 degrees relative to the surface normal and a polar angle of 90 degrees on the albedo plots corresponds to 90 degrees relative to the surface normal. Figure 4.1. plots representative albedos for a 75 keV primary beam incident on each material, using the same color scale and range. One can see that the albedo magnitude varies substantially between the different shielding materials with the albedo magnitude for concrete substantially trumping those for lead and steel; this is due to Compton scattering dominating lower atomic number (Z) materials, like concrete, for synchrotron beamline

energies, whereas for higher Z materials like lead and steel, photoelectric absorption dominates (Attix 1986). However, when these same albedos are plotted with individual color scales ranging from the lowest to highest albedo values (Figure 4.2.), one see a similar asymmetrical pattern in the albedos for each of the shielding materials. The albedos for every combination of simulated primary beam energy and material are provided in Appendix C.

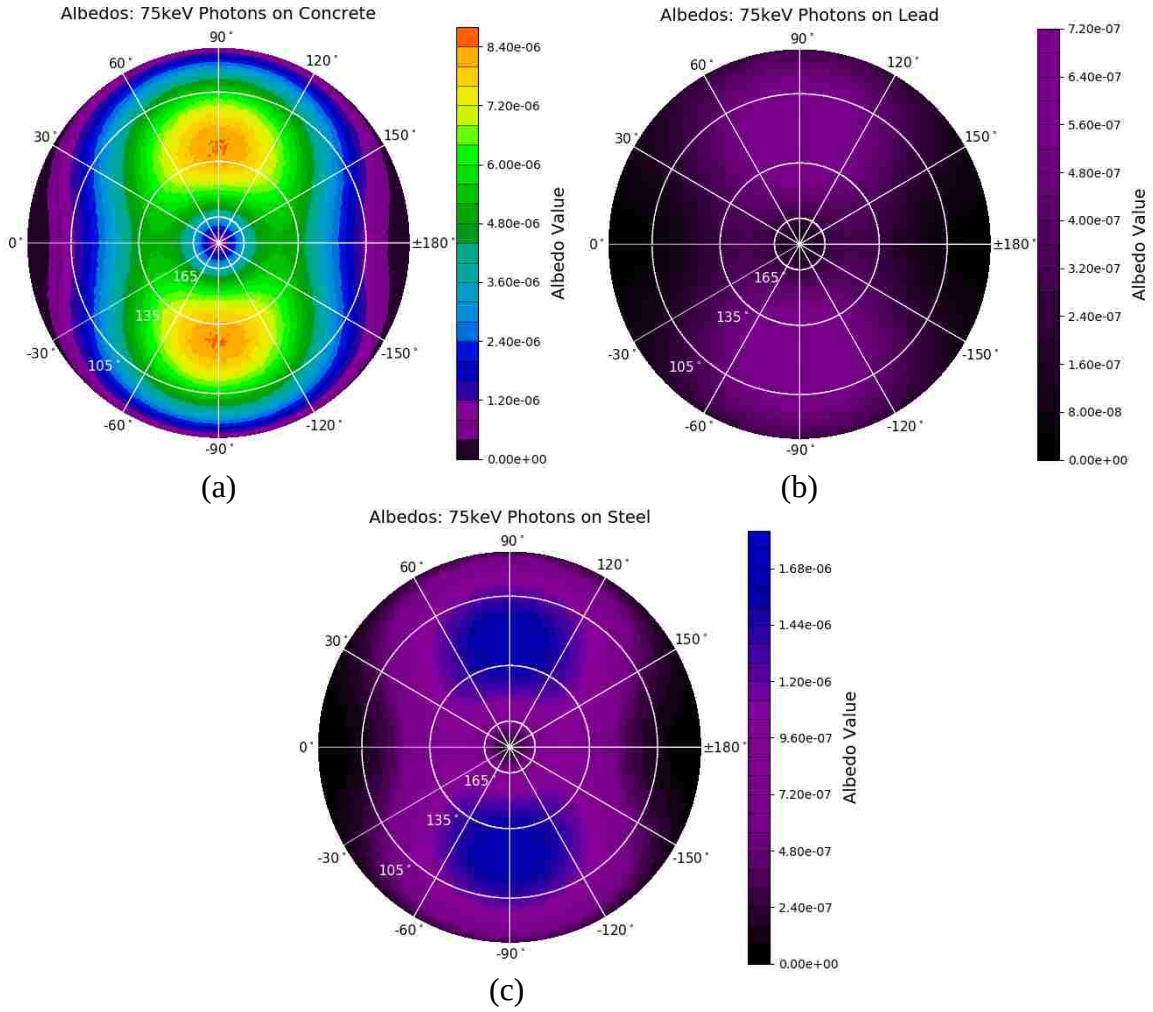

Figure 4.1. Albedos for a beam of 75 keV polarized x-rays incident on slabs of concrete (a), lead (b), and steel (c) on the same color scale range. Note the different albedo magnitudes for the three different shielding materials which is caused by Compton scattering dominating over photoelectric absorption for lower atomic number materials and vise versa for higher atomic number materials. See Figure 3.1. for summary of plot annotations.

The hourglass shaped asymmetric pattern as seen in Figure 4.2. is typical for every material and primary beam energy except for lead with primary beam energies greater than lead's K-edge

binding energy (88 keV). When the primary beam energy was greater than the material's K-edge, a generally symmetric pattern was seen in the albedos, as shown in Figure 4.3. for 90 keV, 95 keV, and 100 keV x-rays. A more rotationally-symmetric ring pattern was seen for these albedos above the K-edge of lead. It was surmised that the pattern's change above the K-edge was due to emission of fluorescence x-rays following photoelectric absorption of primary x-rays; the likelihood of photoelectric absorption, and hence fluorescence emission, increases substantially just above the K-edge of a material.

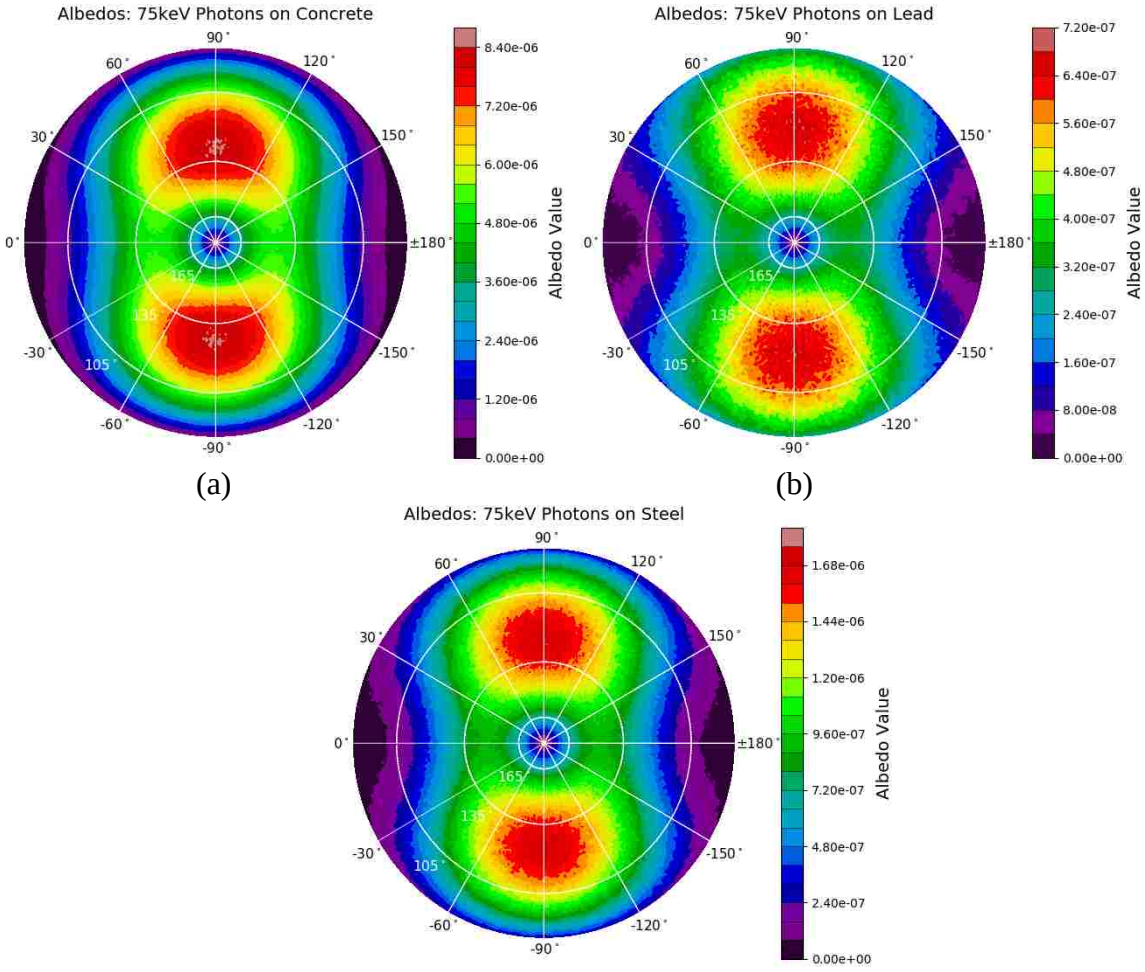

Figure 4.2. Albedos for a beam of 75 keV polarized x-rays incident on slabs of concrete (a), lead (b), and steel (c) on independent color scale ranges. Note the similar asymmetric pattern appearing across the materials due to polarization of the incident beam. See Figure 3.1. for summary of plot annotations.

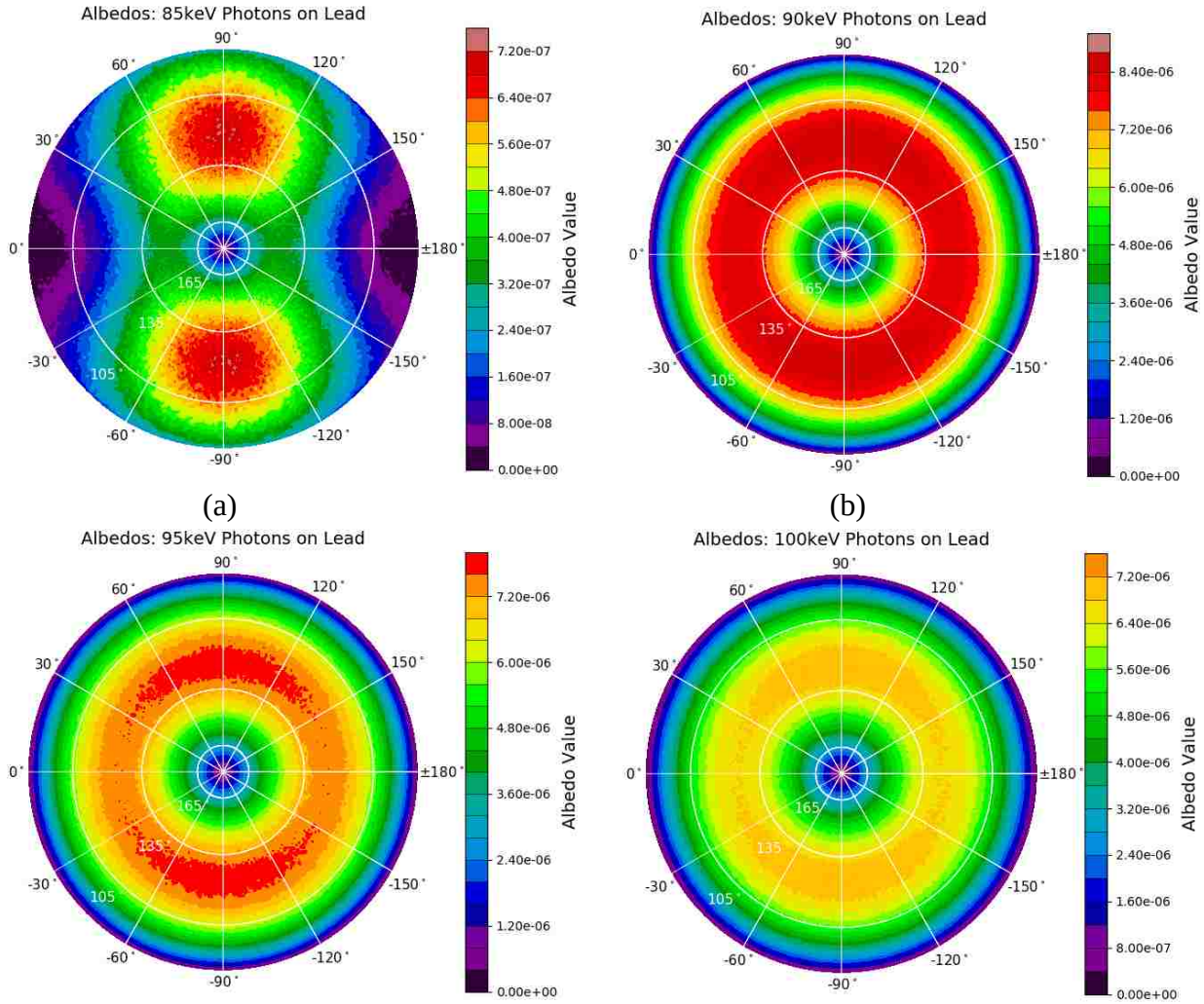

Figure 4.3. Albedos for beams of 85 keV (a), 90 keV (b), 95 keV (c), and 100 keV (d) polarized x-rays incident on slabs of lead on different color scale ranges. The 85 keV plot is on an individual color scale while the 90 keV, 95 keV, and 100 keV plots are on the same color scale. Note polarization causes substantial asymmetry at energies below the K-edge of the lead (a), but above the K-edge, fluorescence emission (b, c, and d) contributes substantially but homogenously to albedo. See Figure 3.1. for summary of plot annotations.

To test that this symmetric pattern was caused by crossing a material's K-edge, rather than a feature of lead itself, another high-Z shielding material, tungsten, was simulated for interactions at two primary beam energies that bracketed tungsten's K-edge of 69.5 keV, namely 65 keV and 70 keV. Figure 4.4. shows the albedos for these primary beams incident on tungsten. Comparable albedo patterns were seen for tungsten above and below the K-edge as was for lead.

Secondly, the attenuation setup simulations for primary beam energies of 90 keV, 95 keV, and 100 keV incident on lead were repeated, but with fluorescence photon production disabled in the GEANT4 physics list. The albedos for these runs are visually displayed in Figure 4.5. As anticipated, the same asymmetric pattern was seen for the primary beam energies greater than lead's K-shell binding energy when the fluorescence photons are no longer simulated.

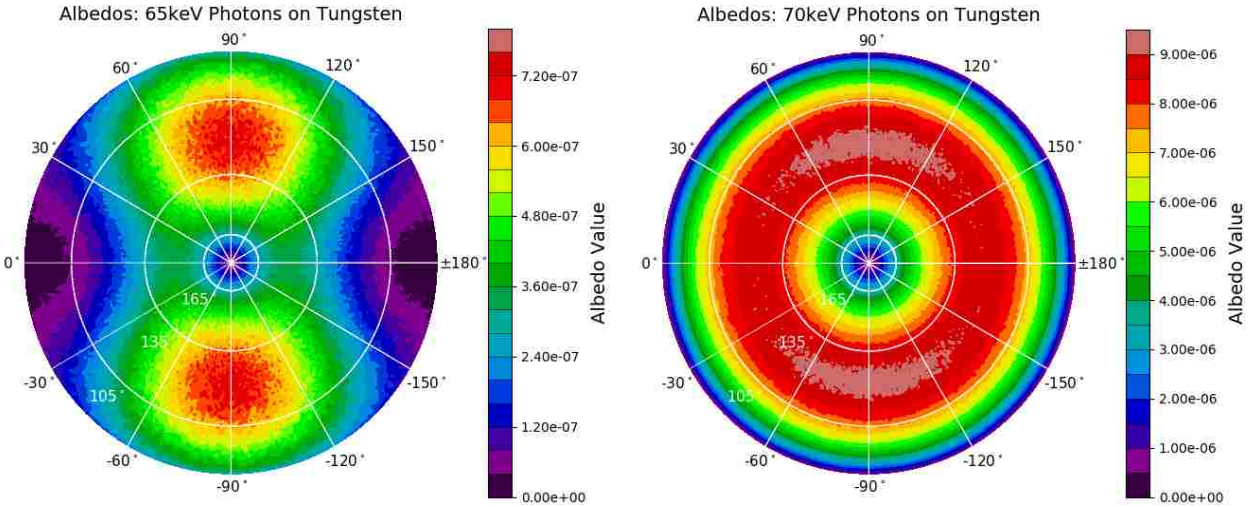

(a) (b)

Figure 4.4. Albedos for beams of 65 keV (a) and 70 keV (b) polarized x-rays incident on slabs of tungsten on different color scale ranges. Note polarization causes substantial asymmetry at energies below the K-edge of tungsten (a), but above the K-edge, fluorescence emission (b) contributes substantially but homogenously to albedo. See Figure 3.1. for summary of plot annotations.

Together, these two additional tests indicated that the symmetric pattern was due to x-ray energies exceeding the K-edge of any material, which subsequently increases photoelectric absorption and fluorescence emission. However, note that a symmetric pattern is not particularly evident at 10 keV in steel (Figure 4.6.), despite an iron K-edge at 7.1 keV; we expect this is due to strong self-attenuation of the low energy iron fluorescence x-rays in the steel block.

To utilize the data for shielding design, albedo values for all but one of the previously reported key locations on the walls of a beamline hutch (Section 3.2) are reported in table format; the key location that was not used resides on the primary barrier, which by definition cannot have

albedo incident on it. The key locations are listed in Table 4.1. and the albedo for these locations are given in Table 4.2. for a concrete primary barrier, Table 4.3. for a lead primary barrier, and Table 4.4. for a steel primary barrier. The key locations are defined by azimuthal and polar angles relative to the primary barrier's surface normal. Due to asymmetry in the data, listed albedo values in Table 4.2., Table 4.3., and Table 4.4. can be used for the hutch's mirrored key locations.

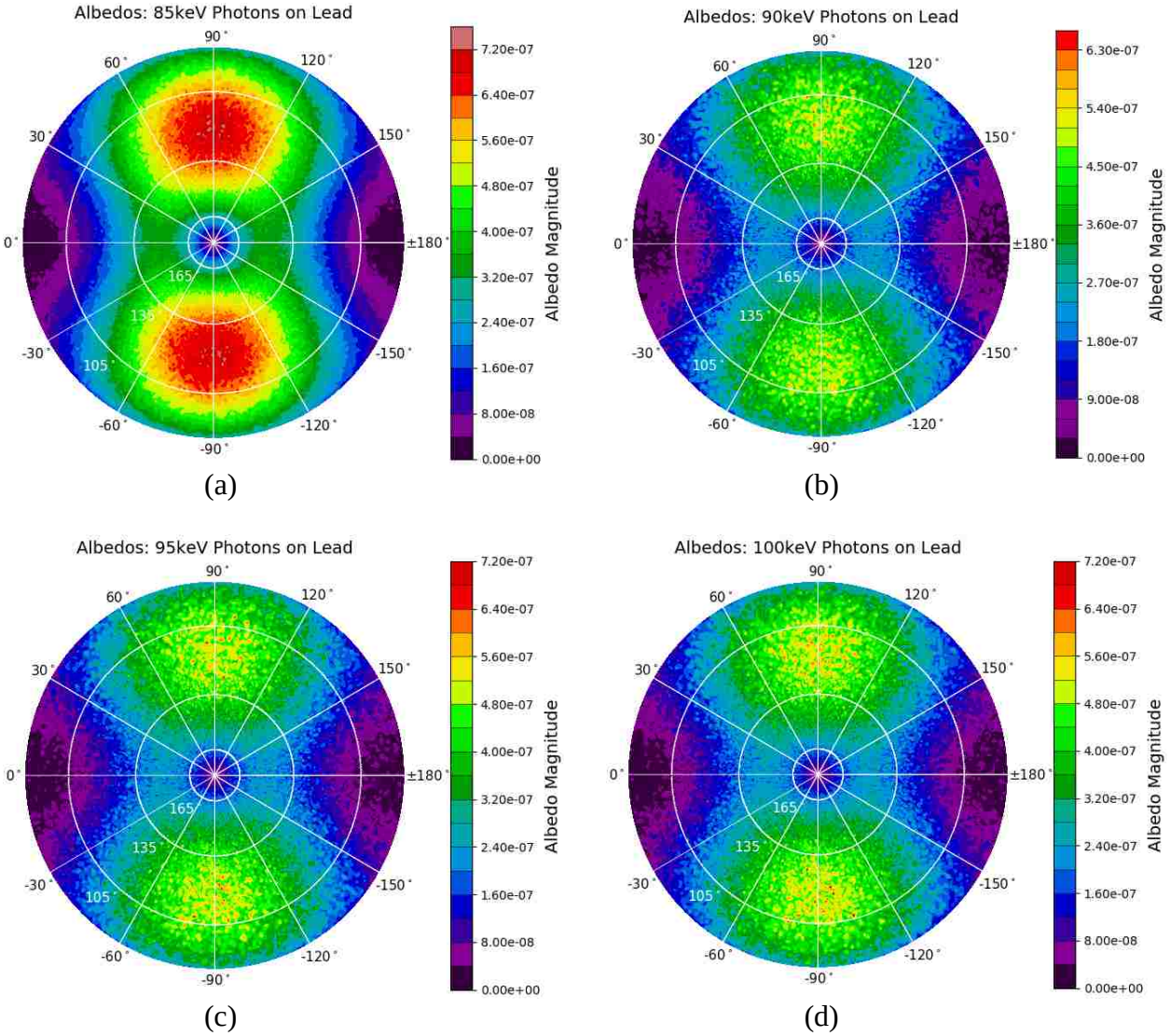

Figure 4.5. Albedos for a beam of 85 keV (a) polarized x-rays incident on slabs of lead with fluorsence emission enabled in the attenuation setup simulation. Albedos for beams of 90 keV (b), 95 keV (c), and 100 keV (d) polarized x-rays incident on slabs of lead with fluorsence emission disabled in the attenuation setup simulation. All plots are on the same color scale. Note the disapperance of the symmetric pattern with fluorescence disabled, but that the polarization-based asymmetry is still present. See Figure 3.1. for summary of plot annotations.

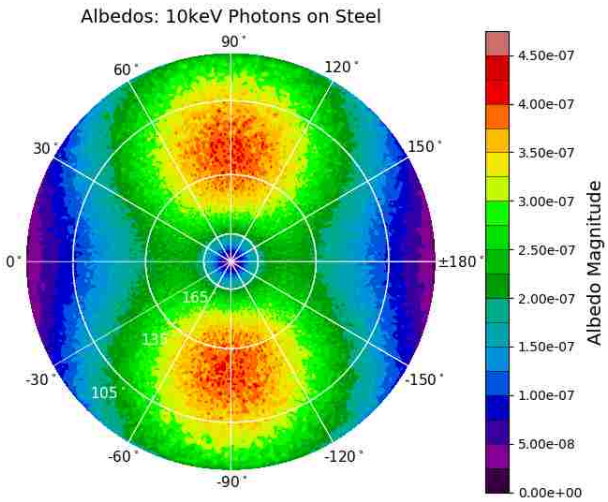

Figure 4.6. Albedos for a beam of 10 keV polarized x-rays incident on slabs of steel. Note that a symmetric pattern is not evident despite an iron K-edge at 7.1 keV; this is likely due to strong self-attenuation of the fluorescence x-rays in the steel. See Figure 3.1. for summary of plot annotations.

Table 4.1. Description of key locations relative to the primary barrier's surface normal.

Polar Angle, θ (°)	**Azimuthal Angle, ϕ (°)**	**Key Location Description**
0	0	Upstream wall midpoint
30	90	Middle roof, upstream wall
30	45	Junction of roof, lateral, and upstream wall, top corner
30	0	Junction of roof, lateral, and upstream wall, midpoint
30	-45	Junction of roof, lateral, and upstream wall, bottom corner
30	-90	Middle floor, upstream wall
60	90	Roof midpoint
60	45	Junction of roof and lateral wall midpoint
60	0	Lateral wall midpoint
60	-45	Junction of floor and lateral wall midpoint
60	-90	Floor midpoint
90	90	Middle roof, downstream wall
90	45	Junction of roof, lateral, and downstream wall, top corner
90	0	Junction of roof, lateral, and downstream wall, midpoint
90	-45	Junction of roof, lateral, and downstream wall, bottom corner
90	-90	Middle floor, upstream wall

Table 4.2. Maximum albedos at one meter from the center of a concrete primary barrier for a beam size of 100x2-mm^2. Multiply each entry by the multiplication factor found in the "Multiply" row.

0 Degree Incidence	**Angle of Reflection (measured from the normal) from Concrete Primary Barrier represented by Polar (θ) and Azimuthal (ϕ) Angles**															
θ (°)	**0**	**30**	**30**	**30**	**30**	**30**	**60**	**60**	**60**	**60**	**60**	**90**	**90**	**90**	**90**	**90**
ϕ (°)	**0**	**90**	**45**	**0**	**-45**	**-90**	**90**	**45**	**0**	**-45**	**-90**	**90**	**45**	**0**	**-45**	**-90**
Multiply	10e-7	10e-6	10e-6	10e-6	10e-6	10e-6	10e-6	10e-6	10e-6	10e-6	10e-6	10e-7	10e-7	10e-8	10e-7	10e-7
Energy (keV)																
10	0.09	0.26	0.19	0.15	0.18	0.25	0.32	0.17	0.03	0.18	0.28	1.94	1.04	1.95	1.21	2.01
15	0.05	0.46	0.38	0.30	0.38	0.44	0.62	0.38	0.10	0.35	0.63	3.03	1.58	1.61	1.71	3.17
20	0.17	0.69	0.61	0.49	0.57	0.70	0.94	0.56	1.76	0.55	0.93	3.52	1.85	1.37	1.95	3.71
25	0.25	1.06	0.84	0.72	0.87	1.07	1.32	0.82	3.19	0.84	1.40	3.63	2.16	2.34	1.73	3.57
30	0.42	1.42	1.18	1.05	1.26	1.40	1.90	1.19	4.79	1.17	1.90	3.67	1.89	2.69	1.98	3.61
35	0.30	1.93	1.63	1.44	1.64	1.86	2.45	1.67	6.93	1.60	2.60	3.82	2.21	2.49	1.87	3.77
40	0.51	2.47	2.13	1.82	2.12	2.50	3.26	2.16	9.51	2.08	3.40	3.86	2.04	2.64	2.08	4.00
45	0.63	3.10	2.72	2.38	2.70	3.06	4.12	2.68	1.27	2.63	4.12	4.34	2.50	3.24	2.19	4.22
50	0.58	3.71	3.28	2.85	3.31	3.77	4.94	3.17	1.51	3.14	5.01	4.52	2.38	4.53	2.32	4.92
55	0.66	4.29	3.80	3.40	3.66	4.32	5.64	3.81	1.82	3.70	5.58	4.73	2.47	3.33	2.50	4.79
60	0.97	4.79	4.34	3.81	4.37	4.84	6.39	4.26	2.15	4.22	6.36	5.10	2.54	4.58	2.41	4.85
65	0.89	5.45	4.76	4.26	4.87	5.46	6.96	4.80	2.47	4.69	7.17	5.00	2.76	5.07	2.86	5.27
70	1.04	5.89	5.25	4.70	5.19	5.83	7.63	5.23	2.62	5.19	7.72	5.04	2.87	5.11	2.99	4.85
75	1.11	6.25	5.59	4.96	5.65	6.22	8.27	5.61	3.05	5.61	8.06	5.44	3.00	5.45	2.97	5.27
80	1.21	6.54	5.99	5.30	5.93	6.53	8.83	5.88	3.15	6.02	8.74	5.34	3.18	5.75	3.10	5.44
85	1.29	7.01	6.25	5.51	6.26	6.89	9.04	6.17	3.45	6.27	9.11	5.39	3.22	6.18	3.12	5.08
90	1.32	7.13	6.51	5.86	6.46	7.21	9.38	6.58	3.62	6.40	9.20	5.61	3.27	5.56	3.28	5.80
95	1.43	7.44	6.75	5.95	6.69	7.44	9.59	6.85	3.77	6.55	9.79	5.59	3.35	7.54	3.07	5.66
100	1.44	7.52	6.96	6.24	6.77	7.52	9.80	6.79	3.96	6.86	9.81	5.69	3.41	7.50	3.12	5.67

Table 4.3. Maximum albedos at one meter from the center of a lead primary barrier for a beam size of 100x2-mm^2. Multiply each entry by the multiplication factor found in the "Multiply" row.

0 Degree Incidence	**Angle of Reflection (measured from the normal) from Lead Primary Barrier represented by Polar (θ) and Azimuthal (ϕ) Angles**															
θ (°)	**0**	**30**	**30**	**30**	**30**	**30**	**60**	**60**	**60**	**60**	**60**	**90**	**90**	**90**	**90**	**90**
ϕ (°)	**0**	**90**	**45**	**0**	**-45**	**-90**	**90**	**45**	**0**	**-45**	**-90**	**90**	**45**	**0**	**-45**	**-90**
Multiply	10e-8	10e-7	10e-7	10e-7	10e-7	10e-7	10e-7	10e-7	10e-7	10e-7	10e-7	10e-7	10e-7	10e-8	10e-7	10e-7
Energy (keV)																
10	0.39	2.73	1.95	1.59	2.17	2.82	3.46	2.05	0.37	2.23	3.11	1.97	1.00	1.89	1.01	2.12
15	2.00	8.72	7.59	7.04	8.43	8.58	11.25	9.64	6.92	9.23	11.28	3.46	1.83	4.08	2.04	2.97
20	1.54	9.09	8.30	7.35	8.29	8.56	11.40	9.38	7.17	9.26	12.07	3.40	1.90	4.63	1.97	3.56
25	1.12	6.67	6.09	5.75	6.10	6.30	8.67	6.65	4.46	6.56	8.46	3.34	2.00	4.03	1.65	3.84
30	0.90	5.16	5.01	4.29	4.91	5.92	6.84	5.21	2.90	4.76	6.70	3.16	1.70	3.96	1.54	2.88
35	1.32	4.89	4.40	3.43	4.14	4.67	6.50	4.24	1.96	4.47	6.60	3.07	1.49	2.92	1.67	2.83
40	0.48	4.78	3.64	3.26	4.22	4.61	6.78	4.07	1.57	4.09	5.91	3.32	1.79	1.69	1.61	2.84
45	0.50	4.41	3.75	2.86	3.54	3.89	5.72	3.82	1.37	3.87	6.18	3.20	1.51	1.96	1.64	2.57
50	1.08	4.27	3.26	2.85	3.29	3.96	5.84	3.68	1.39	3.72	6.00	2.84	1.56	1.63	1.71	2.84
55	0.74	4.13	3.56	3.10	3.70	4.34	5.84	3.82	1.34	3.47	6.19	2.89	1.56	2.09	1.49	2.87
60	0.83	4.18	3.34	2.93	3.52	3.90	6.33	3.98	1.42	3.84	6.39	2.73	1.49	2.22	1.47	2.74
65	0.38	4.18	3.66	2.86	3.25	4.34	6.18	3.84	1.33	3.75	6.37	2.94	1.44	1.61	1.49	2.78
70	0.75	4.79	3.97	3.23	3.71	4.18	6.13	4.05	1.55	3.59	6.63	2.49	1.48	2.49	1.27	2.70
75	1.50	4.64	3.85	3.02	3.62	4.34	6.50	4.07	1.43	3.97	6.69	2.86	1.37	1.37	1.42	2.54
80	1.10	4.83	3.75	3.30	3.94	4.44	6.36	3.93	1.43	4.38	6.57	2.49	1.47	2.13	1.35	2.80
85	0.61	4.12	3.77	3.07	4.12	4.72	6.94	4.48	1.54	4.23	7.39	2.53	1.27	2.66	1.34	2.53
90	10.85	58.17	58.52	55.85	57.69	58.63	86.27	83.90	82.06	82.99	85.06	6.39	5.34	43.93	5.57	6.75
95	7.74	54.15	53.66	52.16	54.18	54.20	78.11	75.72	73.60	75.83	76.27	5.91	4.43	36.33	4.79	5.67
100	9.90	49.96	48.57	50.34	49.02	49.67	70.56	67.94	66.69	67.63	69.65	5.50	4.27	31.23	4.49	5.45

Table 4.4. Maximum albedos at one meter from the center of a steel primary barrier for a beam size of 100x2-mm^2. Multiply each entry by the multiplication factor found in the "Multiply" row.

0 Degree Incidence	**Angle of Reflection (measured from the normal) from Steel Primary Barrier represented by Polar (θ) and Azimuthal (ϕ) Angles**															
θ (°)	**0**	**30**	**30**	**30**	**30**	**30**	**60**	**60**	**60**	**60**	**60**	**90**	**90**	**90**	**90**	**90**
ϕ (°)	**0**	**90**	**45**	**0**	**-45**	**-90**	**90**	**45**	**0**	**-45**	**-90**	**90**	**45**	**0**	**-45**	**-90**
Multiply	10e-8	10e-7	10e-7	10e-7	10e-7	10e-7	10e-6	10e-7	10e-7	10e-7	10e-6	10e-7	10e-7	10e-8	10e-7	10e-7
Energy (keV)																
10	0.36	3.01	2.54	2.24	2.72	2.92	0.39	2.61	1.37	2.78	0.41	2.24	1.23	2.34	1.10	2.14
15	0.91	3.75	2.79	2.34	3.18	3.22	0.53	3.01	0.94	2.73	0.44	2.53	1.65	1.93	1.48	3.09
20	0.70	3.51	2.97	2.34	3.14	3.71	0.53	2.86	0.88	3.13	0.50	2.96	1.67	2.10	1.64	3.01
25	0.55	4.03	3.30	2.35	3.48	3.97	0.51	3.17	0.98	3.01	0.53	3.02	1.92	2.82	1.66	3.19
30	0.55	4.15	3.65	2.48	3.38	3.93	0.60	3.44	0.87	3.40	0.57	3.23	2.05	1.73	1.88	3.06
35	0.71	4.44	3.77	3.07	3.86	4.75	0.66	3.43	1.26	3.90	0.59	3.18	1.75	1.38	1.49	3.04
40	1.41	4.96	4.09	3.46	3.94	5.27	0.79	4.49	1.50	4.38	0.72	3.02	1.74	2.66	1.69	3.27
45	0.84	5.68	4.73	3.85	4.69	5.57	0.78	5.05	1.52	4.80	0.80	3.13	1.52	1.66	1.51	3.08
50	1.51	6.15	5.66	4.50	5.60	6.39	0.89	5.53	2.39	5.84	0.90	2.84	1.60	2.39	1.66	2.74
55	1.57	7.54	6.19	5.14	6.47	7.41	1.08	6.67	2.34	6.28	1.05	3.23	1.61	2.05	1.52	3.15
60	1.44	8.43	7.74	6.27	7.58	8.31	1.16	7.74	2.81	7.12	1.18	2.96	1.43	2.14	1.47	2.79
65	1.10	9.00	8.35	7.35	8.32	10.03	1.35	8.59	3.31	8.36	1.36	2.81	1.61	2.02	1.49	2.91
70	2.06	10.77	9.66	7.93	9.37	10.83	1.56	9.40	3.80	9.48	1.59	3.04	1.71	1.87	1.56	3.15
75	2.86	11.69	10.78	8.63	10.33	11.91	1.67	10.69	4.44	10.71	1.62	3.12	1.66	1.22	1.43	2.89
80	1.89	12.62	10.72	9.70	11.37	12.62	1.87	11.96	4.76	11.83	1.83	2.74	1.54	2.44	1.56	2.92
85	2.77	13.55	12.41	10.58	11.94	13.52	2.00	12.90	5.54	12.56	1.99	3.03	1.68	2.00	1.52	3.08
90	3.46	14.98	13.46	11.16	13.27	15.19	2.15	13.91	5.75	14.16	2.14	3.24	1.65	2.15	1.53	3.60
95	3.39	16.20	14.18	12.32	14.45	16.00	2.39	14.92	7.05	14.92	2.31	3.24	1.58	2.75	1.51	3.23
100	2.93	17.02	15.83	12.80	15.18	17.33	2.51	16.29	7.34	16.75	2.52	3.42	1.64	2.32	1.60	3.33

Chapter 5. Specific Aim 3: Determination of Tenth Value Layers

5.1. Methods and Materials: Python Analysis

A Python script was written to determine the primary TVLs of NIST-defined concrete, lead, and NIST-defined steel as well as the secondary TVLs for lead and steel for incident primary x-ray synchrotron beamline energies between 10 keV and 100 keV in 5 keV increments. The attenuation setup in GEANT4 (Section 2.2) was used to determine the primary TVLs for monoenergetic primary beams while the secondary TVLs came from the polyenergetic spectrum of scattered radiation (Section 2.1). The resulting TVLs represent a broad-beam transmission geometry, as appropriate for shielding calculations.

As stated in Section 2.2, the TVL files recorded the number of photons and the total energy fluence that crossed each of the target material planes. Within the Python script, the TVL file for each simulated energy was opened and the data were read into appropriate variables. This process was repeated for all data files for the one billion events at each primary energy, creating two summed arrays. The two summed arrays, one for number of particles and one for energy fluence, each had a length of 50, i.e. the number of material planes in the block of material.

Once all the data files from a simulation were read in, the total energy fluence of the incident beam was calculated as:

$$\text{Total Energy Fluence of the Incident Beam} = \sum_{E=0}^{E_{max}} N_E * E \qquad \text{[Eq. 9]}$$

where N_E is the total number of photons that were simulated at energy E, E is the energy of the simulated photon, and E_{max} is the maximum energy a simulated photon could have in the simulation run. For monoenergetic beams, all simulated photons possessed the same incident energy, E_{max}.

Once the total energy fluence for an incident beam was calculated, the energy fluence was multiplied by 0.1 to obtain one tenth of said energy fluence; i.e. the resulting energy fluence after passing through the first TVL (TVL_1) of shielding material. Attenuation of a beam through a block of material follows the exponential function:

$$I = I_0 e^{-\mu x} = I_0 10^{-\frac{x}{TVL}} \quad \text{[Eq. 10]}$$

where I_0 is the intensity of the radiation before entering the material, μ is the linear attenuation coefficient, TVL is the corresponding thickness of one tenth value layer of material, and x is the thickness of the material the radiation has traveled though. Thus, the depth of each scoring plane in the block of material was specified at a logarithmic spacing of:

$$x_i = \omega_0 \, 10^{\frac{i}{B}} - \omega_0 \quad \text{[Eq. 11]}$$

where i ranged from 1 to 50, ω_0 was an offset of 10^{-5} m, and B had a value of 10. The thickness of the first TVL was interpolated from the transmission data generated by the attenuation setup simulations using the relationship:

$$x_{TVL} = x_1 + \frac{\ln(I_{TVL}/I_1)}{\ln(I_2/I_1)}(x_2 - x_1) \quad \text{[Eq. 12]}$$

where x_1 was the depth of the material plane whose energy fluence was above one tenth of the beam's incident energy fluence, x_2 was the depth of the next material plane whose energy fluence was below one tenth of the beam's incident energy fluence, I_{TVL} was the target value of one tenth of the beam's incident energy fluence, I_1 was the beam's energy fluence at the upper bounding material plane x_1, and I_2 was the beam's energy fluence at the lower bounding material plane x_2. This methodology was repeated to determine the second (TVL_2), third (TVL_3), and fourth (TVL_4) TVLs where the target energy fluence at each corresponding depth was an additional factor of ten smaller. The values of TVL_1, TVL_2, TVL_3, and TVL_4 were then stored for subsequent analysis.

5.2. TVL Results

Figure 5.1. compares TVL_1 of monoenergetic primary beams for concrete, lead, and steel verses primary beam energy; Figure 5.2. shows an enlarged view of Figure 5.1. for lead and steel. As expected, the TVL_1s for the various materials generally increase with increasing energy. However, upon crossing the K-edge of a shielding material, such as at 88 keV for lead, the TVL_1 drops significantly. At 88 keV, lead's mass attenuation coefficient for photoelectric absorption jumps from 1.547 $cm^2\ g^{-1}$ to 7.321 $cm^2\ g^{-1}$ (Berger 2010). This enhances the effectiveness of the shielding material just above the K-edge.

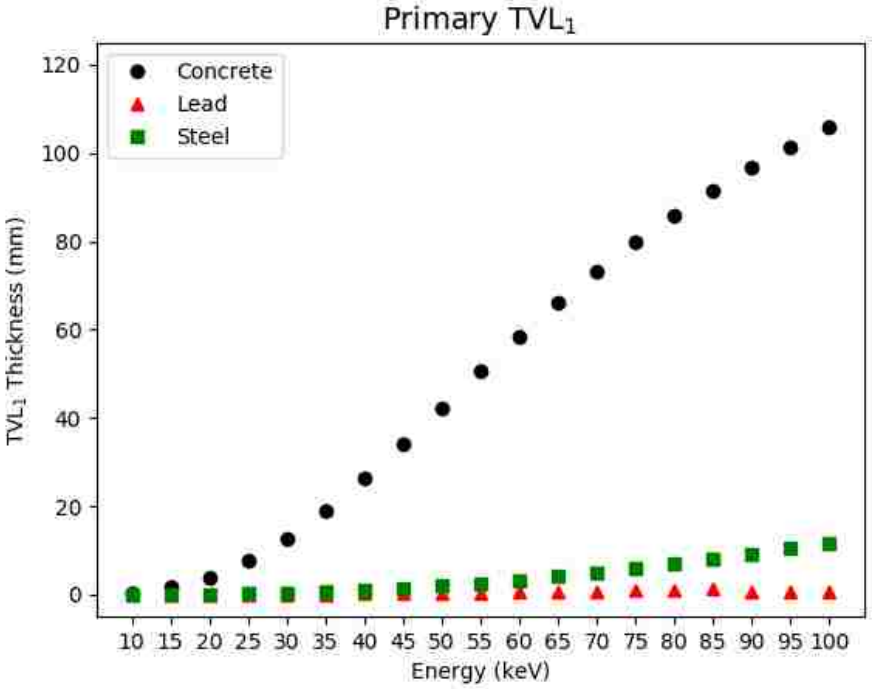

Figure 5.1. Plot of the magnitudes of the primary TVL_1s for concrete (circle), lead (triangle), and steel (square) verses primary beam energy.

Under broad-beam geometry, buildup and spectral effects mean that a material's rate of attenuation is not consistent. The second TVL is generally slightly smaller than the first TVL due to the geometry of the beam itself (Attix 1986). At depth, the attenuation behavior approaches a steady-state value called the equilibrium TVL, TVL_e. This effect is seen in Figure 5.3., which displays the primary beam's TVL_1 through TVL_4 in concrete, lead, and steel.

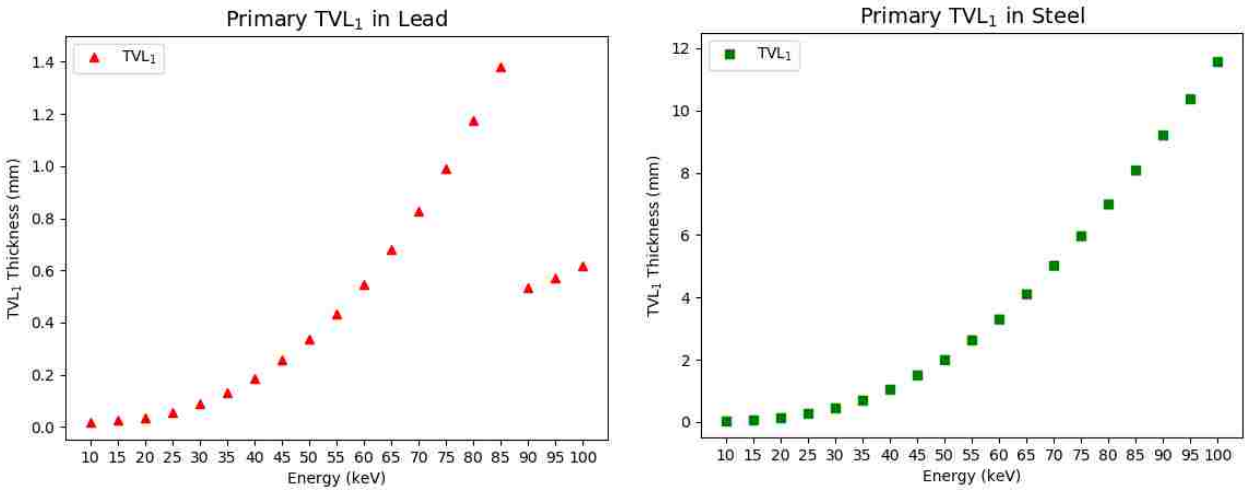

(a) (b)

Figure 5.2. Enlarged views of the magnitudes of the primary TVL_1s for lead (a) and steel (b) verses primary beam energy. TVLs increase with x-ray energy as expected until one exceeds the K-edge of the shielding material. Above the K-edge, photoelectric absorption enhances the effectiveness of the shielding material. All data points for steel are above the K-edge of iron at 7.1 keV.

In Figure 5.3. (c), one sees that the pattern of change in the TVLs for primary beam energies above the K-edge (e.g. 90 keV, 95 keV, and 100 keV) do not follow the same relationship as below the K-edge. Specifically, the deeper TVLs are larger than the shallower TVLs due to two effects. The first effect is production of fluorescence x-rays subsequent to absorption of a primary photon by the photoelectric effect. Because the vacancy in the K-shell can be filled by any of the outer shell electrons, these fluorescence photons also have a spectrum of energies. This causes the second effect, which is that beam hardening occurs, i.e. the more rapid attenuation of lower energy photons compared to higher energy photons. Therefore, photoelectric absorption enhances the effectiveness of the shielding material above the K-edge, but it also introduces more fluorescence x-rays which must be attenuated. (Attix 1986, Khan 2014)

The same patterns and relationships as previously mentioned for the primary TVLs generally hold true for the secondary TVLs. Figure 5.4., Figure 5.5., and Figure 5.6. show the secondary TVLs in lead and steel. Recall the polyenergetic spectra used to determine secondary

TVLs was modeled from the energies of scattered photons from water (Section 3.3). Secondary TVLs were not determined for concrete because it is not a typical shielding material for secondary radiation in synchrotron beamline hutches. Lastly, Figure 5.7. compares the primary TVL_1 and secondary TVL_1 for lead and steel verses primary beam energy. Except above the K-edge of lead, the primary TVL_1 is typically larger that the secondary TVL_1 at each energy. Table 5.1. summarizes the TVL results for primary and secondary TVL_1 and TVL_e for all materials.

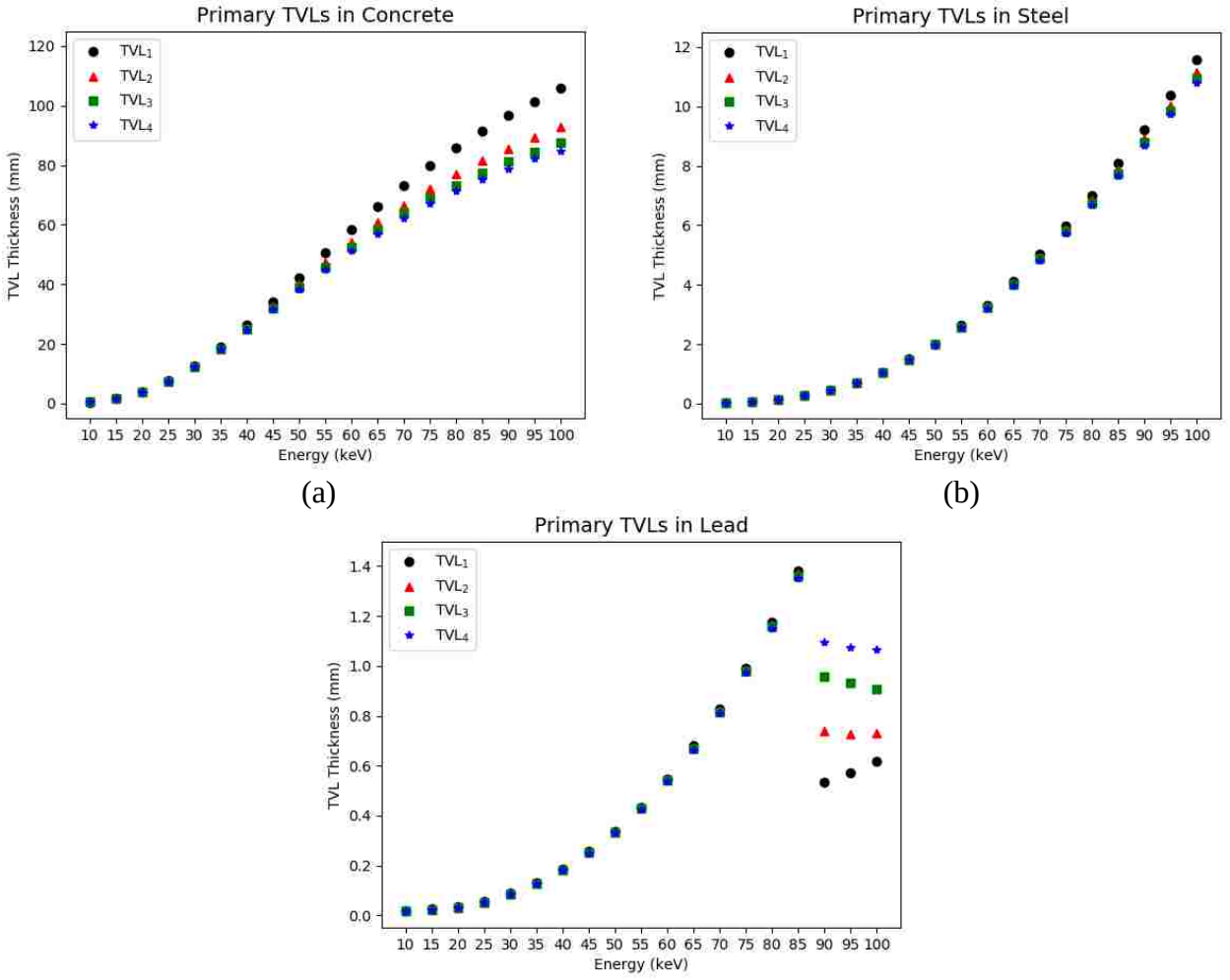

Figure 5.3. Plots of the magnitudes of TVL_1 (circle), TVL_2 (triangle), TVL_3 (square), and TVL_4 (star) of primary x-rays for concrete (a), steel (b), and lead (c) verses primary beam energy. The TVLs at greater depths decrease in magnitude relative to shallower depths. Note the effect in lead (c) of crossing the K-edge of the shielding material.

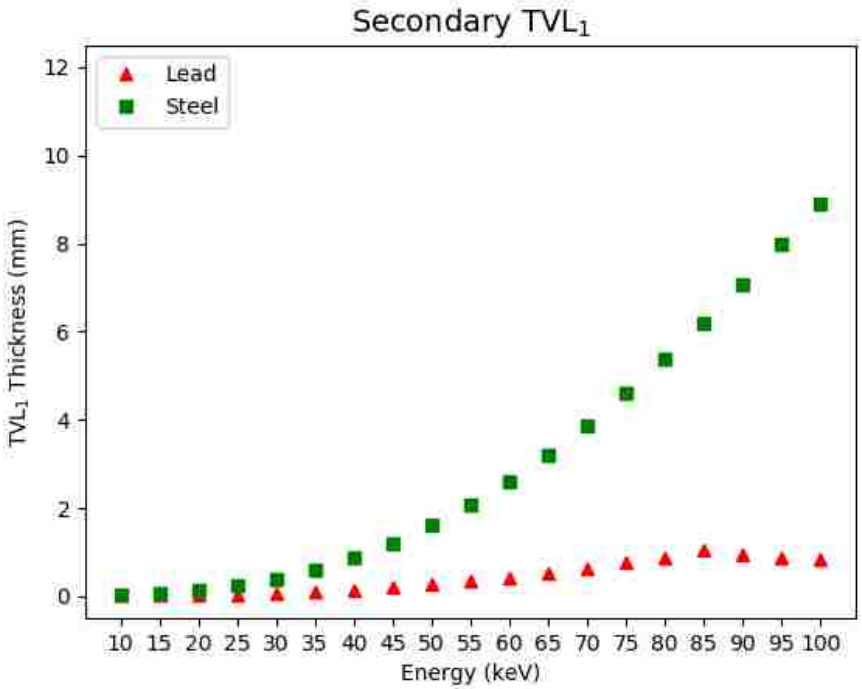

Figure 5.4. Plot of the magnitudes of the secondary TVL_1s for lead (triangle) and steel (square) verses primary beam energy.

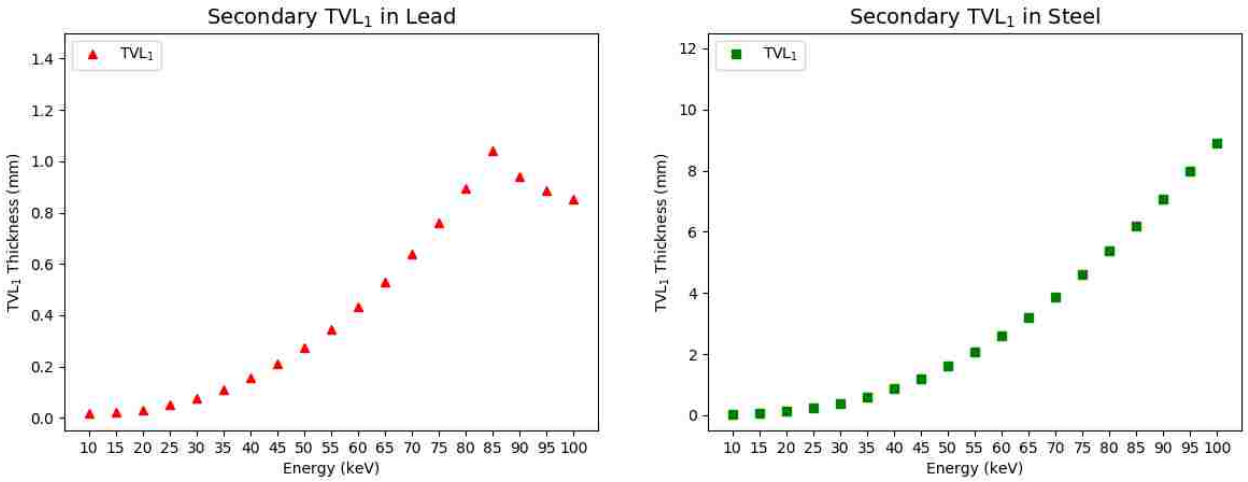

(a) (b)

Figure 5.5. Individual views of the magnitudes of the secondary TVL_1s for lead (a) and steel (b) verses primary beam energy. TVLs increase with x-ray energy as expected until one exceeds the K-edge of the shielding material. Above the K-edge, photoelectric absorption enhances the effectiveness of the shielding material. All data points for steel are above the K-edge of iron at 7.1 keV.

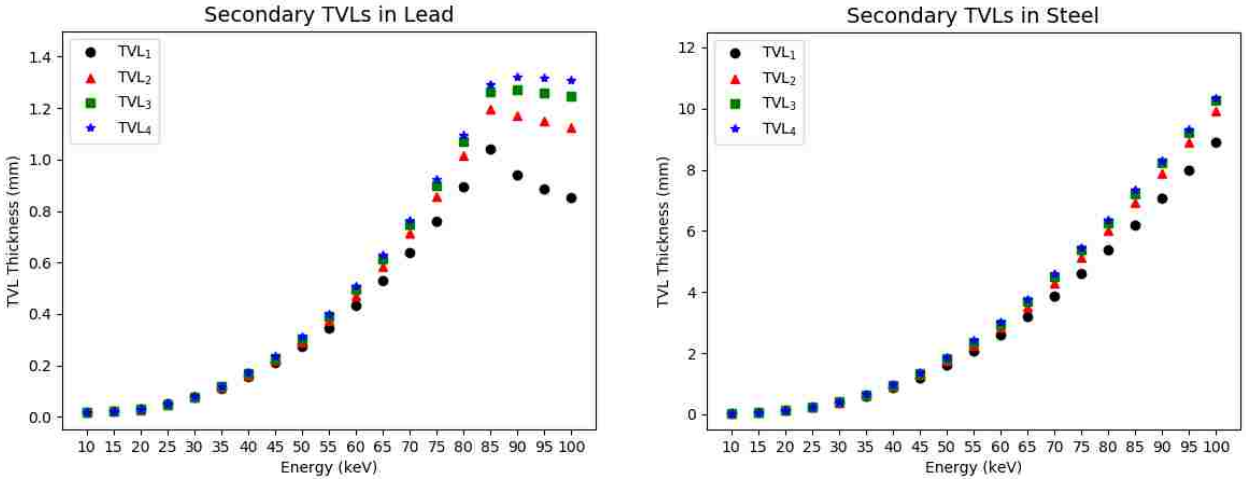

(a) (b)

Figure 5.6. Plots of the magnitudes of TVL_1 (circle), TVL_2 (triangle), TVL_3 (square), and TVL_4 (star) of secondary x-rays for lead (a) and steel (b) verses primary beam energy. The TVLs at greater depths increase in magnitude relative to shallower depths. Note the effect in lead (a) of crossing the K-edge of the shielding material.

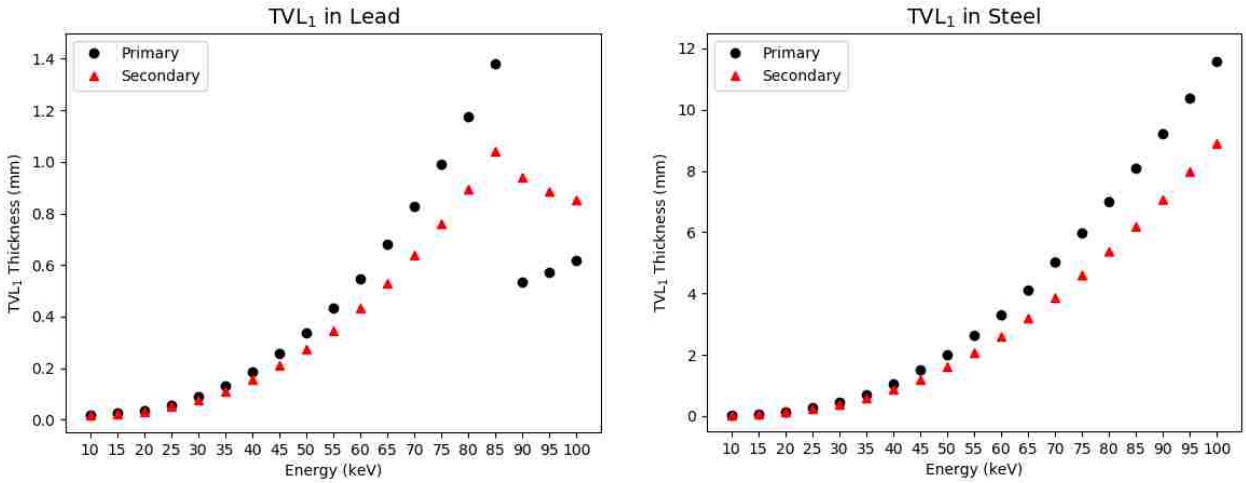

(a) (b)

Figure 5.7. Plots of the magnitudes of the primary TVL_1 (circle) and secondary TVL_1 (triangle) for lead (a) and steel (b) verses primary beam energy.

Table 5.1. Primary and secondary barrier TVL_1 and TVL_e (mm) for concrete, lead, and steel.

	Concrete		Lead				Steel			
	Primary TVLs		Primary TVLs		Secondary TVLs		Primary TVLs		Secondary TVLs	
Energy (keV)	TVL_1	TVL_e	TVL_1	TVL_e	TVL_1	TVL_e	TVL_1	TVL_e	TVL_1	TVL_e
10	0.5	0.5	0.02	0.02	0.02	0.02	0.02	0.02	0.02	0.02
15	1.7	1.8	0.03	0.02	0.02	0.02	0.07	0.07	0.06	0.06
20	4.0	4.1	0.03	0.03	0.03	0.03	0.14	0.14	0.13	0.13
25	7.6	7.6	0.06	0.05	0.05	0.05	0.27	0.27	0.24	0.25
30	12.6	12.5	0.09	0.09	0.08	0.08	0.46	0.45	0.39	0.41
35	18.9	18.5	0.13	0.13	0.11	0.12	0.72	0.71	0.60	0.65
40	26.2	25.4	0.19	0.18	0.16	0.17	1.06	1.06	0.87	0.96
45	34.2	32.8	0.26	0.25	0.21	0.23	1.50	1.49	1.21	1.35
50	42.4	40.2	0.34	0.33	0.27	0.30	2.02	2.00	1.61	1.82
55	50.5	47.4	0.44	0.43	0.35	0.39	2.62	2.60	2.07	2.36
60	58.3	54.2	0.55	0.54	0.43	0.50	3.30	3.26	2.59	2.97
65	66.0	60.7	0.68	0.67	0.53	0.61	4.12	4.06	3.19	3.69
70	73.2	66.6	0.83	0.81	0.64	0.75	5.02	4.93	3.86	4.50
75	79.8	72.1	0.99	0.98	0.76	0.90	5.98	5.86	4.59	5.37
80	85.8	77.0	1.18	1.17	0.89	1.07	7.01	6.84	5.37	6.27
85	91.5	81.5	1.38	1.37	1.04	1.26	8.09	7.88	6.20	7.22
90	96.7	85.6	0.53	0.96	0.94	1.27	9.22	8.94	7.08	8.21
95	101.4	89.3	0.57	0.93	0.89	1.26	10.39	10.04	7.98	9.22
100	105.8	92.9	0.62	0.91	0.85	1.25	11.59	11.15	8.91	10.25

Chapter 6. Discussion

6.1. Sample Calculations

The goal of this work was to provide shielding parameter data that allows NCRP-style calculation of shielding requirements for synchrotron x-ray beamline hutches. To illustrate how the results of this thesis could be utilized, this section provides sample calculations for primary barrier thickness and lateral wall shielding thickness. Assumptions for input parameters are illustrative and may not represent actual operating conditions of an x-ray beamline.

For the synchrotron beamline hutch, illustrated in Figure 6.1., a primary beam of horizontally-polarized, monoenergetic photons enters the hutch through the upstream wall, passes through the beamline target, and strikes the primary barrier on the hutch's downstream wall. The calculations assume a 40-hour work week with a primary beam energy of 70 keV and an average dose rate of 10 Gy/hr. The workload, W, is defined as the time integral of the absorbed-dose rate of the primary beam (NCRP 2005), which simplifies for this example to:

$$W = D\ (\mathrm{Gy\ hr^{-1}}) * t\ (\mathrm{hr\ wk^{-1}}) \qquad \text{[Eq. 13]}$$

corresponding to a workload of 400 Gy/wk.

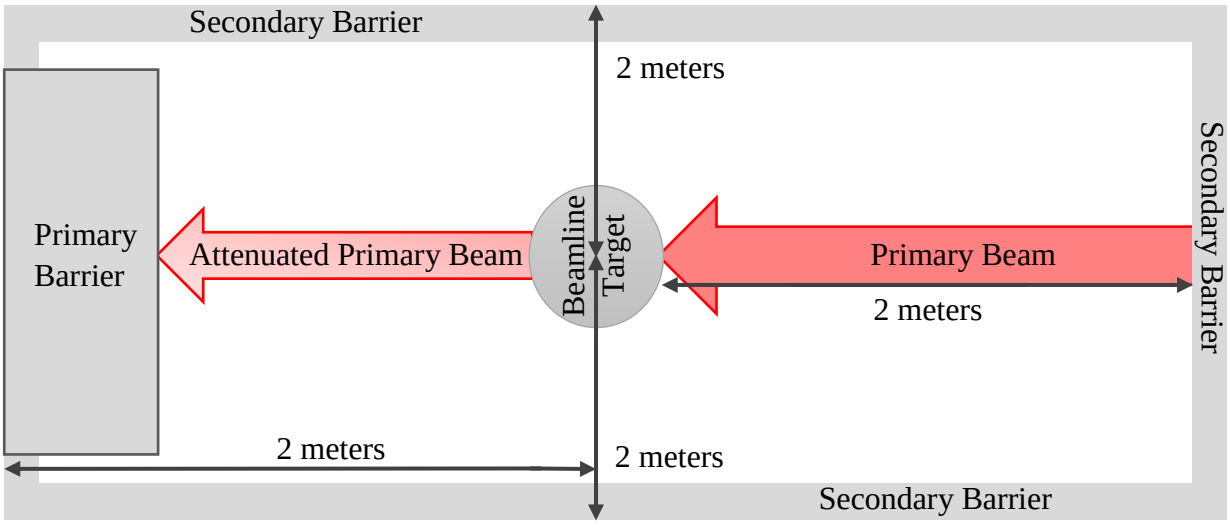

Figure 6.1. Overhead view of the synchrotron beamline hutch used in the sample calculations. The hutch is 2.1 m tall, with the beamline 1.1 m above the floor. The drawing is not to scale.

Assume the maximally-exposed individual is a radiation worker, for instance a researcher who is monitoring an experiment from outside the hutch. Consequently, the area is treated as a controlled area with a shielding design goal, P, of 5 mSv/yr or 0.1 mSv/wk (NCRP 2005). Furthermore, assume this individual is present for the full work week, so the occupancy factor, T, is 1. Lastly, the point of protection is specified at 0.3 m beyond any barrier (NCRP 2005).

6.1.1. Primary Barrier Calculation

For a synchrotron beamline, the primary beam is at a fixed orientation. This means that the use factor, U, which is the ratio of the time that the primary beam is directed towards the primary barrier (or beam stop) to the total amount of time that the beam is on (NCRP 2005), is 1.

The transmission factor, B_{pri}, and number of TVLs, n, needed for the primary barrier to attenuate the beam to the design goal are given by:

$$B_{pri} = \frac{P\, d_{pri}^2}{WUT} \qquad \text{[Eq. 14]}$$

$$n = -\log\left(B_{pri}\right) \qquad \text{[Eq. 15]}$$

where d_{pri} is normally specified as the distance from the source to the point of protection at 0.3 m beyond the primary barrier (NCRP 2005). However, synchrotron x-ray beams exhibit very little divergence, so a $1/r^2$ correction is inappropriate. For simplicity in this example, the workload, W, is assumed to be defined at a point in the hutch such that d_{pri} has a value of 1 m. Calculating from Equation 14 and Equation 15, B_{pri} and n, have values of:

$$B_{pri} = \frac{P\, d_{pri}^2}{WUT} = \frac{\left(0.1\,\frac{\text{mSv}}{\text{wk}}\right) * \ (1\ \text{m})^2}{\left(400000\,\frac{\text{mGy}}{\text{wk}}\right) * (1) * (1)} = \ 2.5 * 10^{-7}$$

$$n = \ -\log\left(B_{pri}\right) = \ -\log(2.5 * 10^{-7}) = \sim 6.6$$

The total thickness of the primary barrier, $t_{barrier}$, is calculated from n and the TVLs of the shielding material by:

$$t_{barrier} = TVL_1 + (n-1) * TVL_e \quad \text{[Eq. 16]}$$

where TVL_1 and TVL_e are respectively the first and equilibrium tenth value layers of the material at the relevant primary beam energy (NCRP 2005). Table 5.1. gives TVL_1 and TVL_e values of concrete, lead, and steel at 70 keV, which are 73.2 mm and 66.6 mm in concrete, 0.83 mm and 0.82 mm in lead, and 5.02 mm and 4.93 mm in steel. From Equation 16, the required thickness of a primary barrier made from concrete, lead, or steel are 446 mm, 5.4 mm, or 33 mm respectively.

$$t_{barrier\,(concrete)} = TVL_1 + (n-1) * TVL_e = 73.2 \text{ mm} + (6.6-1) * 66.6 \text{ mm} = 446 \text{ mm}$$

$$t_{barrier\,(lead)} = TVL_1 + (n-1) * TVL_e = 0.83 \text{ mm} + (6.6-1) * 0.82 \text{ mm} = 5.4 \text{ mm}$$

$$t_{barrier\,(steel)} = TVL_1 + (n-1) * TVL_e = 5.02 \text{ mm} + (6.6-1) * 4.93 \text{ mm} = 33 \text{ mm}$$

6.1.2. Secondary Barrier Calculation for Lateral Wall

The lateral walls of the synchrotron hutch, which are secondary barriers, must attenuate both scatter from the target object and reflected radiation (albedo) from the primary barrier. One must determine the dose equivalents from these sources reaching the point of protection through the lateral wall. The calculations correspond to NCRP 151's vault door calculations, namely equation 2.11 for patient scatter and equation 2.9 for primary scatter, with several simplifying assumptions. First, as with d_{pri}, the workload W is assumed to be measured such that the distance from source to point of scattering (either target or primary barrier) is 1 m; attenuation by the target is also conservatively neglected. Second, the x-ray field size is assumed to be the same size (100x2-mm^2) as that used in this work to determine scatter fraction and albedo, so no field-size correction is needed. Third, because no maze and door are involved, some albedo, area, and distance terms can be disregarded from the NCRP 151 equations. Finally, the largest magnitudes for scatter

fraction and albedo incident on the wall surface will be used in the calculation, while also assuming the shortest distance d_{sec} to perpendicular incidence on the lateral wall. The barrier transmission factor for the lateral wall for both sources combined is therefore:

$$B_{sec} = \frac{P}{W(a+\alpha)T}\, d_{sec}^2 \qquad \text{[Eq. 17]}$$

where a is the scatter fraction, α is the albedo, d_{sec} is the perpendicular distance to the point of protection from the middle of the target or the primary barrier, i.e., 2.3 m, and W is the workload.

From the scatter fraction plots in Chapter 3 (and Figure B.13.), the most intense scatter incident on the lateral wall likely occurs near the junction of lateral wall, downstream wall, and roof, corresponding approximately to a polar angle of 45° and an azimuthal angle of 45° relative to the primary beam's incident direction; the scatter fraction at this location is 1.56 x 10^{-5} using Table 3.1. A similar assessment of the albedo plots in Chapter 4 (and Figure C.32.) for lead indicates the worst value at comparable polar and azimuthal angles; the albedo at this location is 3.97 x 10^{-7} using Table 4.3. Thus, the required secondary barrier transmission in lead for the lateral wall is:

$$B_{sec} = \frac{P}{W(a+\alpha)T}\, d_{sec}^2 = \frac{\left(0.1\,\frac{\text{mSv}}{\text{wk}}\right)}{\left(400000\,\frac{\text{mGy}}{\text{wk}}\right)(1.56 * 10^{-5} + 3.97 * 10^{-7})(1)}(2.3\text{ m})^2 = 0.083$$

Using Equation 15, the number of TVLs needed for the secondary barrier is:

$$n = -\log(B_{sec}) = -\log(0.083) = \sim 1.08$$

Using Table 5.1., the secondary TVL_1 and TVL_e in lead for 70 keV primary x-rays is 0.64 mm and 0.75 mm, so a secondary barrier composed of lead must be 0.70 mm (from Equation 16).

$$t_{barrier;\,lead} = TVL_1 + (n-1) * TVL_e = 0.64\text{ mm} + (1.08-1) * 0.75\text{ mm} = 0.70\text{ mm}$$

A similar calculation could be used to determine the required steel thickness, or the material thicknesses for a lead+steel laminated barrier.

The directional asymmetries in scatter fractions and albedos could be used to choose an optimal placement of the hutch door in the lateral wall. The section of wall receiving the least amount of radiation from scatter and albedo could be determined from the corresponding polar plots. Rather than shielding the door to the same worst-case level as the rest of the wall, a door placed at this optimal location would require the least possible amount of shielding, saving weight in the door and thus improving hutch utilization.

6.1.3. Additional Notes about Sample Calculations

The sample calculations assumed that a single x-ray energy is used on the beamline. While some synchrotron facilities might choose to shield a hutch for a single worst-case energy, one could easily calculate for more realistic usage patterns in terms of beam energy. For beamlines that operate at two principle beam energies, required shielding thicknesses could be calculated for each beam energy and its respective workload, then combined with the two-source rule of NCRP 151 to determine the final barrier thickness (NCRP 2005). Alternatively, one could develop a workload distribution method similar to that used in NCRP 147 for polyenergetic diagnostic x-ray beams (NCRP 2004). In this approach, one guesses the required material thickness and calculates the shielded dose equivalents at the point of protection for the workload at each energy; if the total shielded dose equivalent exceeds the design goal, one then repeats the process with a larger guess.

The sample calculations also assumed that one desired to shield the hutch for a design goal based on annual exposure limits. An alternative strategy is to shield the hutch to meet an “in any one hour” design goal (NCRP 2005); this may be required by the cognizant regulatory agency at some synchrotron facilities. In this case, one would use the instantaneous dose rate of the x-ray beam, rather than the average dose rate and weekly workload used in the sample calculations, in conjunction with an appropriate design goal such as “2 mrem in any one hour.”

6.2. Limitations

One limitation of this project was that it was purely simulation based, without experimental measurements to compare with the simulation results. The original project plan included a set of comparison measurements at Louisiana State University's synchrotron; experimental data could have been obtained using the same geometries that were simulated in GEANT4. An inconsistent operational status has delayed experimental verification to a future date.

Another limitation of this project was that it assumes that synchrotron x-ray beams are truly monoenergetic. In reality, beamline monochromators exhibit a finite bandpass; the monochromator design determines the level of polychromaticity. Similarly, over a typical operating period, a beamline could utilize a large variety of monoenergetic x-rays for a range of experiments.

Lastly, secondary TVLs were calculated only for the energy spectrum of photons scattered from the beamline target. Backscattered photons that influence albedo should generally have lower energies that side-, back-, and forward-scatter from the beamline target, so it was assumed that secondary TVLs based on scatter would be conservatively appropriate for albedos also. Figure 6.2. compares the energy spectrum of 100 keV photons scattered from the target to that of the backscattered photons from the primary barrier that determine albedo. One sees noticeably fewer high energy photons in the albedo energy spectrum compared to the target-scattered spectrum. Concrete was chosen over lead or steel for this comparison because its albedo values were higher. While this confirms that scatter-based secondary TVLs are conservatively safe to use for albedo, this choice results in an overestimate of shielding requirements. Albedo-based secondary TVLs would be straightforward to determine in the same fashion as the scatter-based TVLs, if one wished to account for the differences to potentially reduce the overall shielding thicknesses.

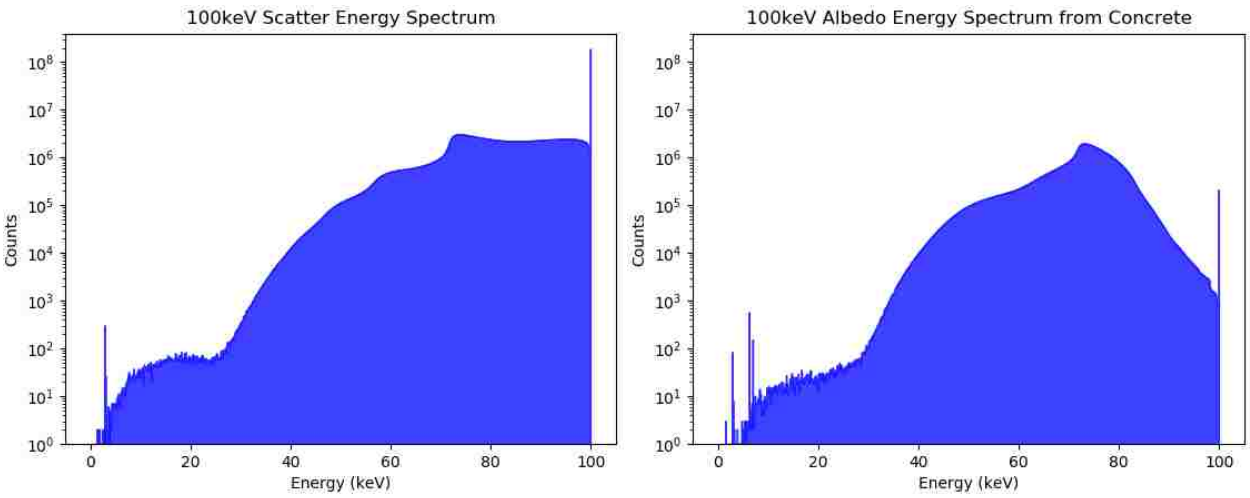

(a) (b)

Figure 6.2. Histograms of the energy spectra of photons scattered from the beamline target (a) and reflected (i.e., albedo) from a primary concrete barrier (b) for a primary beam energy of 100 keV.

6.3. Future Work

To produce a robust set of data to use for shielding design calculations for synchrotron x-ray hutches, several additions to the current work would be desirable. First, as noted in the previous section, experimental validation of the GEANT4 simulation models is desirable. Additional aspects are:

1. Determination of Workload: This work assumed that the qualified expert knows how to determine an appropriate value for workload of the primary beam energy (or energies) in the hutch, in Gy/week or similar. Such a value could be determined by direct measurement on a comparable existing beamline. Alternatively, workload could be estimated from the stored ring current, the x-ray production characteristics (e.g., field strength and number of poles) of a bending magnet or insertion device, and the characteristics of a beamline's monochromator. A future NCRP-style report for synchrotron x-ray beamline hutches should include guidance on appropriate determination of workload.

2. White-beam or pink-beam data: In some types of experiments, the use of a broad-spectrum x-ray beam is appropriate. In this case, TVLs, scatter fractions, and albedos for the broad-spectrum radiation would be useful to have for shielding design. In addition, for safety considerations, synchrotron facility managers may prefer that the primary beam stop be capable of attenuating the full white beam to acceptable levels, rather than just the monochromatized beam. In the case of failure of upstream beamline shutters or monochromator elements, the full white beam could potentially reach the hutch's primary beam stop.

3. Scaling of scatter fractions and albedos with beam area: This work modeled a relatively large beam area of 100x2-mm^2 and a scattering object that was only somewhat larger than the beam, to maximize the magnitudes of scatter and albedo. Because many x-ray beamlines routinely use smaller beam sizes, it could be useful to generate scatter fractions and albedos across a range of beam areas. This data would also show if scatter fractions and albedos scale with beam area, which is true in NCRP 151 for the substantially larger x-ray fields used in radiation therapy.

4. Occupancy: The literature does not appear to provide survey data about appropriate occupancies of areas around x-ray beamline hutches. The sample calculation in Section 6.1 assumed a 100% occupancy, which may well be excessively conservative based on experience working at a synchrotron facility (Matthews 2019). A survey of utilization and occupancy patterns at a variety of synchrotron facilities could be informative on this topic.

6.4. Conclusion

This work addresses the need for appropriate data to facilitate NCRP-style shielding design calculations for synchrotron x-ray beamline hutches. Synchrotron x-ray beams have several unique features that complicate the adaptation of existing shielding guidelines for diagnostic imaging and radiotherapy facilities to this purpose, namely monochromatic highly-polarized x-ray beams. This

work produced data on scatter fractions from water, as well as albedos for concrete, steel, and lead, and primary and secondary TVLs in these materials. With the addition of methodology for determining workloads and other synchrotron-specific operational details, along with experimental validation of the results presented here, this project enables the development of an NCRP-style shielding methodology to support radiation protection around x-ray beamline hutches.

Appendix A. Simulation Runs Produced in GEANT4 to Determine Shielding Parameters

Table A.1. GEANT4 simulations completed to determine shielding parameters.

Simulation Setup	Beam Spectrum	Primary Energy (keV)	Number of Events	Target Material	Shielding Parameter(s) Determined
Scatter	Monoenergetic	10	10^9	Water	Scatter Fractions
Scatter	Monoenergetic	15	10^9	Water	Scatter Fractions
Scatter	Monoenergetic	20	10^9	Water	Scatter Fractions
Scatter	Monoenergetic	25	10^9	Water	Scatter Fractions
Scatter	Monoenergetic	30	10^9	Water	Scatter Fractions
Scatter	Monoenergetic	35	10^9	Water	Scatter Fractions
Scatter	Monoenergetic	40	10^9	Water	Scatter Fractions
Scatter	Monoenergetic	45	10^9	Water	Scatter Fractions
Scatter	Monoenergetic	50	10^9	Water	Scatter Fractions
Scatter	Monoenergetic	55	10^9	Water	Scatter Fractions
Scatter	Monoenergetic	60	10^9	Water	Scatter Fractions
Scatter	Monoenergetic	65	10^9	Water	Scatter Fractions
Scatter	Monoenergetic	70	10^9	Water	Scatter Fractions
Scatter	Monoenergetic	75	10^9	Water	Scatter Fractions
Scatter	Monoenergetic	80	10^9	Water	Scatter Fractions
Scatter	Monoenergetic	85	10^9	Water	Scatter Fractions
Scatter	Monoenergetic	90	10^9	Water	Scatter Fractions
Scatter	Monoenergetic	95	10^9	Water	Scatter Fractions
Scatter	Monoenergetic	100	10^9	Water	Scatter Fractions
Attenuation	Monoenergetic	10	10^9	Concrete	Albedo / Primary TVLs
Attenuation	Monoenergetic	15	10^9	Concrete	Albedo / Primary TVLs
Attenuation	Monoenergetic	20	10^9	Concrete	Albedo / Primary TVLs
Attenuation	Monoenergetic	25	10^9	Concrete	Albedo / Primary TVLs
Attenuation	Monoenergetic	30	10^9	Concrete	Albedo / Primary TVLs
Attenuation	Monoenergetic	35	10^9	Concrete	Albedo / Primary TVLs
Attenuation	Monoenergetic	40	10^9	Concrete	Albedo / Primary TVLs
Attenuation	Monoenergetic	45	10^9	Concrete	Albedo / Primary TVLs
Attenuation	Monoenergetic	50	10^9	Concrete	Albedo / Primary TVLs
Attenuation	Monoenergetic	55	10^9	Concrete	Albedo / Primary TVLs
Attenuation	Monoenergetic	60	10^9	Concrete	Albedo / Primary TVLs
Attenuation	Monoenergetic	65	10^9	Concrete	Albedo / Primary TVLs
Attenuation	Monoenergetic	70	10^9	Concrete	Albedo / Primary TVLs
Attenuation	Monoenergetic	75	10^9	Concrete	Albedo / Primary TVLs
Attenuation	Monoenergetic	80	10^9	Concrete	Albedo / Primary TVLs
Attenuation	Monoenergetic	85	10^9	Concrete	Albedo / Primary TVLs
Attenuation	Monoenergetic	90	10^9	Concrete	Albedo / Primary TVLs
Attenuation	Monoenergetic	95	10^9	Concrete	Albedo / Primary TVLs
Attenuation	Monoenergetic	100	10^9	Concrete	Albedo / Primary TVLs

table cont'd.

Simulation Setup	Beam Spectrum	Primary Energy (keV)	Number of Events	Target Material	Shielding Parameter(s) Determined
Attenuation	Monoenergetic	10	10^9	Lead	Albedo / Primary TVLs
Attenuation	Monoenergetic	15	10^9	Lead	Albedo / Primary TVLs
Attenuation	Monoenergetic	20	10^9	Lead	Albedo / Primary TVLs
Attenuation	Monoenergetic	25	10^9	Lead	Albedo / Primary TVLs
Attenuation	Monoenergetic	30	10^9	Lead	Albedo / Primary TVLs
Attenuation	Monoenergetic	35	10^9	Lead	Albedo / Primary TVLs
Attenuation	Monoenergetic	40	10^9	Lead	Albedo / Primary TVLs
Attenuation	Monoenergetic	45	10^9	Lead	Albedo / Primary TVLs
Attenuation	Monoenergetic	50	10^9	Lead	Albedo / Primary TVLs
Attenuation	Monoenergetic	55	10^9	Lead	Albedo / Primary TVLs
Attenuation	Monoenergetic	60	10^9	Lead	Albedo / Primary TVLs
Attenuation	Monoenergetic	65	10^9	Lead	Albedo / Primary TVLs
Attenuation	Monoenergetic	70	10^9	Lead	Albedo / Primary TVLs
Attenuation	Monoenergetic	75	10^9	Lead	Albedo / Primary TVLs
Attenuation	Monoenergetic	80	10^9	Lead	Albedo / Primary TVLs
Attenuation	Monoenergetic	85	10^9	Lead	Albedo / Primary TVLs
Attenuation	Monoenergetic	90	10^9	Lead	Albedo / Primary TVLs
Attenuation	Monoenergetic	95	10^9	Lead	Albedo / Primary TVLs
Attenuation	Monoenergetic	100	10^9	Lead	Albedo / Primary TVLs
Attenuation	Monoenergetic	10	10^9	Steel	Albedo / Primary TVLs
Attenuation	Monoenergetic	15	10^9	Steel	Albedo / Primary TVLs
Attenuation	Monoenergetic	20	10^9	Steel	Albedo / Primary TVLs
Attenuation	Monoenergetic	25	10^9	Steel	Albedo / Primary TVLs
Attenuation	Monoenergetic	30	10^9	Steel	Albedo / Primary TVLs
Attenuation	Monoenergetic	35	10^9	Steel	Albedo / Primary TVLs
Attenuation	Monoenergetic	40	10^9	Steel	Albedo / Primary TVLs
Attenuation	Monoenergetic	45	10^9	Steel	Albedo / Primary TVLs
Attenuation	Monoenergetic	50	10^9	Steel	Albedo / Primary TVLs
Attenuation	Monoenergetic	55	10^9	Steel	Albedo / Primary TVLs
Attenuation	Monoenergetic	60	10^9	Steel	Albedo / Primary TVLs
Attenuation	Monoenergetic	65	10^9	Steel	Albedo / Primary TVLs
Attenuation	Monoenergetic	70	10^9	Steel	Albedo / Primary TVLs
Attenuation	Monoenergetic	75	10^9	Steel	Albedo / Primary TVLs
Attenuation	Monoenergetic	80	10^9	Steel	Albedo / Primary TVLs
Attenuation	Monoenergetic	85	10^9	Steel	Albedo / Primary TVLs
Attenuation	Monoenergetic	90	10^9	Steel	Albedo / Primary TVLs
Attenuation	Monoenergetic	95	10^9	Steel	Albedo / Primary TVLs
Attenuation	Monoenergetic	100	10^9	Steel	Albedo / Primary TVLs
Attenuation	Polyenergetic	10	10^9	Lead	Secondary TVLs
Attenuation	Polyenergetic	15	10^9	Lead	Secondary TVLs
Attenuation	Polyenergetic	20	10^9	Lead	Secondary TVLs
Attenuation	Polyenergetic	25	10^9	Lead	Secondary TVLs

table cont'd.

Simulation Setup	Beam Spectrum	Primary Energy (keV)	Number of Events	Target Material	Shielding Parameter(s) Determined
Attenuation	Polyenergetic	30	10^9	Lead	Secondary TVLs
Attenuation	Polyenergetic	35	10^9	Lead	Secondary TVLs
Attenuation	Polyenergetic	40	10^9	Lead	Secondary TVLs
Attenuation	Polyenergetic	45	10^9	Lead	Secondary TVLs
Attenuation	Polyenergetic	50	10^9	Lead	Secondary TVLs
Attenuation	Polyenergetic	55	10^9	Lead	Secondary TVLs
Attenuation	Polyenergetic	60	10^9	Lead	Secondary TVLs
Attenuation	Polyenergetic	65	10^9	Lead	Secondary TVLs
Attenuation	Polyenergetic	70	10^9	Lead	Secondary TVLs
Attenuation	Polyenergetic	75	10^9	Lead	Secondary TVLs
Attenuation	Polyenergetic	80	10^9	Lead	Secondary TVLs
Attenuation	Polyenergetic	85	10^9	Lead	Secondary TVLs
Attenuation	Polyenergetic	90	10^9	Lead	Secondary TVLs
Attenuation	Polyenergetic	95	10^9	Lead	Secondary TVLs
Attenuation	Polyenergetic	100	10^9	Lead	Secondary TVLs
Attenuation	Polyenergetic	10	10^9	Steel	Secondary TVLs
Attenuation	Polyenergetic	15	10^9	Steel	Secondary TVLs
Attenuation	Polyenergetic	20	10^9	Steel	Secondary TVLs
Attenuation	Polyenergetic	25	10^9	Steel	Secondary TVLs
Attenuation	Polyenergetic	30	10^9	Steel	Secondary TVLs
Attenuation	Polyenergetic	35	10^9	Steel	Secondary TVLs
Attenuation	Polyenergetic	40	10^9	Steel	Secondary TVLs
Attenuation	Polyenergetic	45	10^9	Steel	Secondary TVLs
Attenuation	Polyenergetic	50	10^9	Steel	Secondary TVLs
Attenuation	Polyenergetic	55	10^9	Steel	Secondary TVLs
Attenuation	Polyenergetic	60	10^9	Steel	Secondary TVLs
Attenuation	Polyenergetic	65	10^9	Steel	Secondary TVLs
Attenuation	Polyenergetic	70	10^9	Steel	Secondary TVLs
Attenuation	Polyenergetic	75	10^9	Steel	Secondary TVLs
Attenuation	Polyenergetic	80	10^9	Steel	Secondary TVLs
Attenuation	Polyenergetic	85	10^9	Steel	Secondary TVLs
Attenuation	Polyenergetic	90	10^9	Steel	Secondary TVLs
Attenuation	Polyenergetic	95	10^9	Steel	Secondary TVLs
Attenuation	Polyenergetic	100	10^9	Steel	Secondary TVLs

Appendix B. Polar Plots of Scatter Fractions for Simulated Primary Beam Energies

This Appendix contains the polar plots of the scatter fractions created for each simulated primary beam energy. All possible scatter directions are shown as polar plots representing the front half (left), i.e., with 0° (center of plot) defined as the direction of the incident beam, or back half (right) of the sphere. White radial lines mark azimuthal angles of the scattering geometry, while concentric circles correspond to polar angles. The plots match at their outer edges, corresponding to a 90° scatter angle. The color scale represents scatter intensity. Note the polar plots found in this Appendix have different ranges for their corresponding color scales.

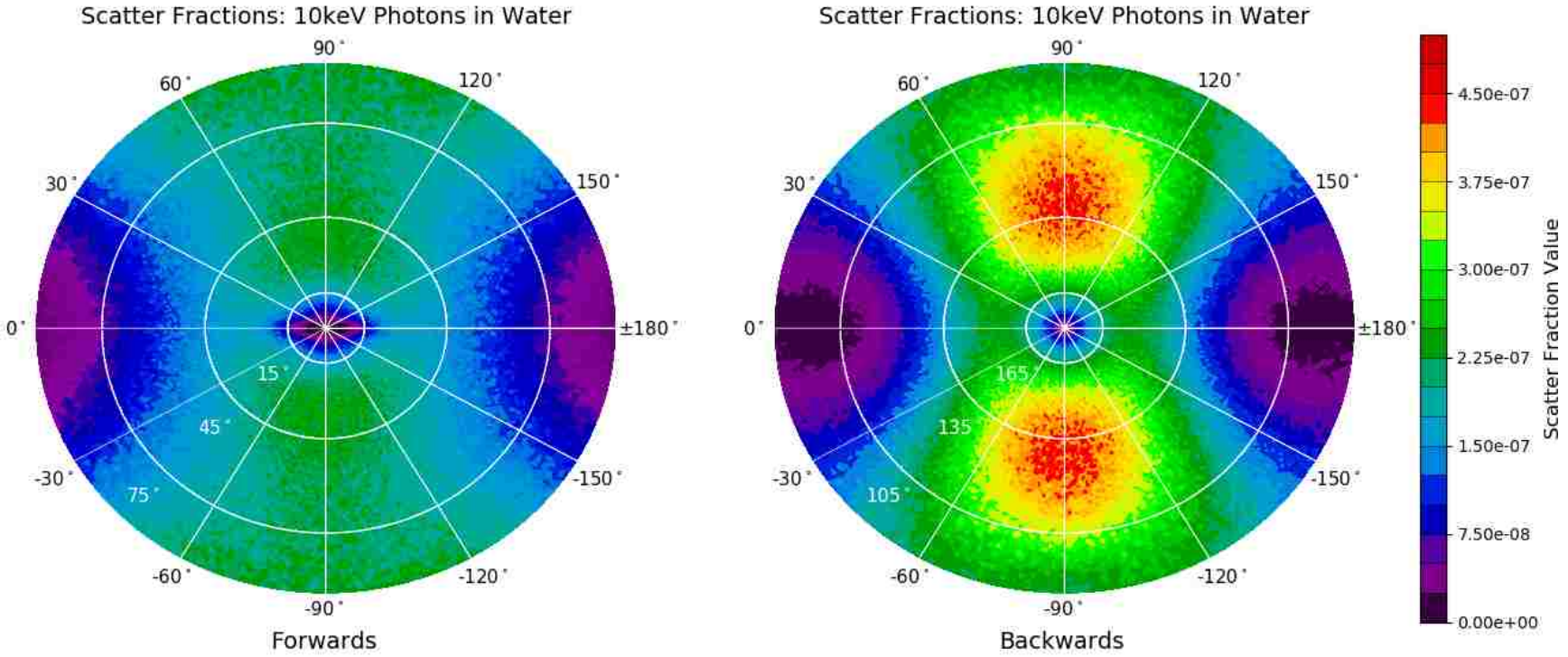

Figure B.1. Scatter fractions for a 100x2-mm^2 beam of 10 keV polarized photons scattering from a 2-cm x 6-cm radius cylinder of water.

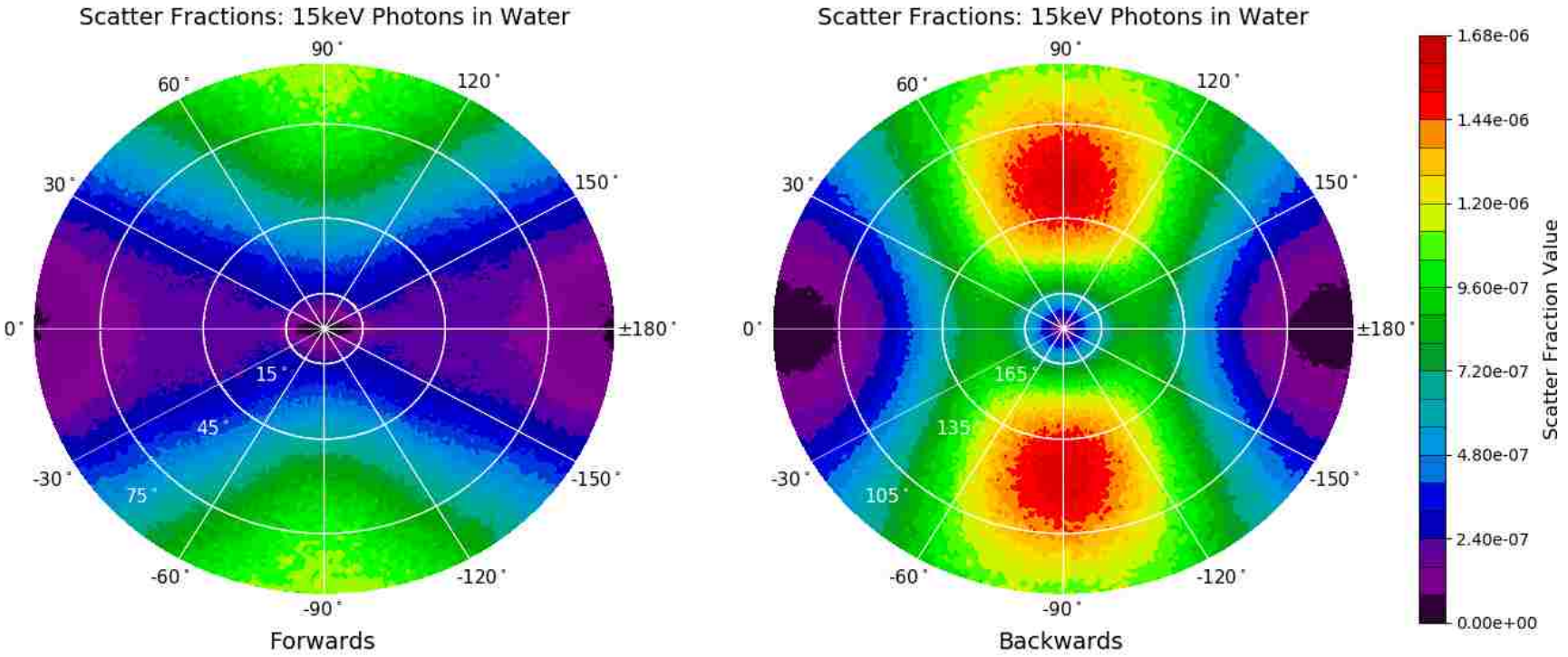

Figure B.2. Scatter fractions for a 100x2-mm^2 beam of 15 keV polarized photons scattering from a 2-cm x 6-cm radius cylinder of water.

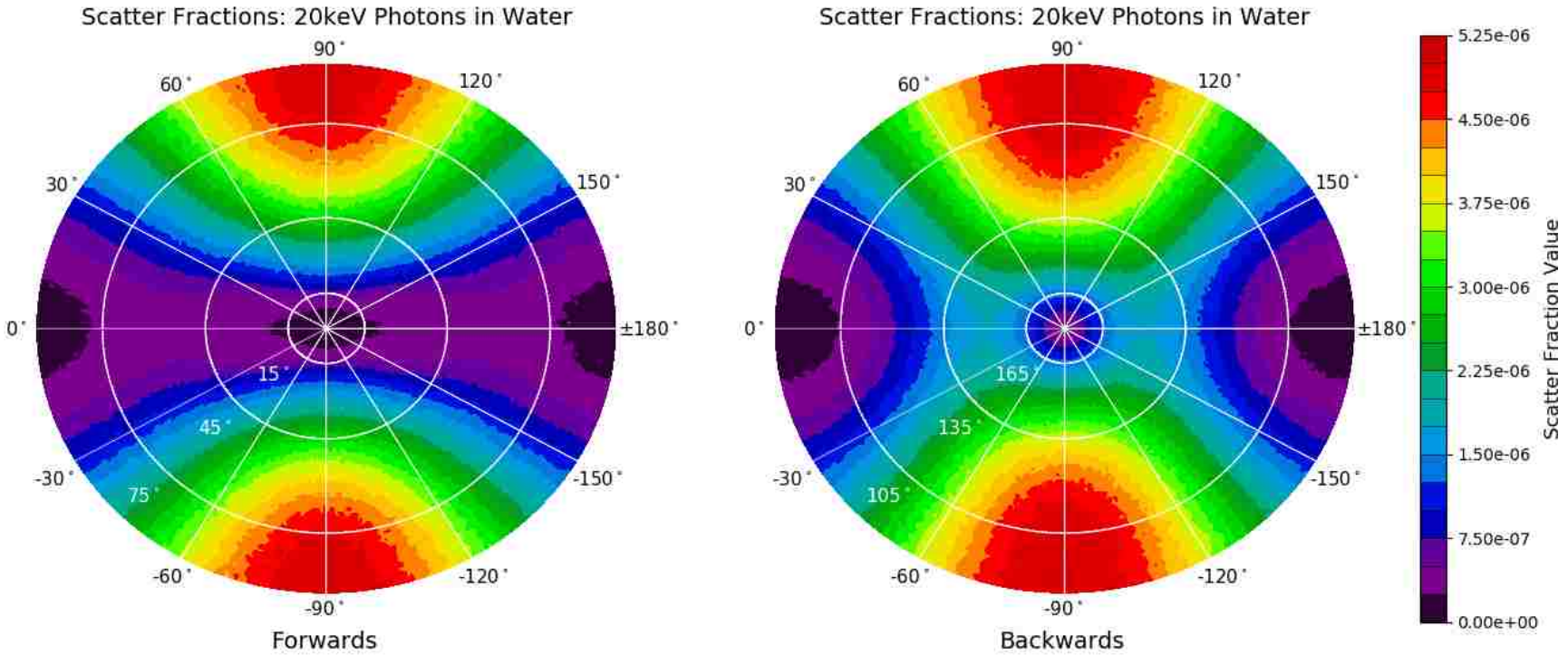

Figure B.3. Scatter fractions for a 100x2-mm^2 beam of 20 keV polarized photons scattering from a 2-cm x 6-cm radius cylinder of water.

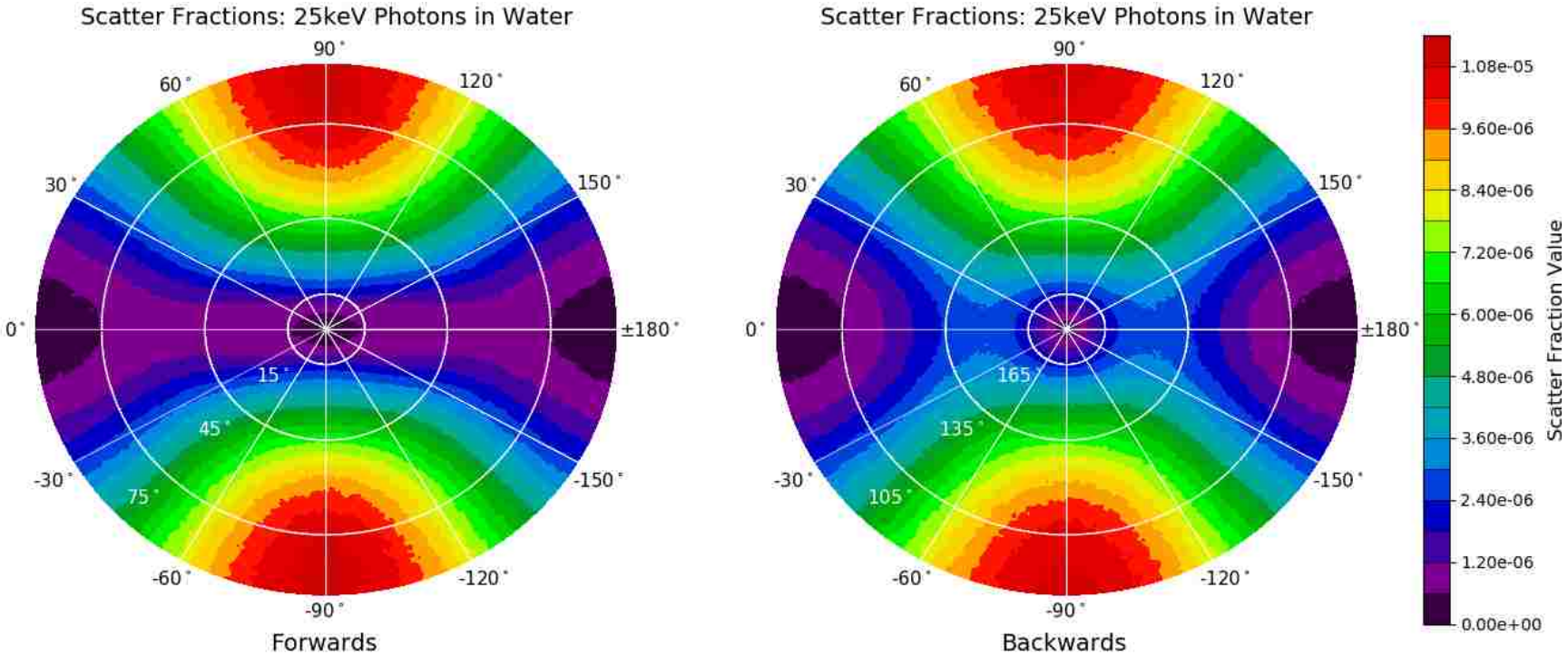

Figure B.4. Scatter fractions for a 100x2-mm^2 beam of 25 keV polarized photons scattering from a 2-cm x 6-cm radius cylinder of water.

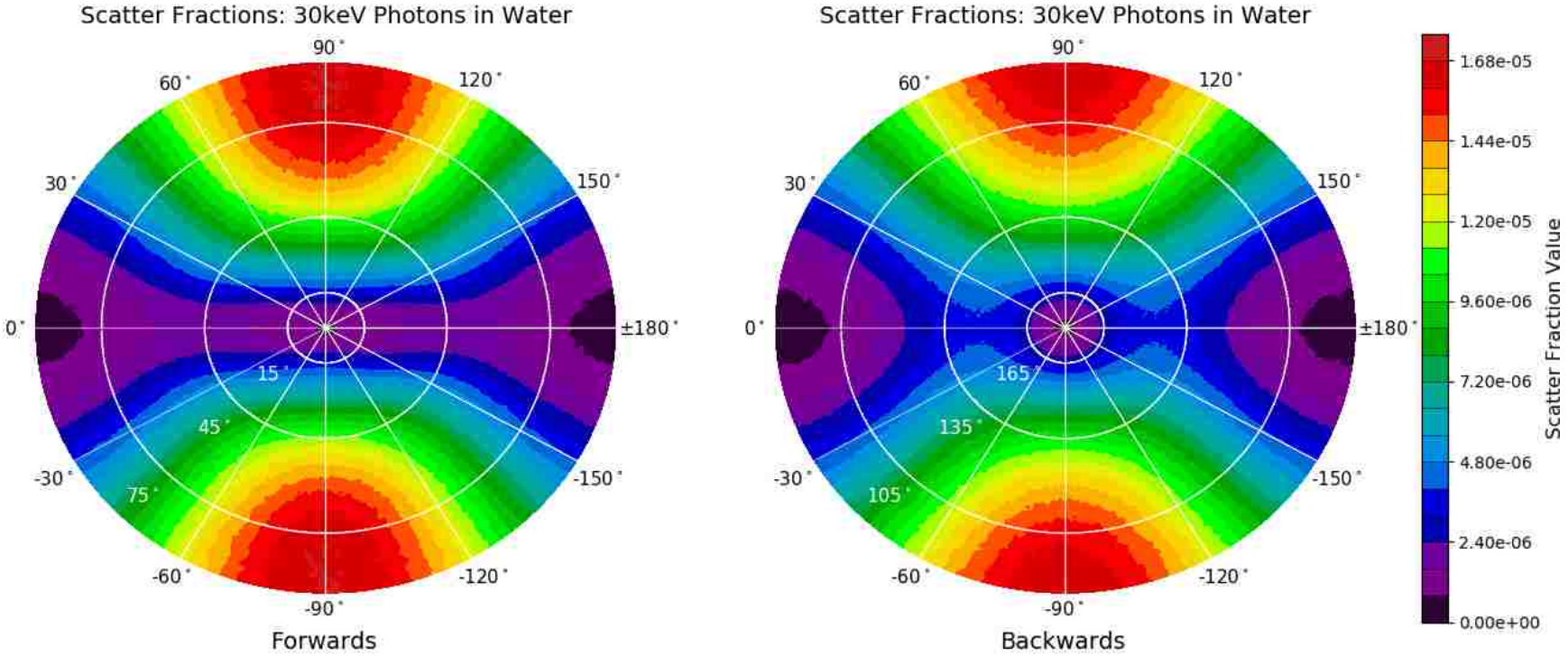

Figure B.5. Scatter fractions for a 100x2-mm^2 beam of 30 keV polarized photons scattering from a 2-cm x 6-cm radius cylinder of water.

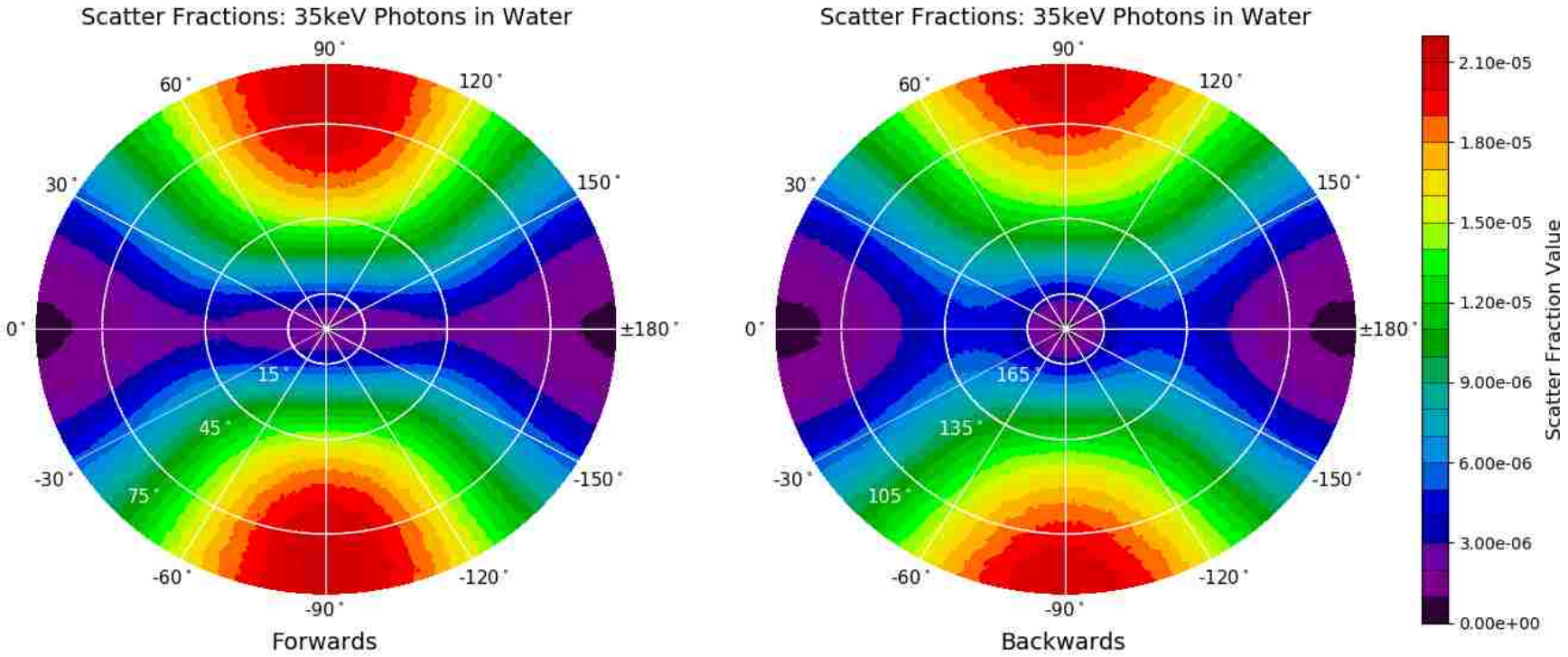

Figure B.6. Scatter fractions for a 100x2-mm^2 beam of 35 keV polarized photons scattering from a 2-cm x 6-cm radius cylinder of water.

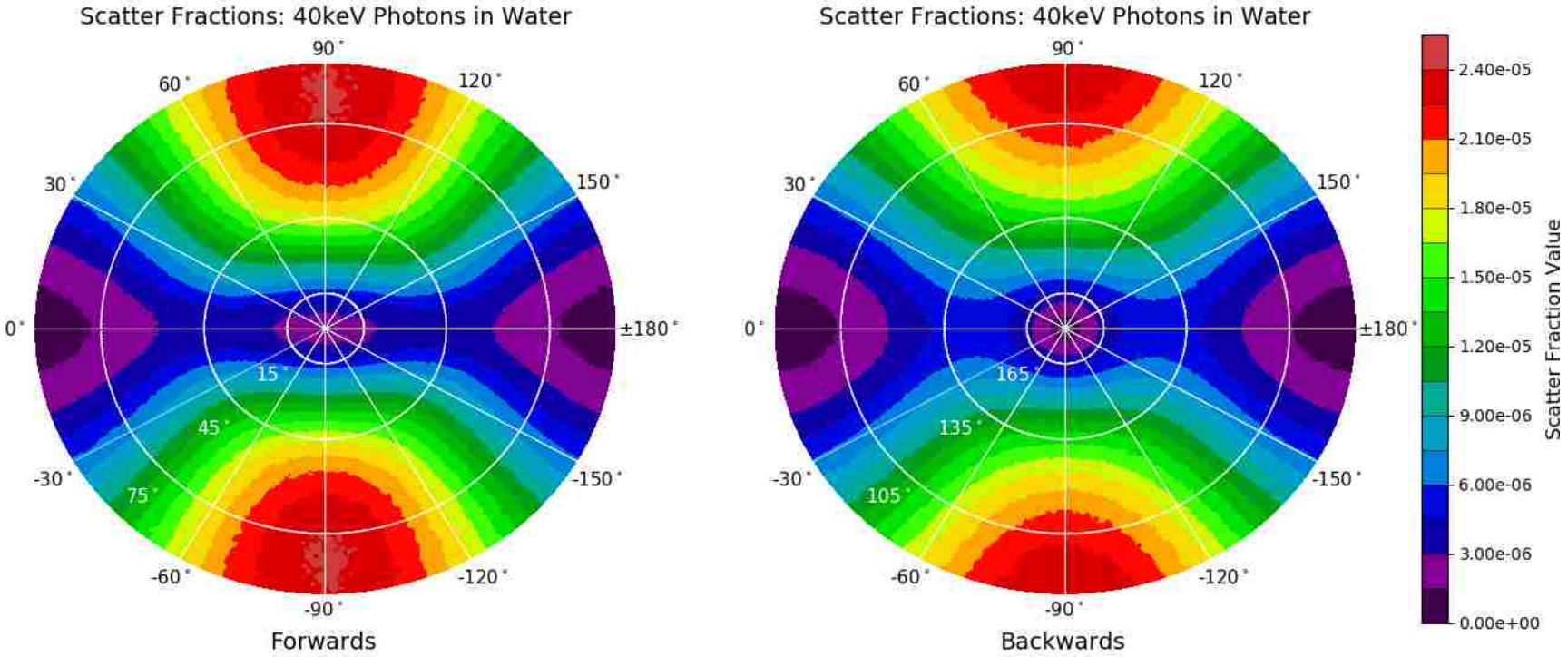

Figure B.7. Scatter fractions for a 100x2-mm^2 beam of 40 keV polarized photons scattering from a 2-cm x 6-cm radius cylinder of water.

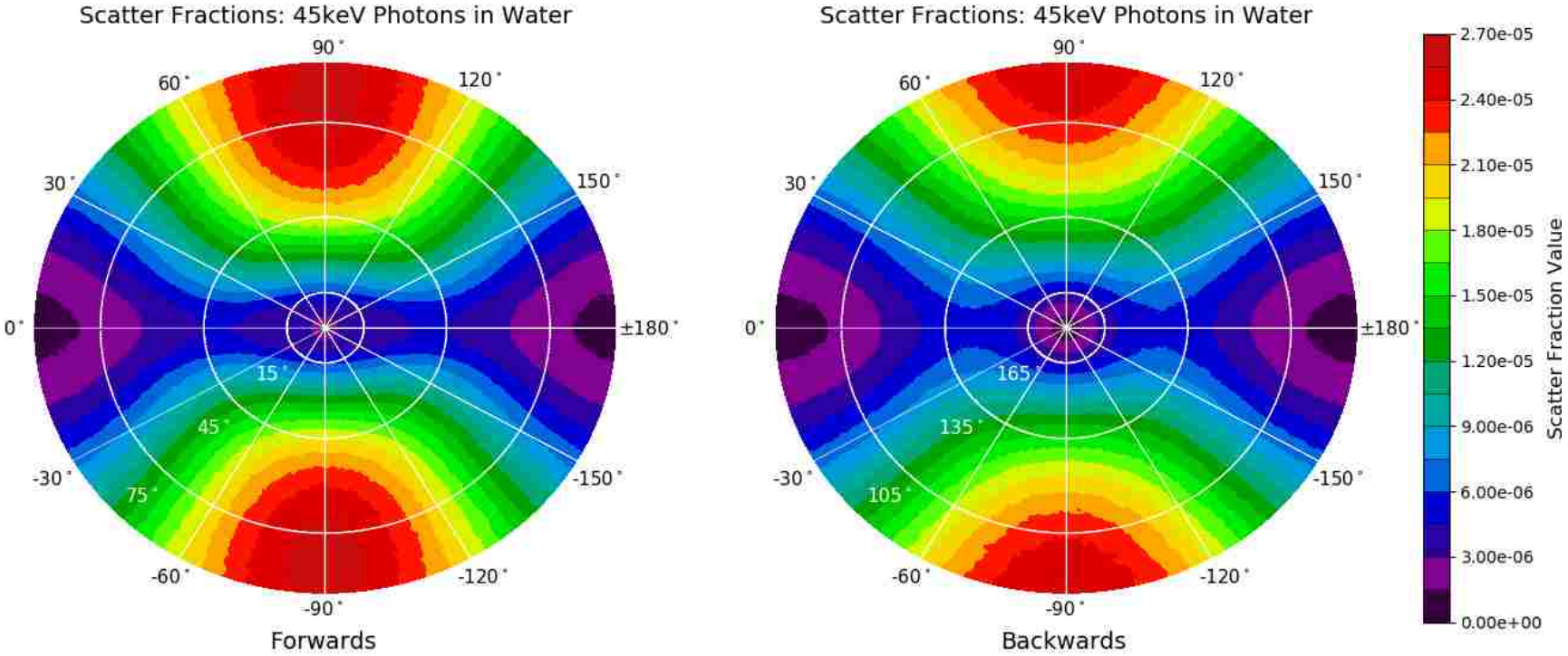

Figure B.8. Scatter fractions for a 100x2-mm^2 beam of 45 keV polarized photons scattering from a 2-cm x 6-cm radius cylinder of water.

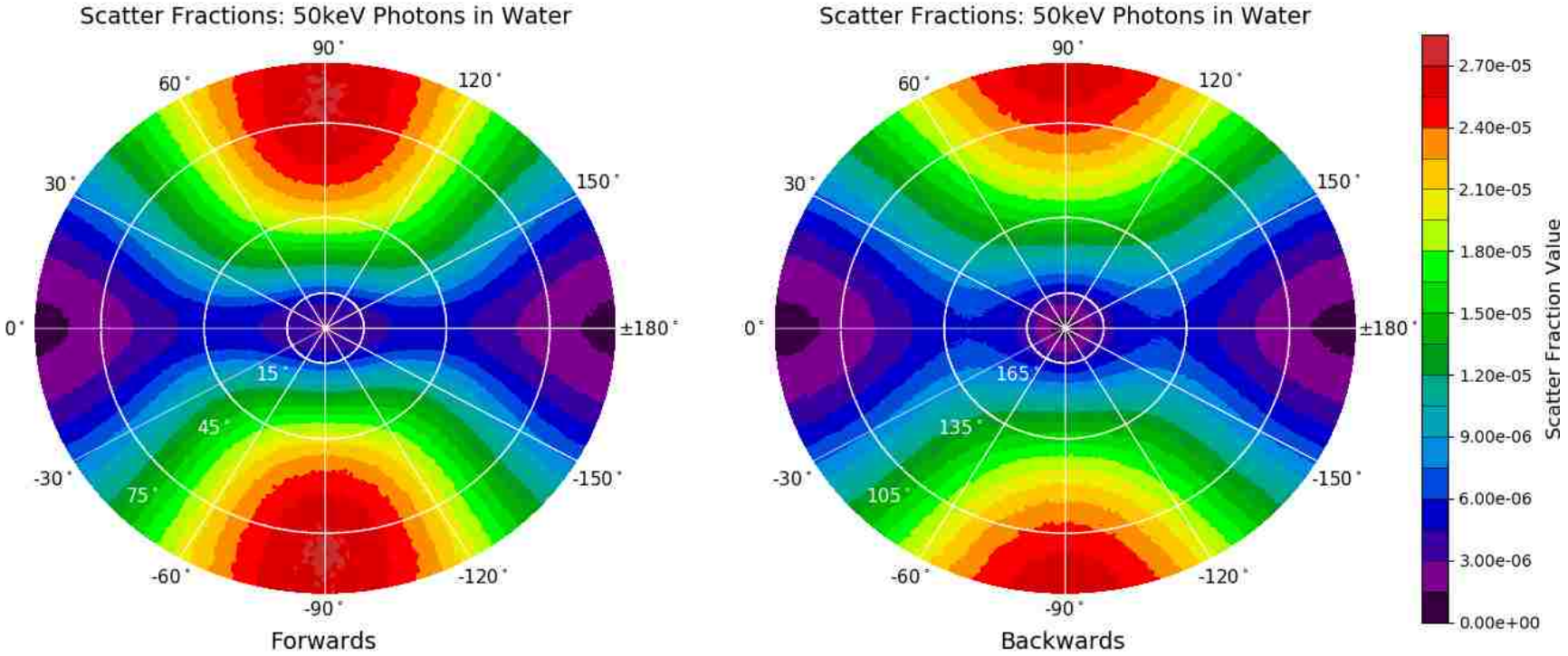

Figure B.9. Scatter fractions for a 100x2-mm^2 beam of 50 keV polarized photons scattering from a 2-cm x 6-cm radius cylinder of water.

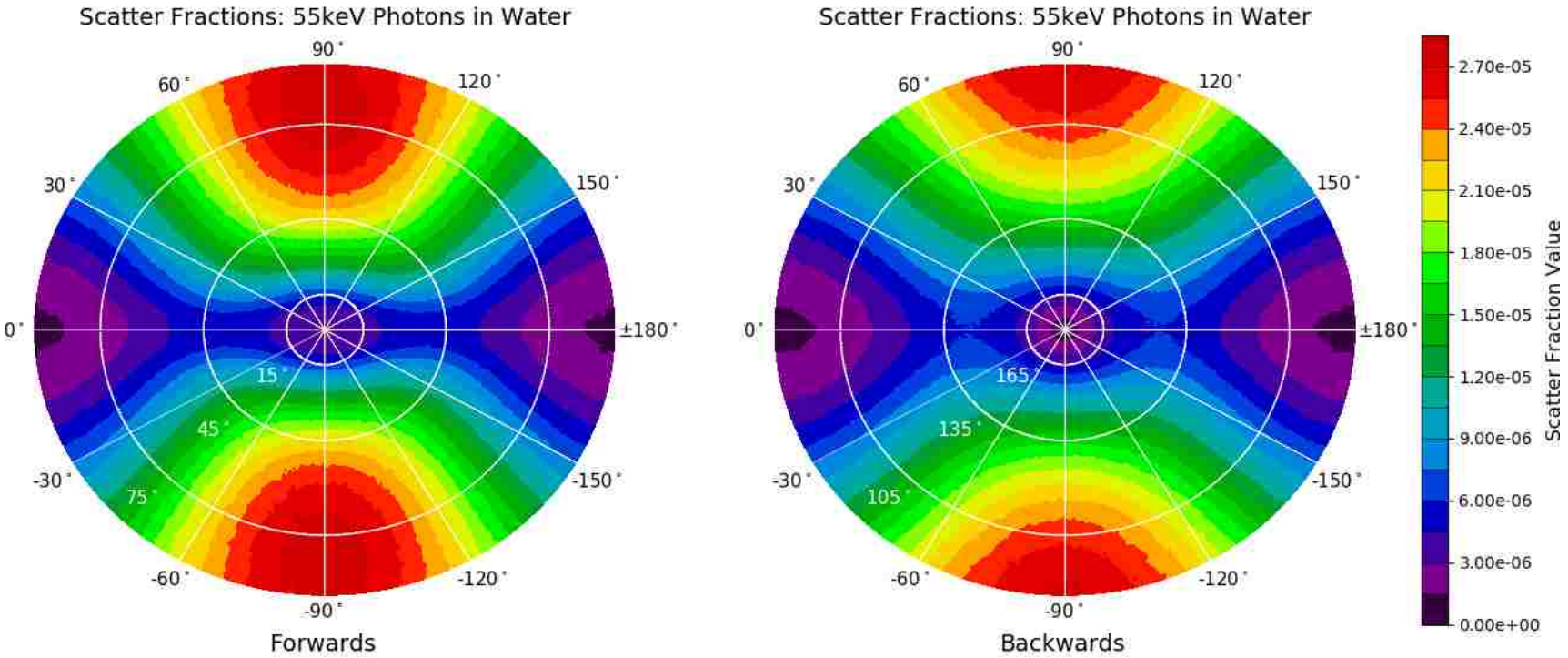

Figure B.10. Scatter fractions for a 100x2-mm^2 beam of 55 keV polarized photons scattering from a 2-cm x 6-cm radius cylinder of water.

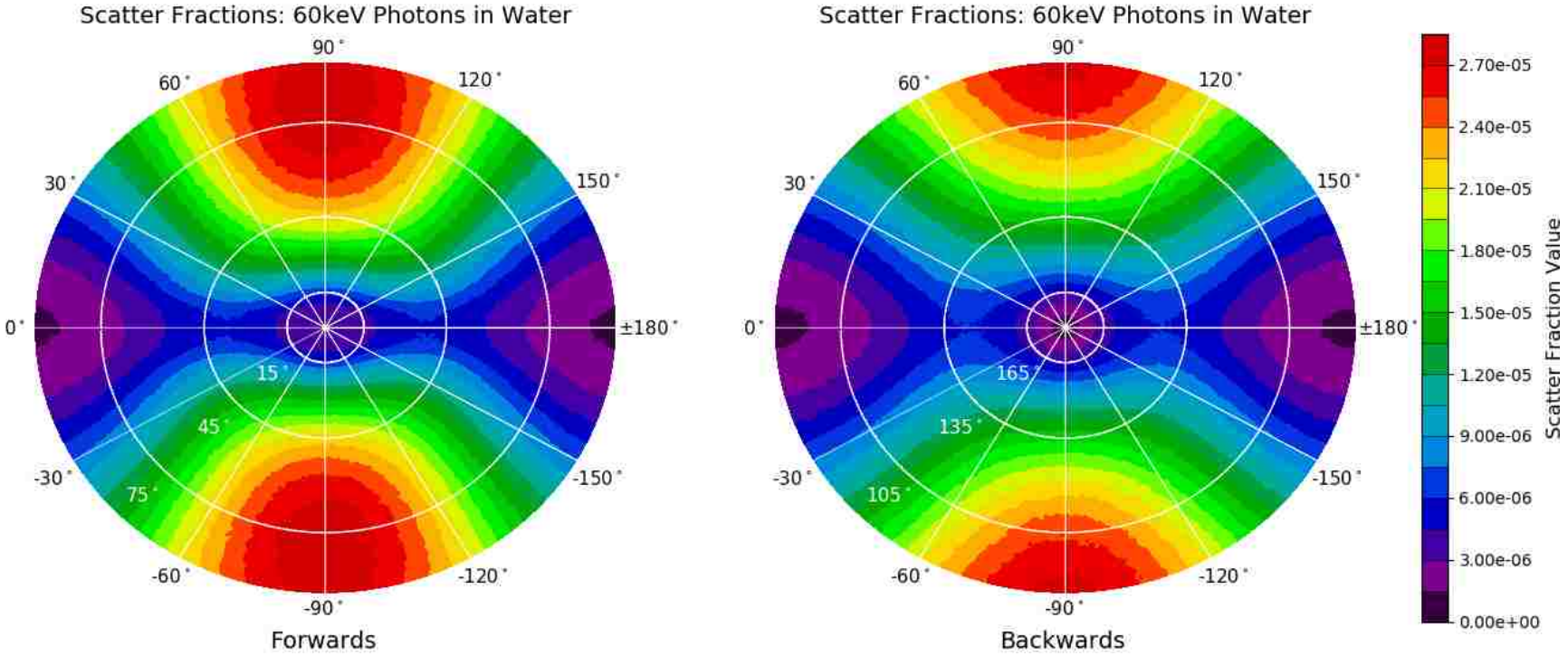

Figure B.11. Scatter fractions for a 100x2-mm^2 beam of 60 keV polarized photons scattering from a 2-cm x 6-cm radius cylinder of water.

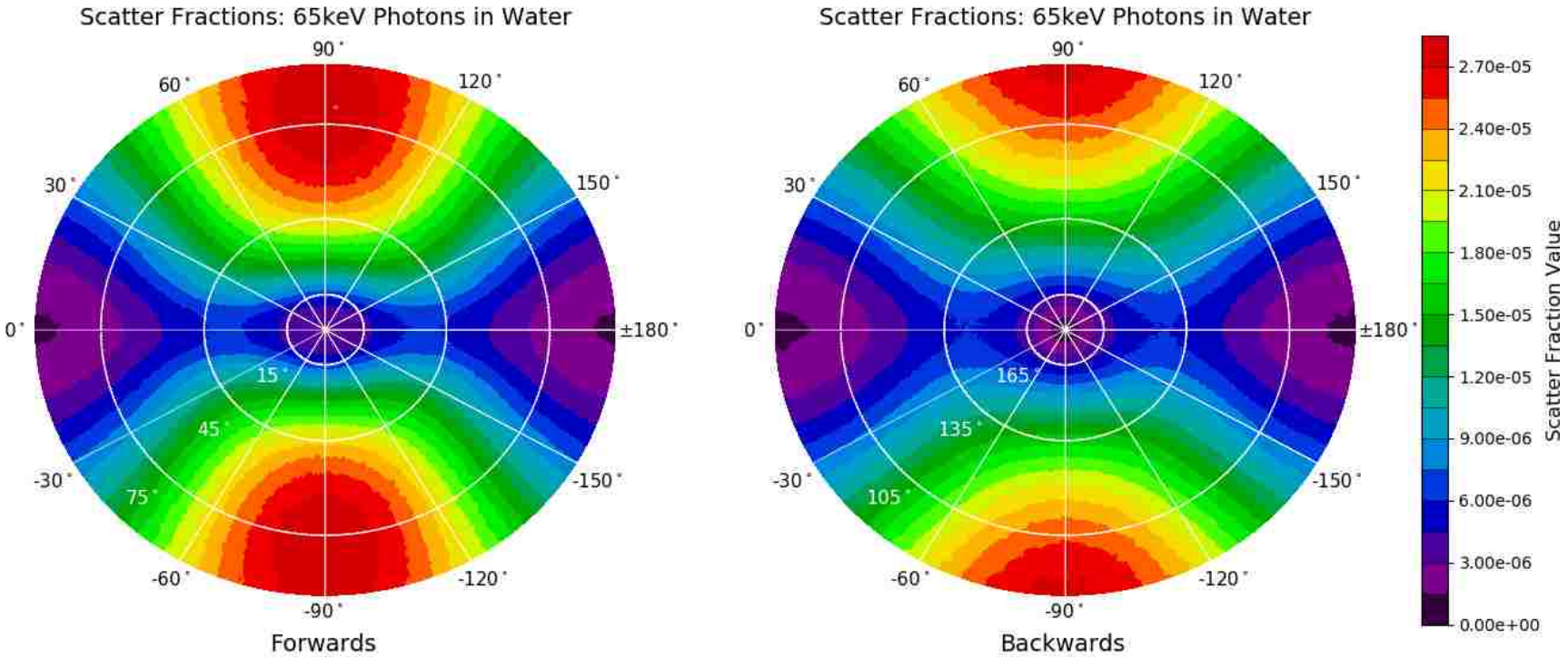

Figure B.12. Scatter fractions for a 100x2-mm^2 beam of 65 keV polarized photons scattering from a 2-cm x 6-cm radius cylinder of water.

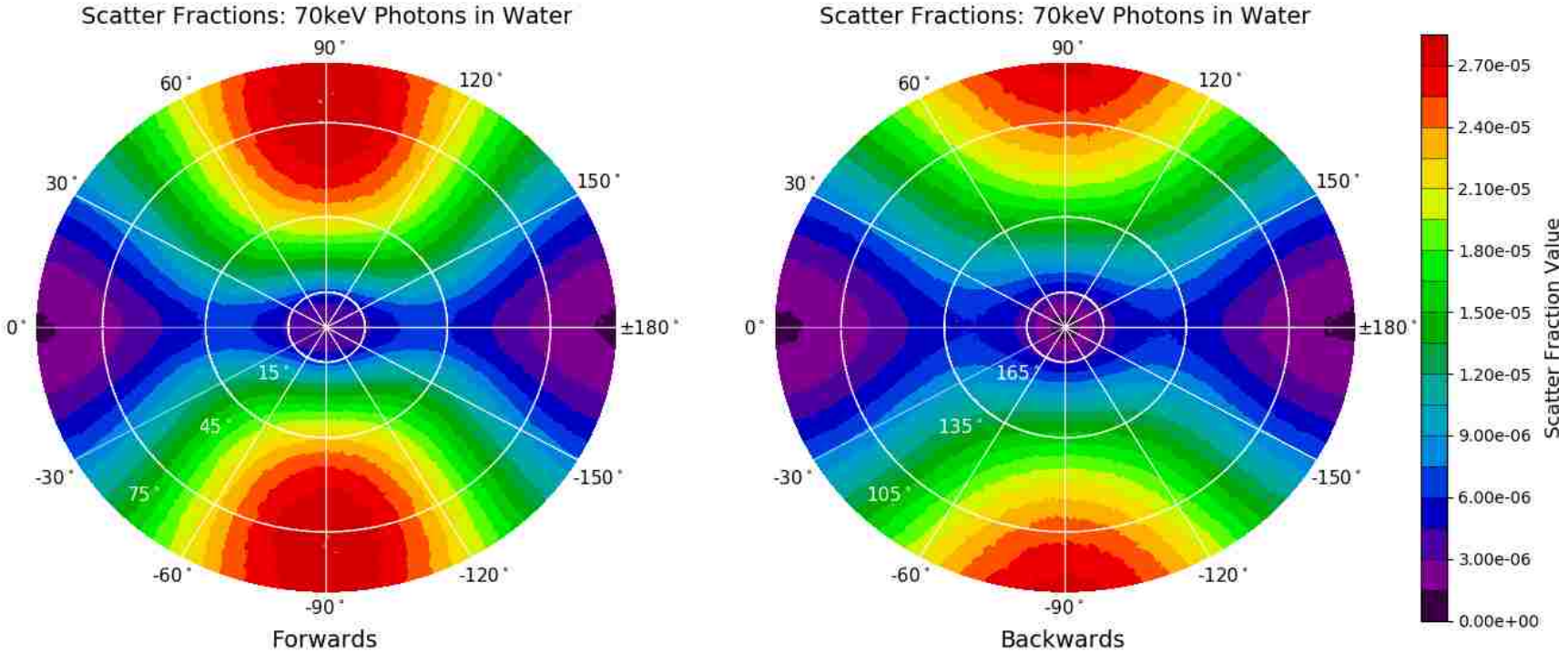

Figure B.13. Scatter fractions for a 100x2-mm^2 beam of 70 keV polarized photons scattering from a 2-cm x 6-cm radius cylinder of water.

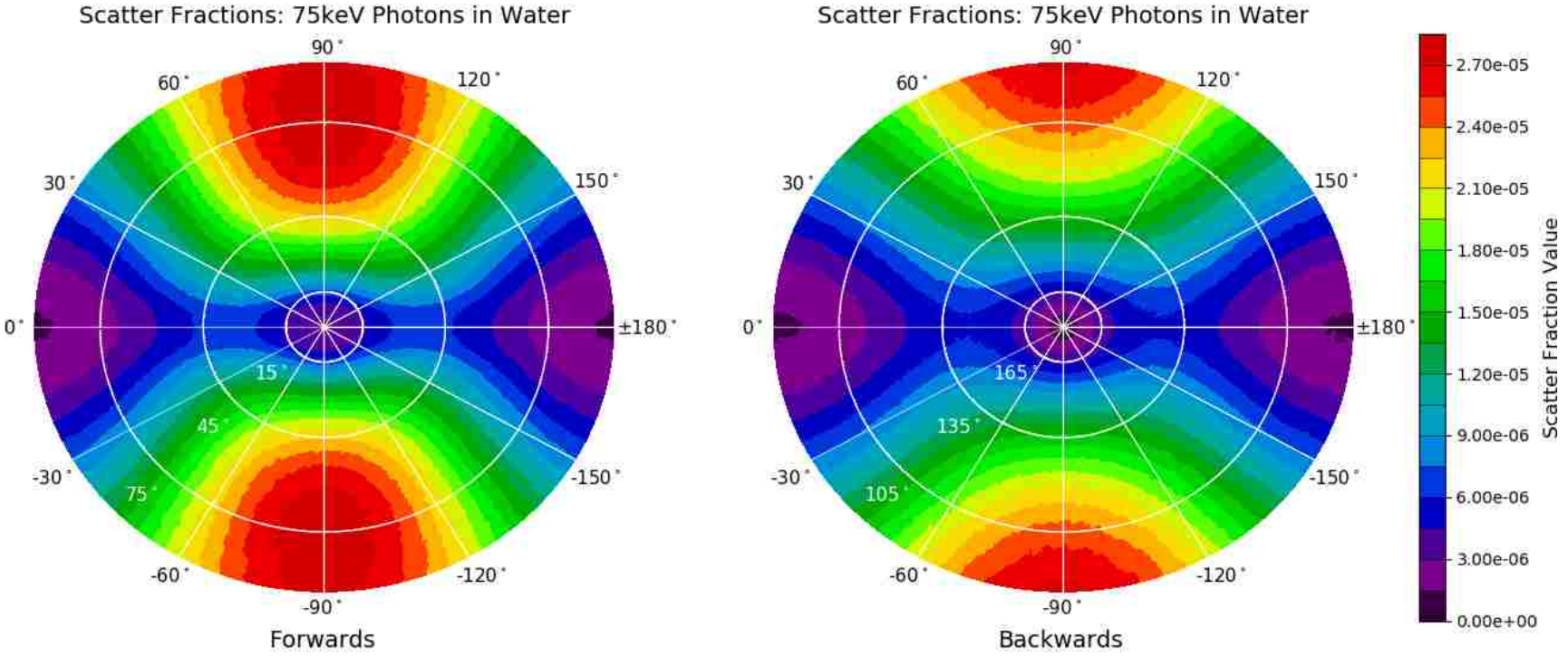

Figure B.14. Scatter fractions for a 100x2-mm^2 beam of 75 keV polarized photons scattering from a 2-cm x 6-cm radius cylinder of water.

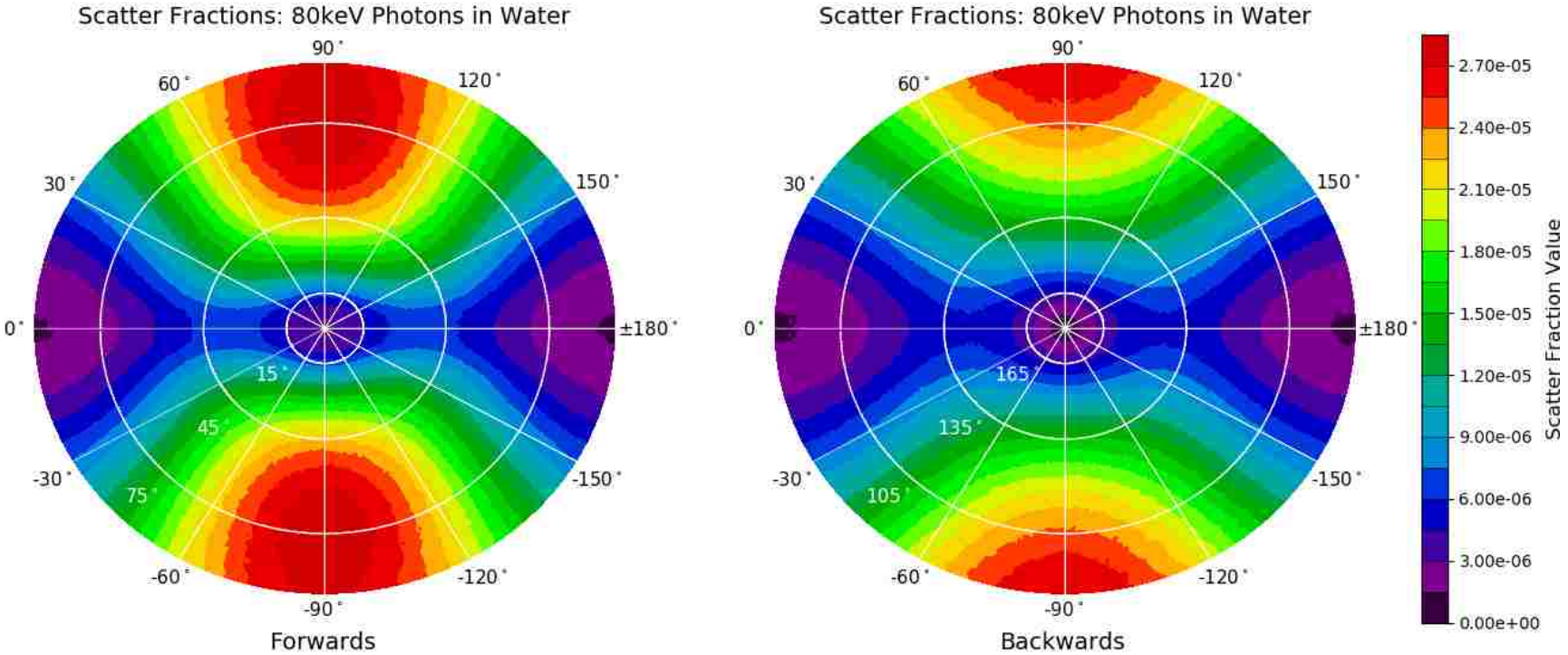

Figure B.15. Scatter fractions for a 100x2-mm^2 beam of 80 keV polarized photons scattering from a 2-cm x 6-cm radius cylinder of water.

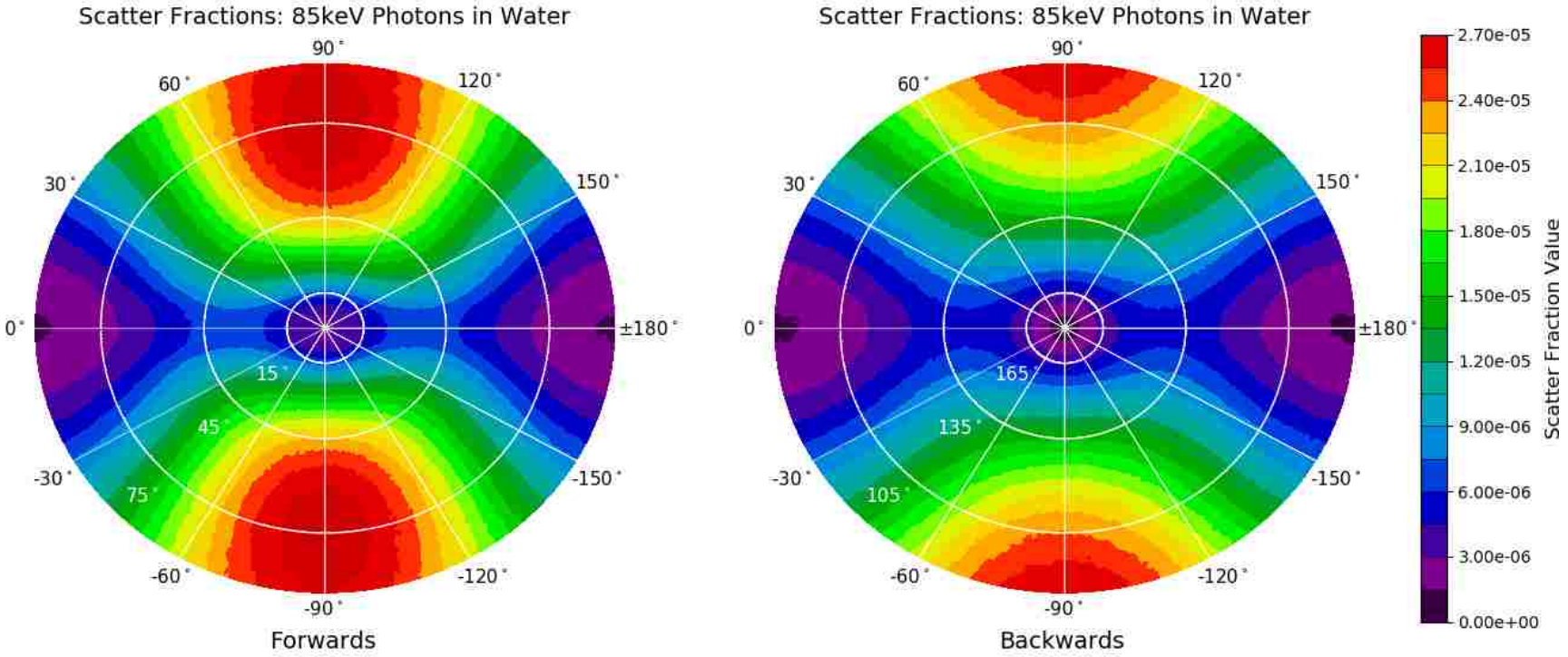

Figure B.16. Scatter fractions for a 100x2-mm^2 beam of 85 keV polarized photons scattering from a 2-cm x 6-cm radius cylinder of water.

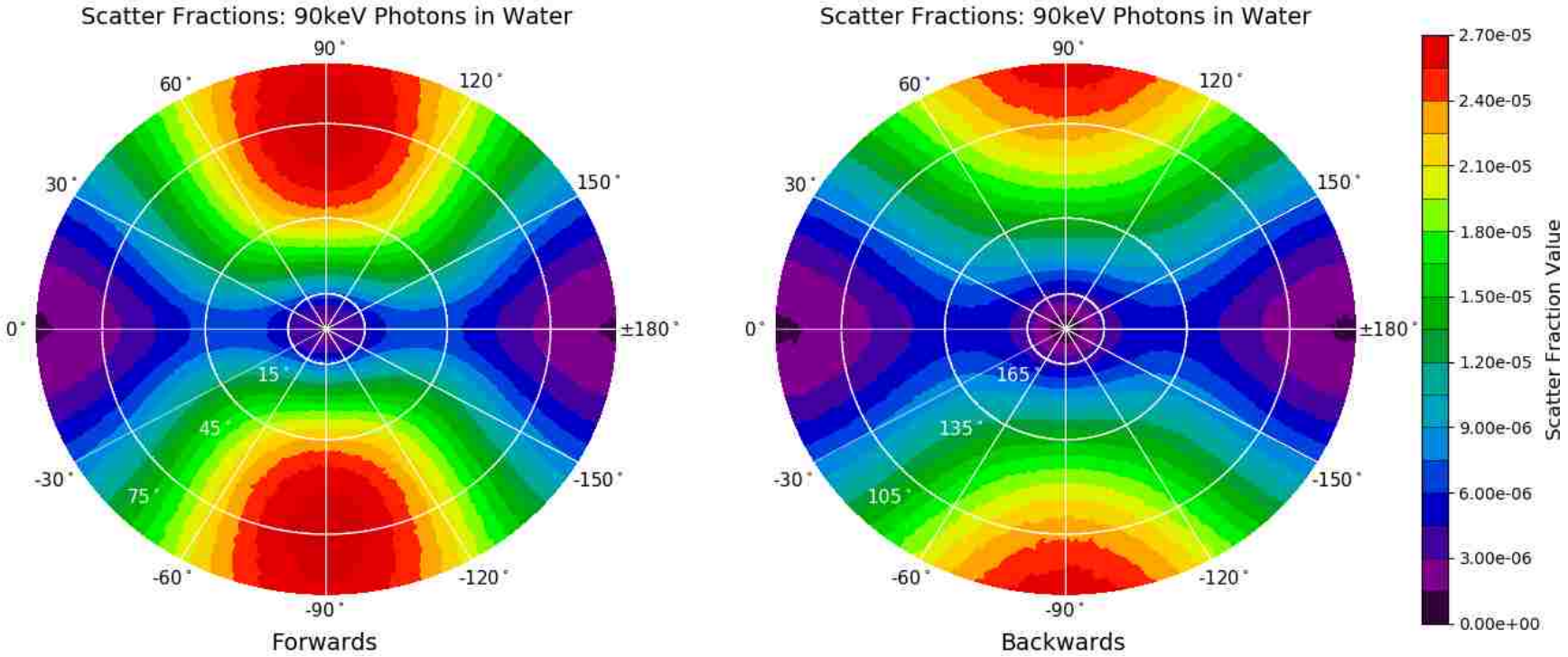

Figure B.17. Scatter fractions for a 100x2-mm^2 beam of 90 keV polarized photons scattering from a 2-cm x 6-cm radius cylinder of water.

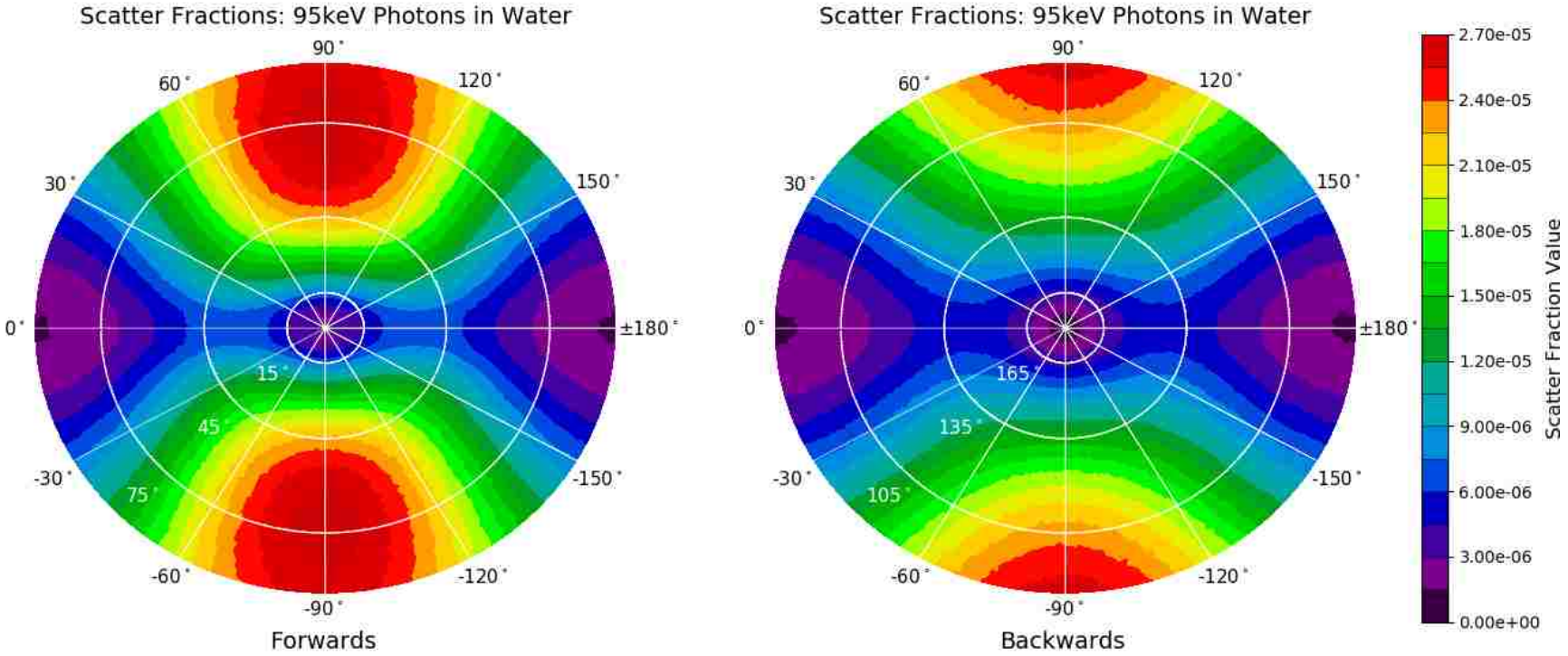

Figure B.18. Scatter fractions for a 100x2-mm^2 beam of 95 keV polarized photons scattering from a 2-cm x 6-cm radius cylinder of water.

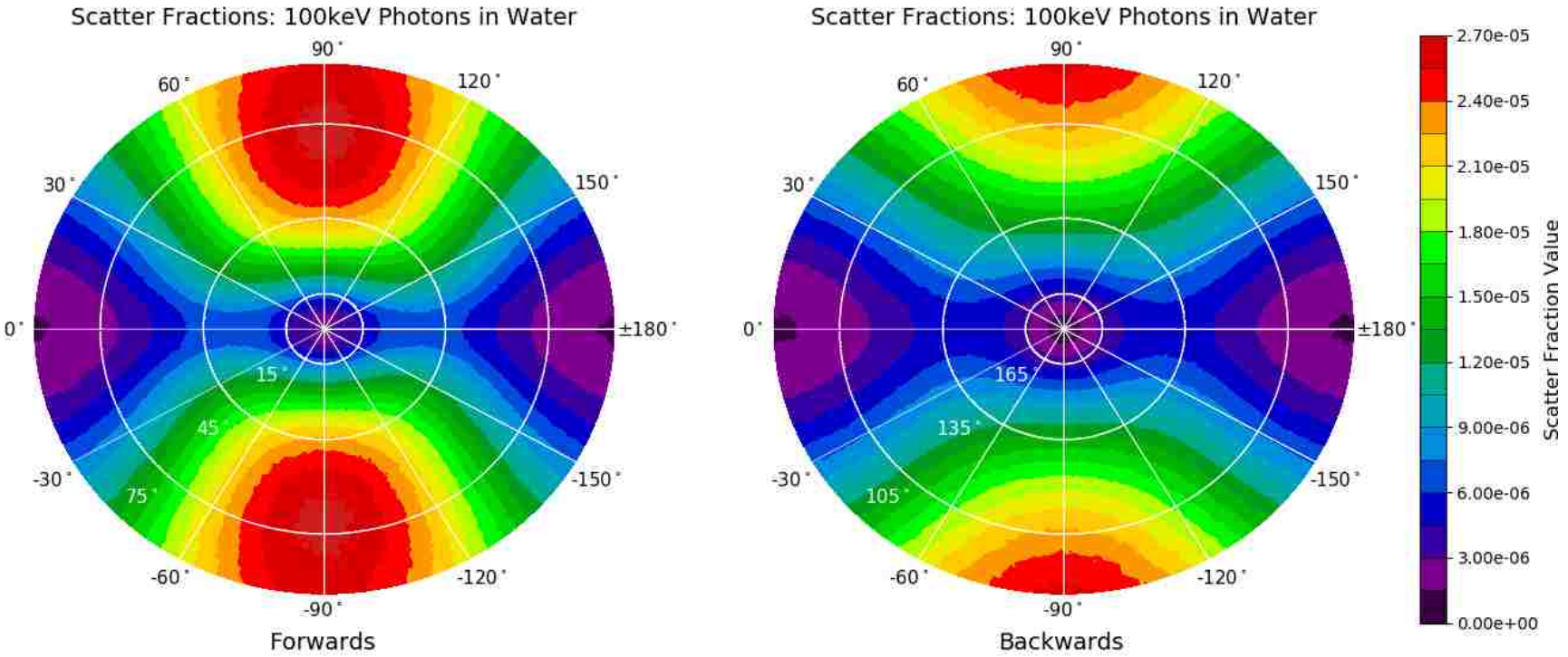

Figure B.19. Scatter fractions for a 100x2-mm^2 beam of 100 keV polarized photons scattering from a 2-cm x 6-cm radius cylinder of water.

Appendix C. Polar Plots of Albedos for NIST Concrete, Lead, and NIST Steel

This Appendix contains the polar plots of the albedos for monoenergetic primary beams incident on a block of material. Each polar plot represents a hemisphere encompassing the possible directions of reflection of x-rays from the barrier. White radial lines correspond to azimuthal angles of the scattering geometry, while concentric circles correspond to polar angles. The center of each plot is the normal to the barrier and the outer edge represents 90° reflection parallel to the barrier's surface. The color scale represents albedo intensity. Note the polar plots found in this Appendix have different ranges for their corresponding color scales.

C.1. NIST Defined Concrete Albedo Polar Plots

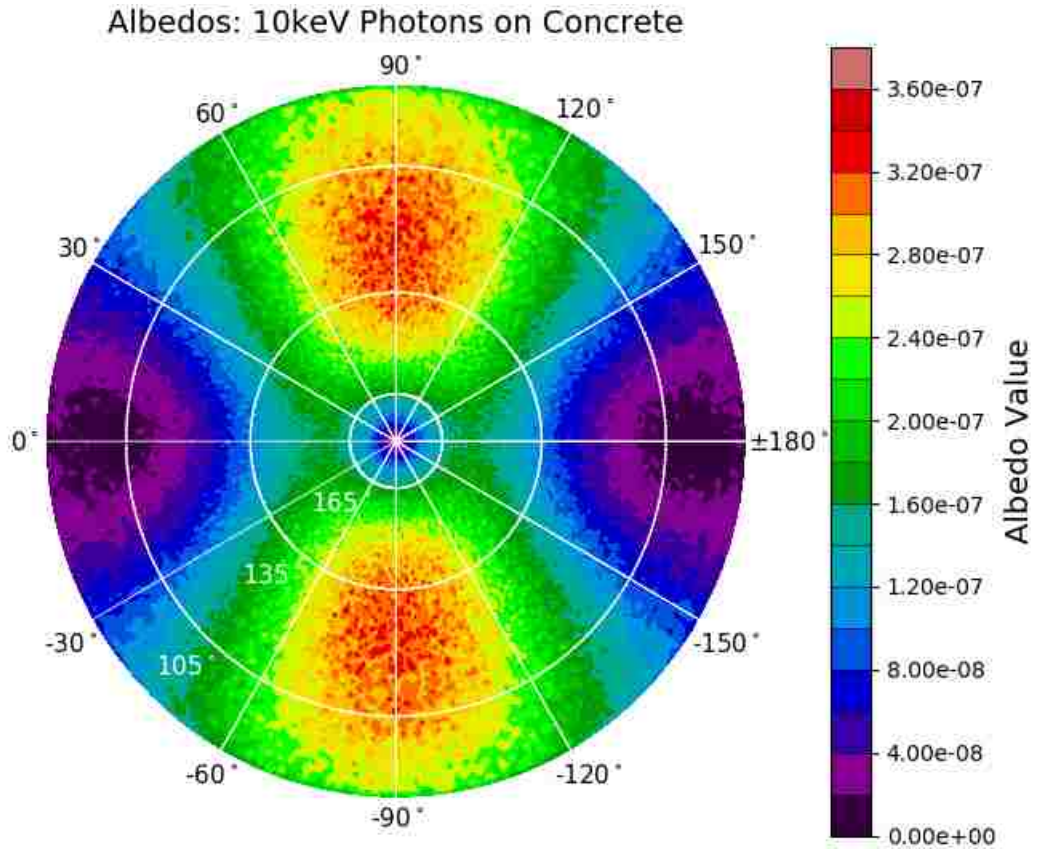

Figure C.1. Albedos for a beam of 10 keV polarized x-rays incident on a slab of concrete.

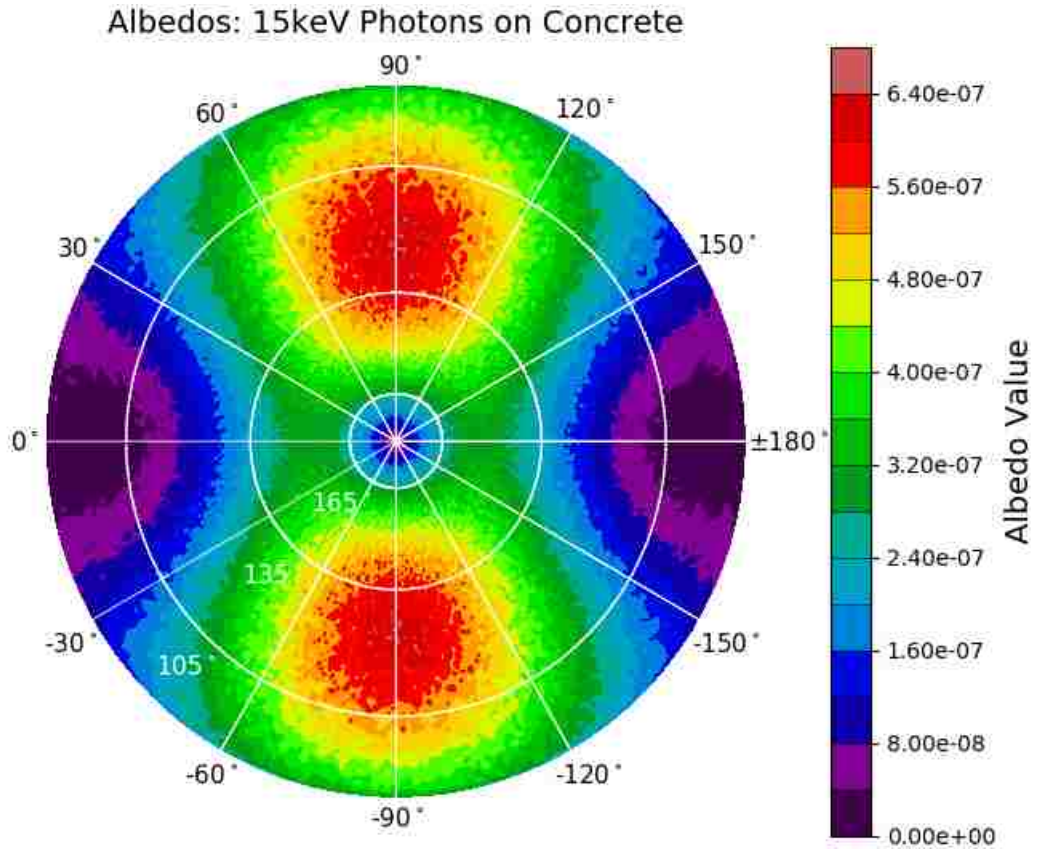

Figure C.2. Albedos for a beam of 15 keV polarized x-rays incident on a slab of concrete.

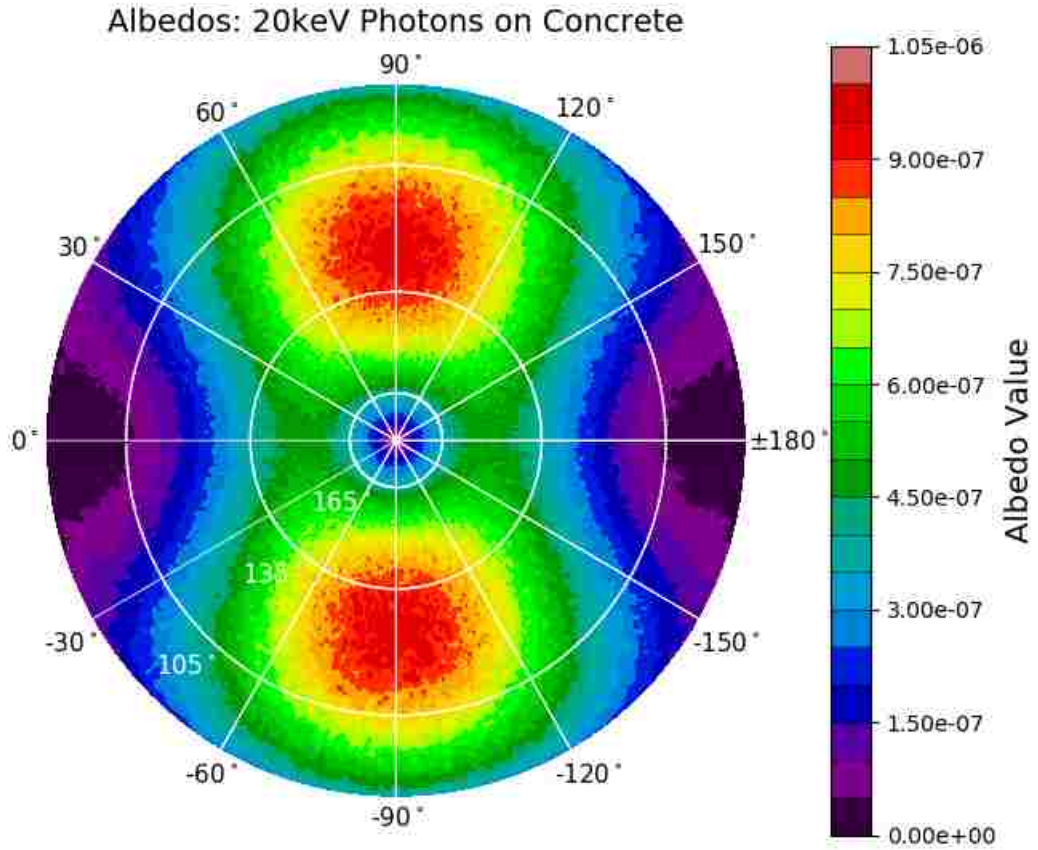

Figure C.3. Albedos for a beam of 20 keV polarized x-rays incident on a slab of concrete.

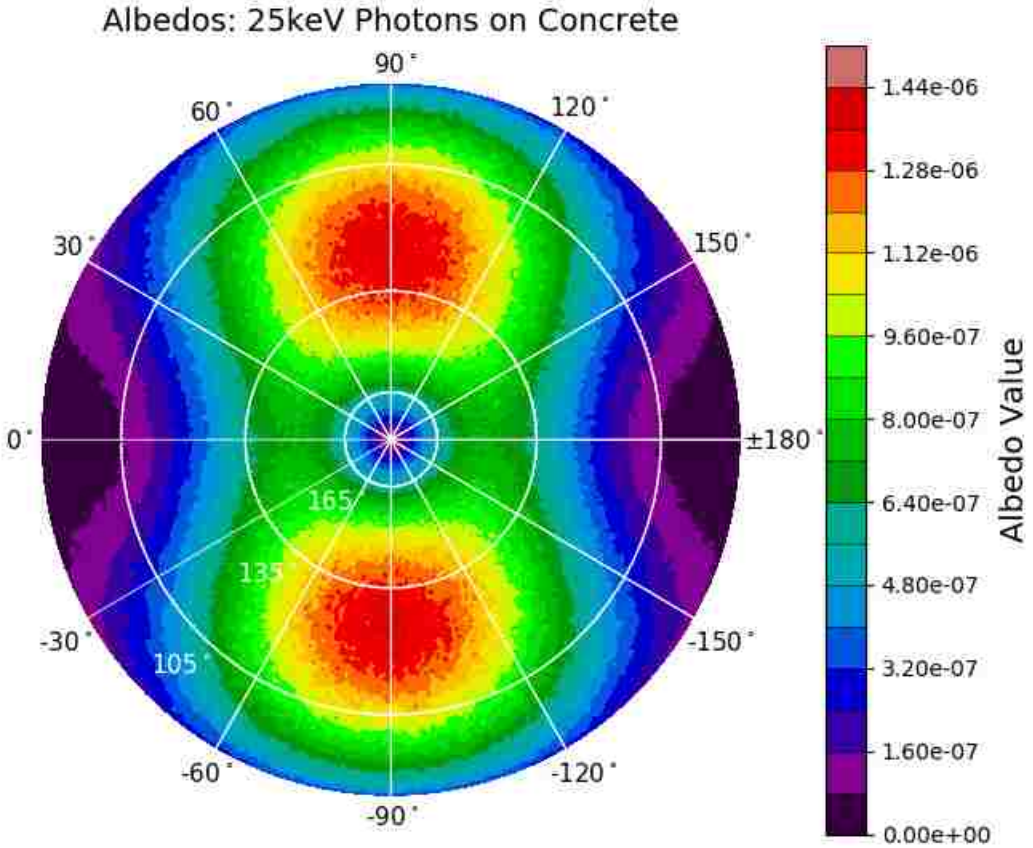

Figure C.4. Albedos for a beam of 25 keV polarized x-rays incident on a slab of concrete.

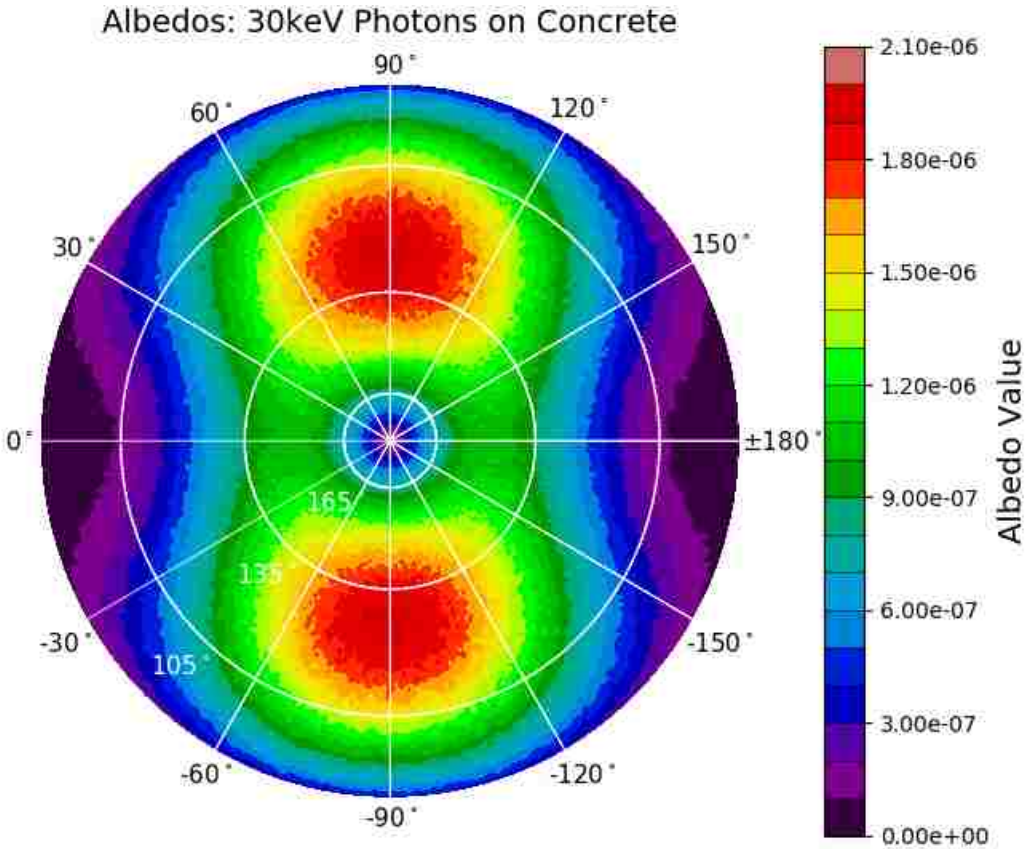

Figure C.5. Albedos for a beam of 30 keV polarized x-rays incident on a slab of concrete.

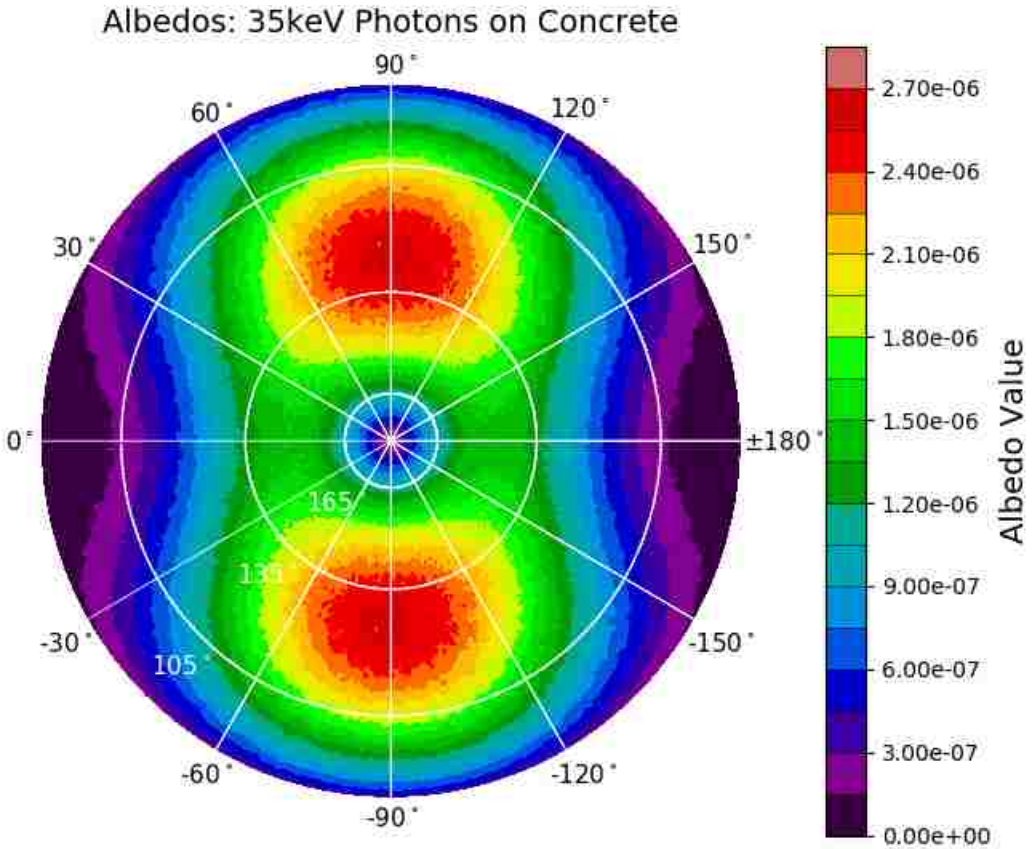

Figure C.6. Albedos for a beam of 35 keV polarized x-rays incident on a slab of concrete.

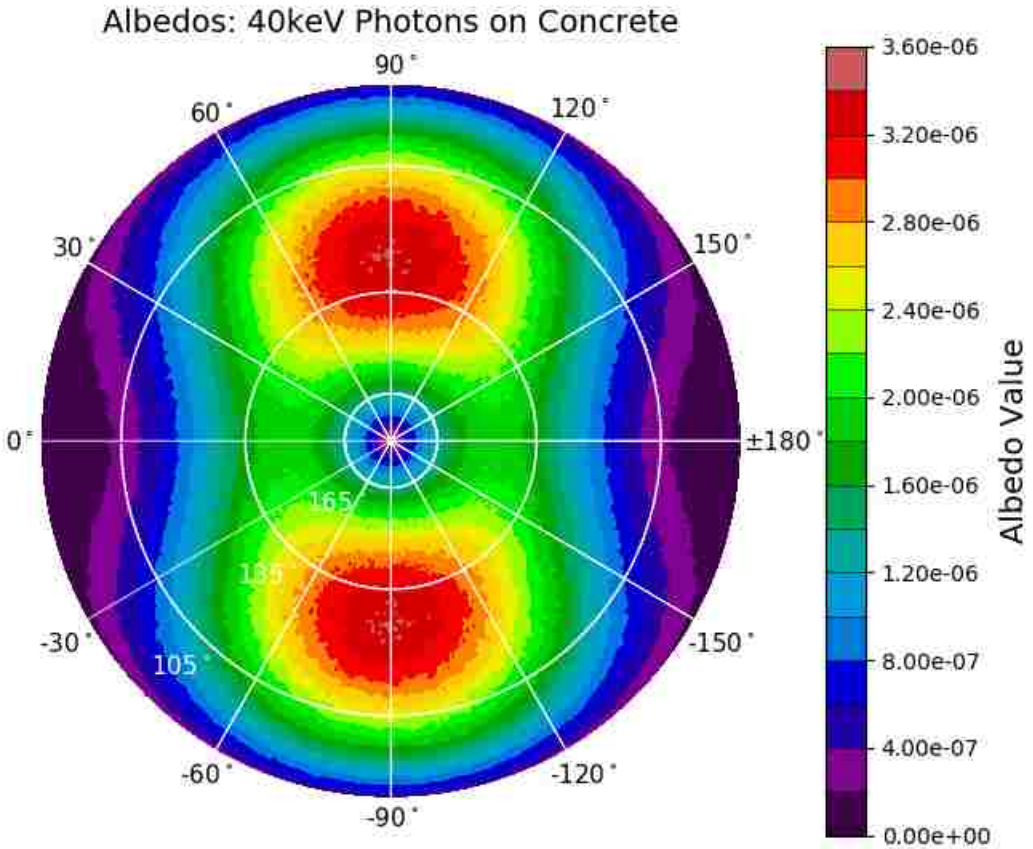

Figure C.7. Albedos for a beam of 40 keV polarized x-rays incident on a slab of concrete.

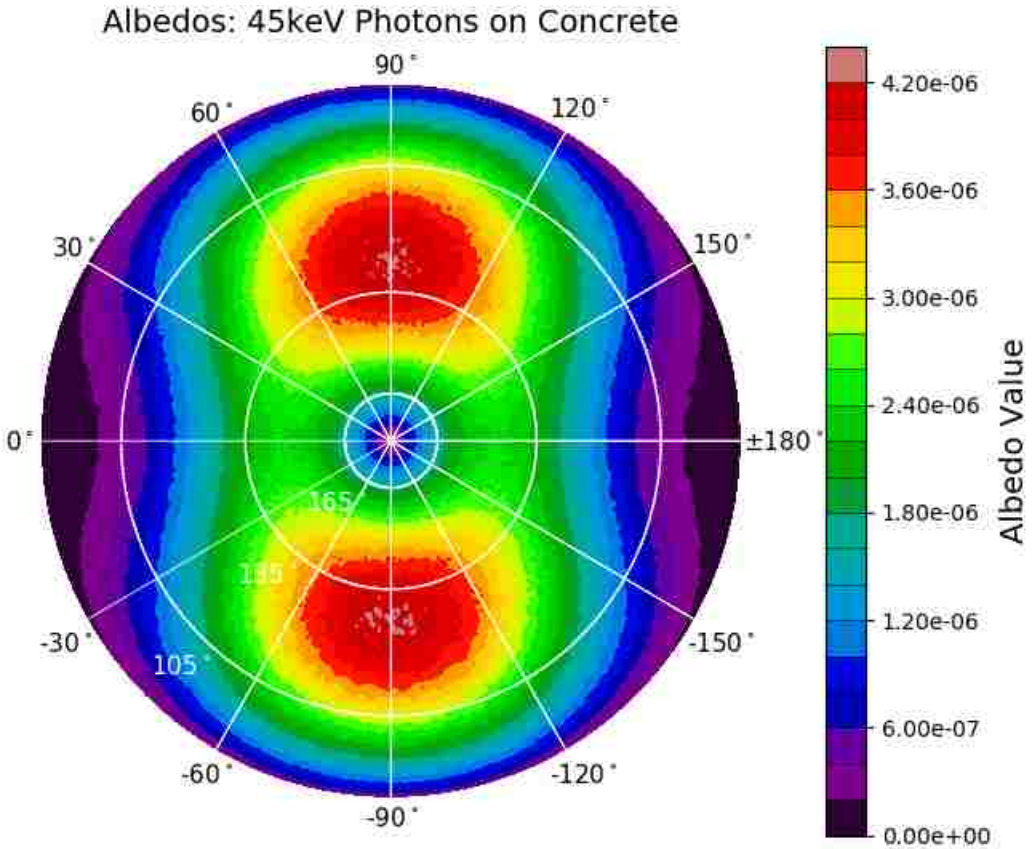

Figure C.8. Albedos for a beam of 45 keV polarized x-rays incident on a slab of concrete.

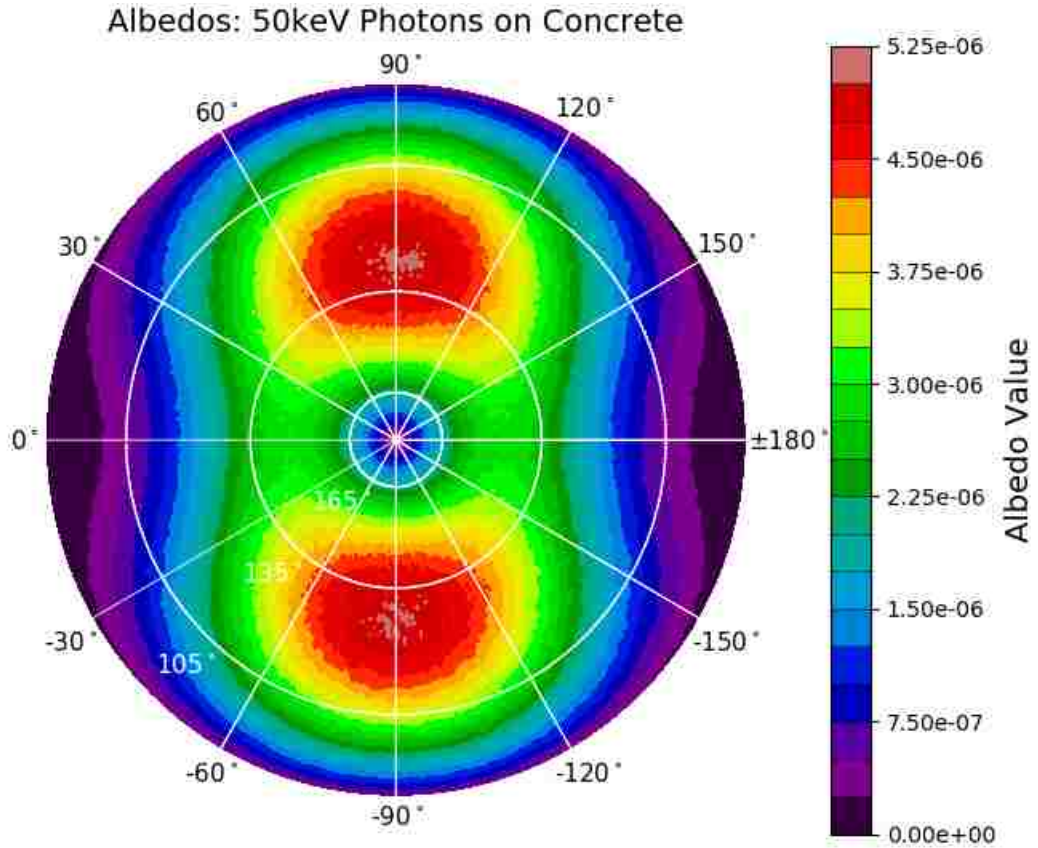

Figure C.9. Albedos for a beam of 50 keV polarized x-rays incident on a slab of concrete.

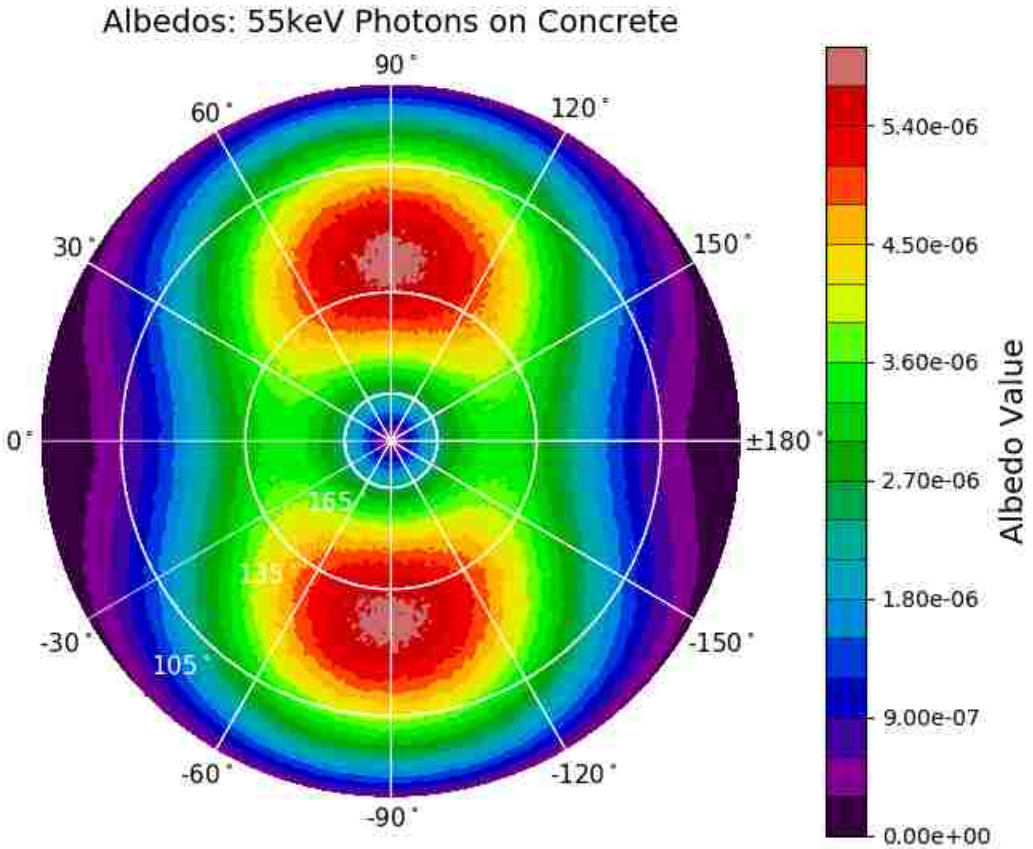

Figure C.10. Albedos for a beam of 55 keV polarized x-rays incident on a slab of concrete.

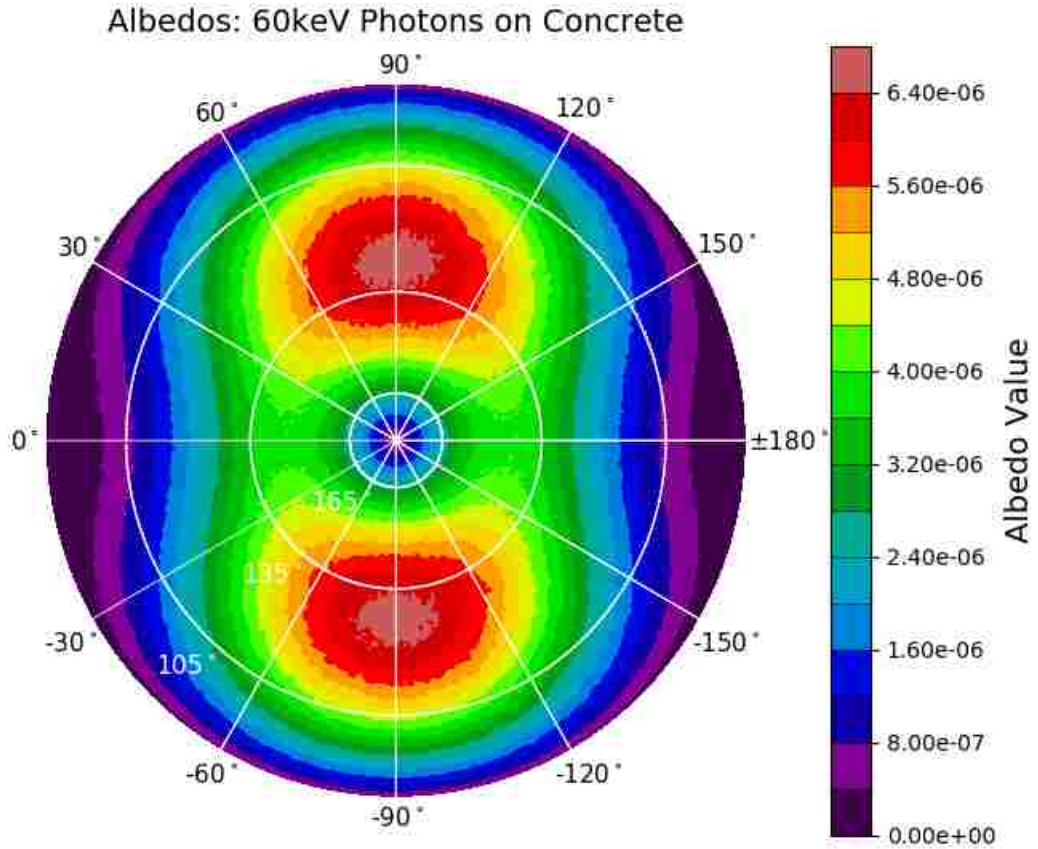

Figure C.11. Albedos for a beam of 60 keV polarized x-rays incident on a slab of concrete.

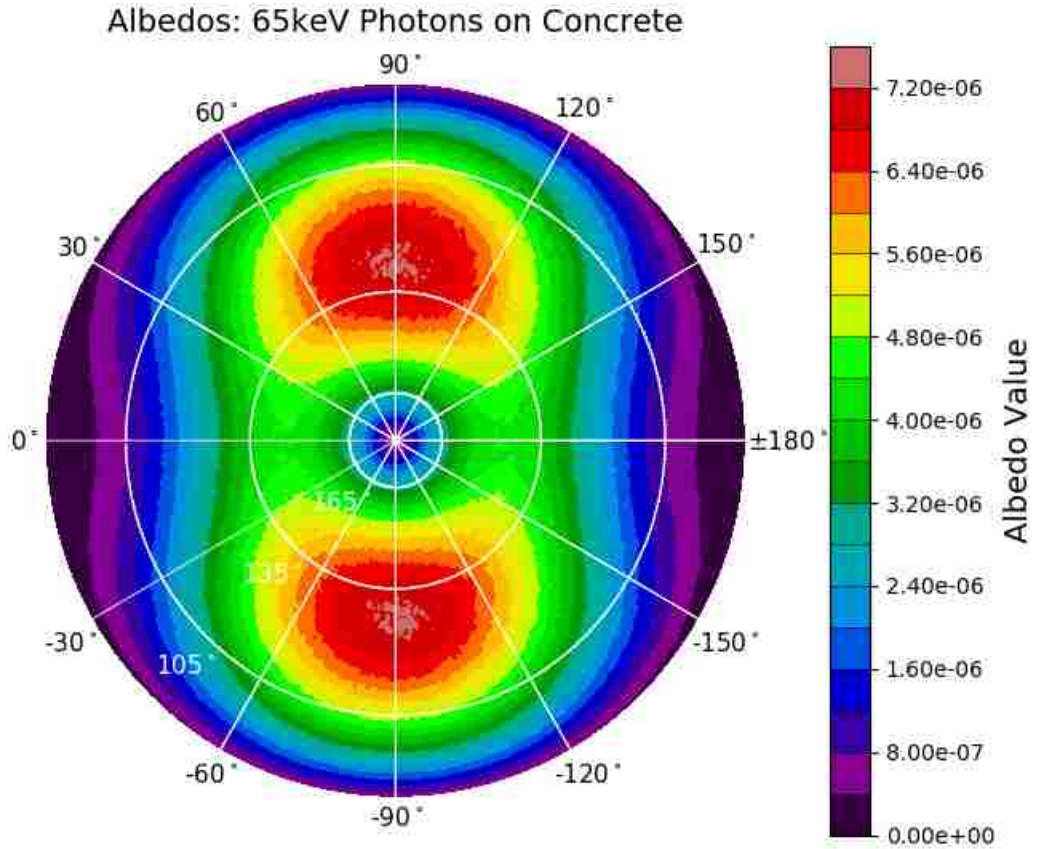

Figure C.12. Albedos for a beam of 65 keV polarized x-rays incident on a slab of concrete.

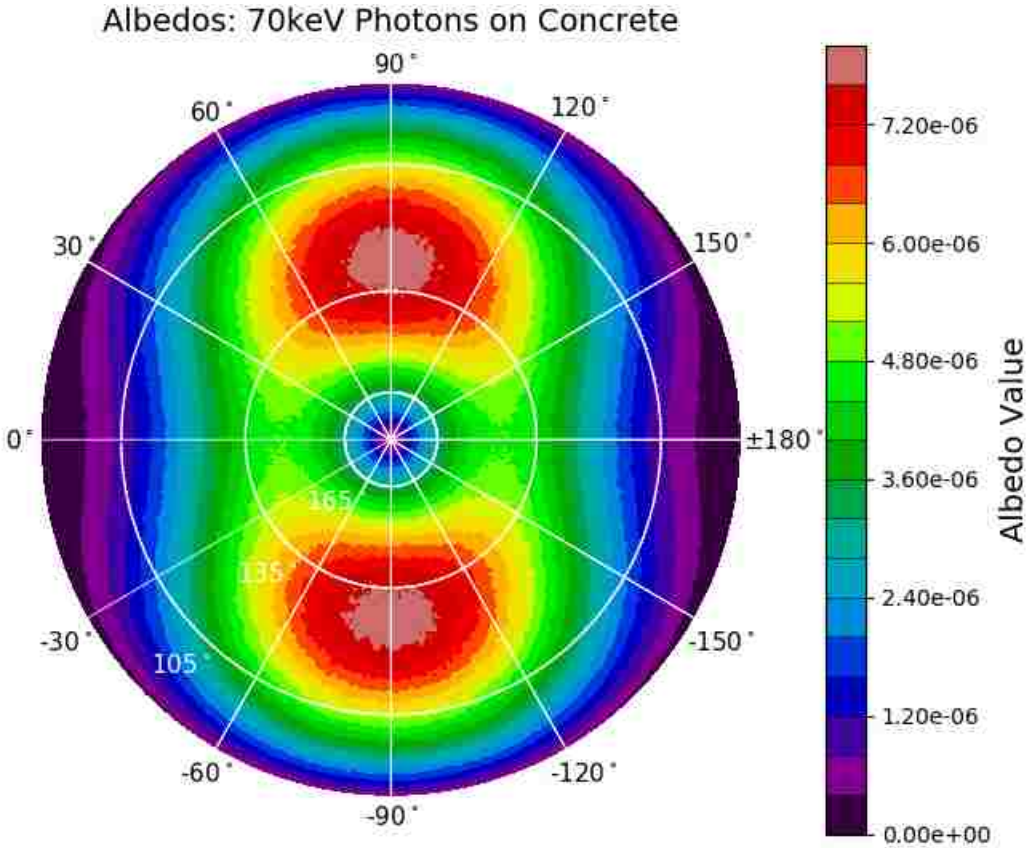

Figure C.13. Albedos for a beam of 70 keV polarized x-rays incident on a slab of concrete.

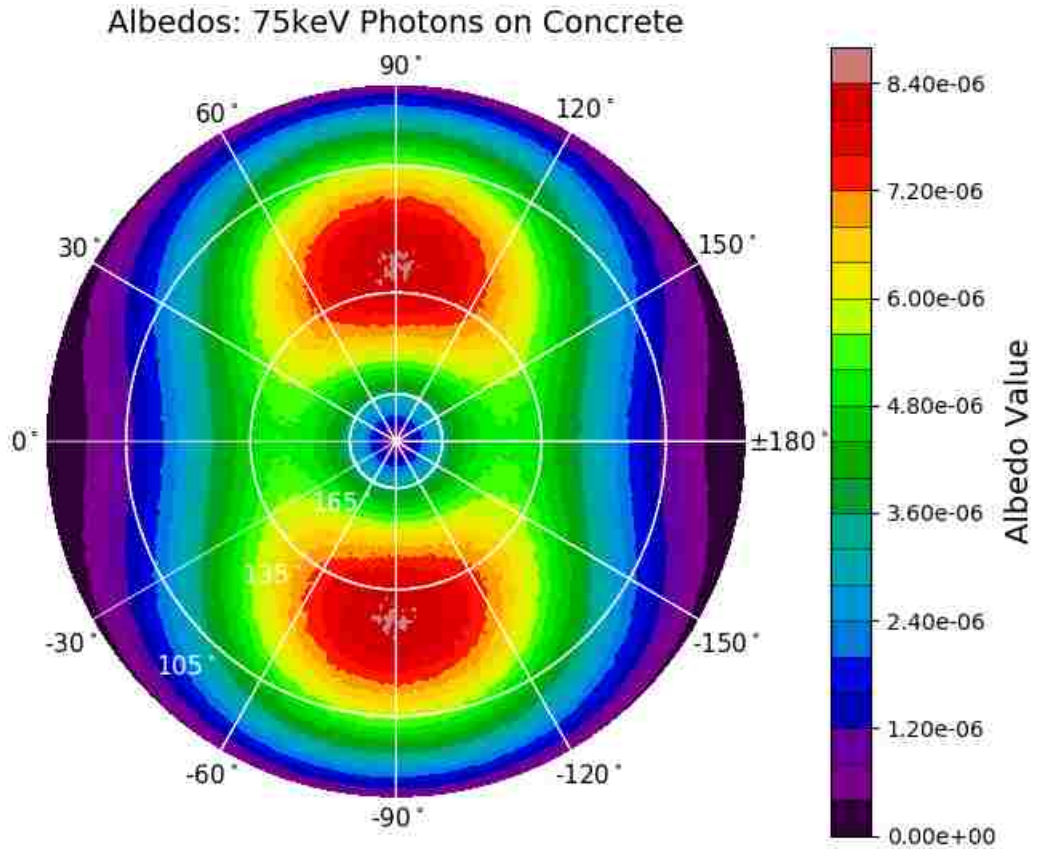

Figure C.14. Albedos for a beam of 75 keV polarized x-rays incident on a slab of concrete.

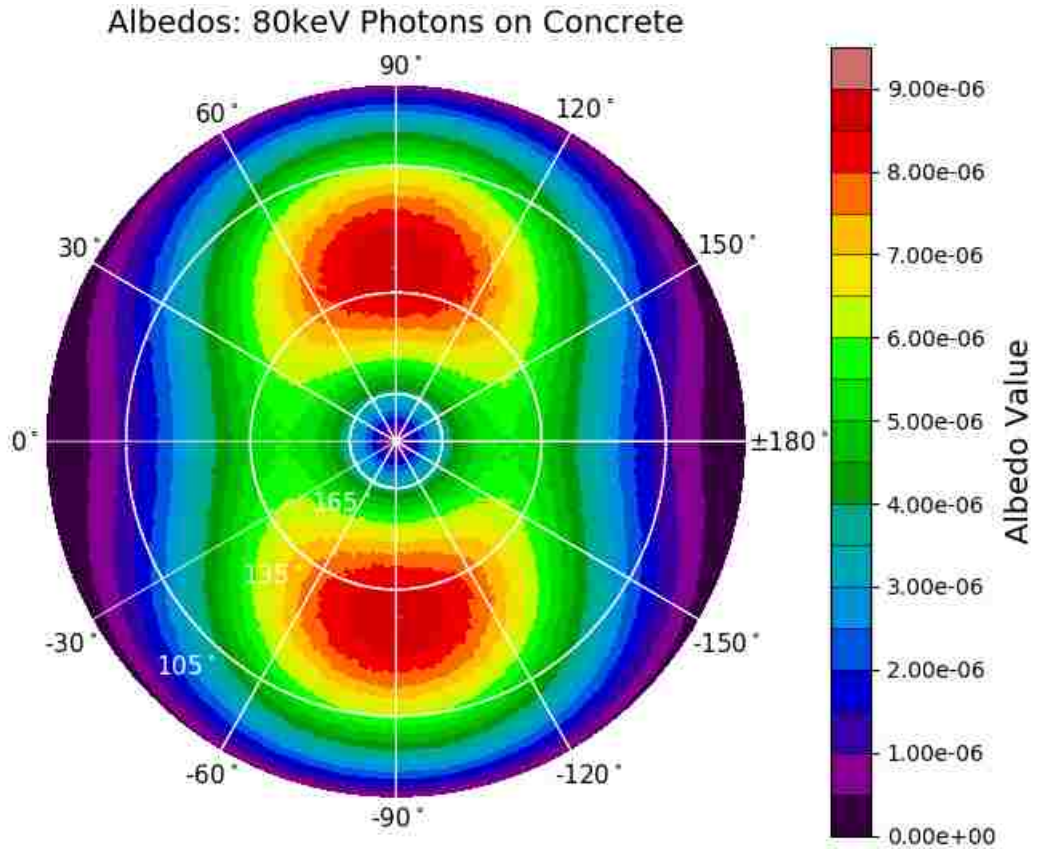

Figure C.15. Albedos for a beam of 80 keV polarized x-rays incident on a slab of concrete.

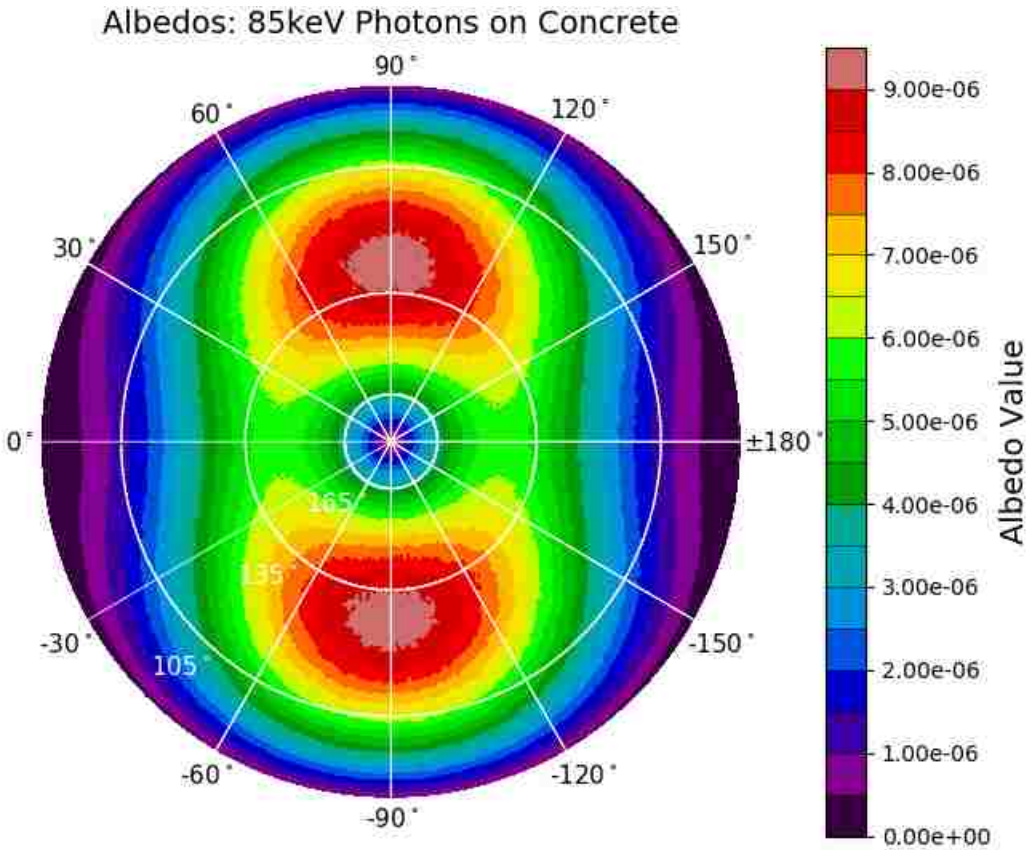

Figure C.16. Albedos for a beam of 85 keV polarized x-rays incident on a slab of concrete.

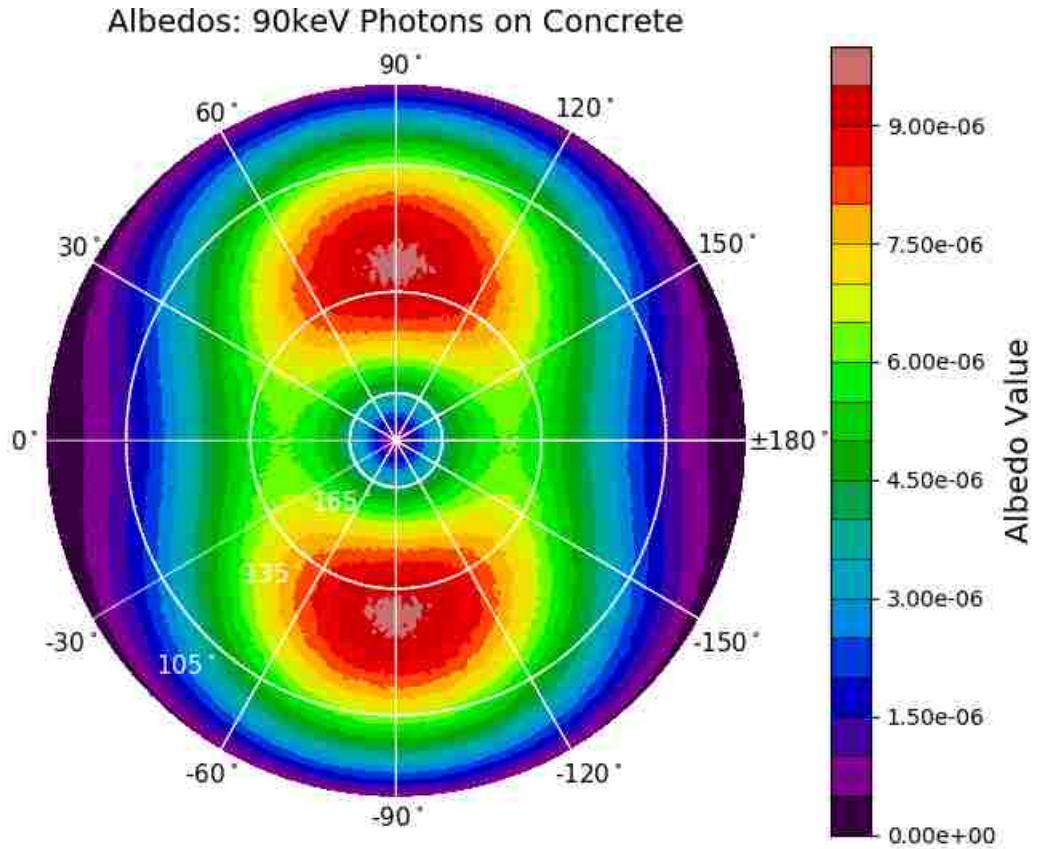

Figure C.17. Albedos for a beam of 90 keV polarized x-rays incident on a slab of concrete.

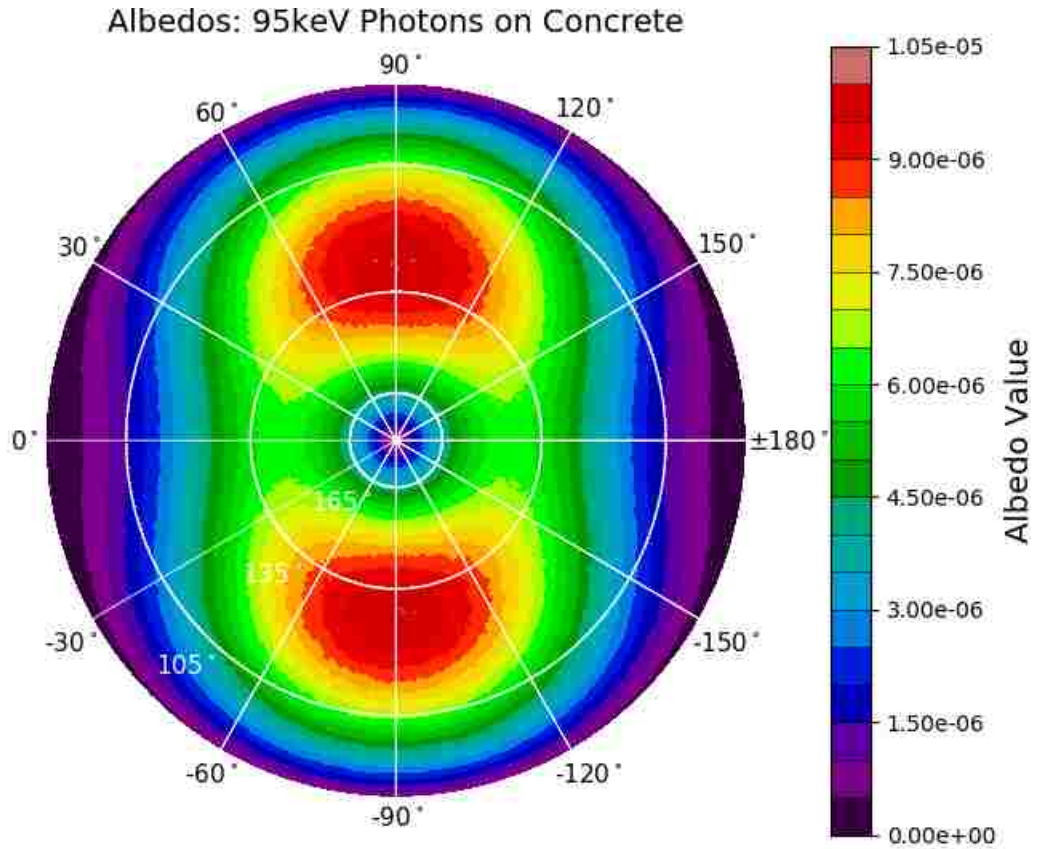

Figure C.18. Albedos for a beam of 95 keV polarized x-rays incident on a slab of concrete.

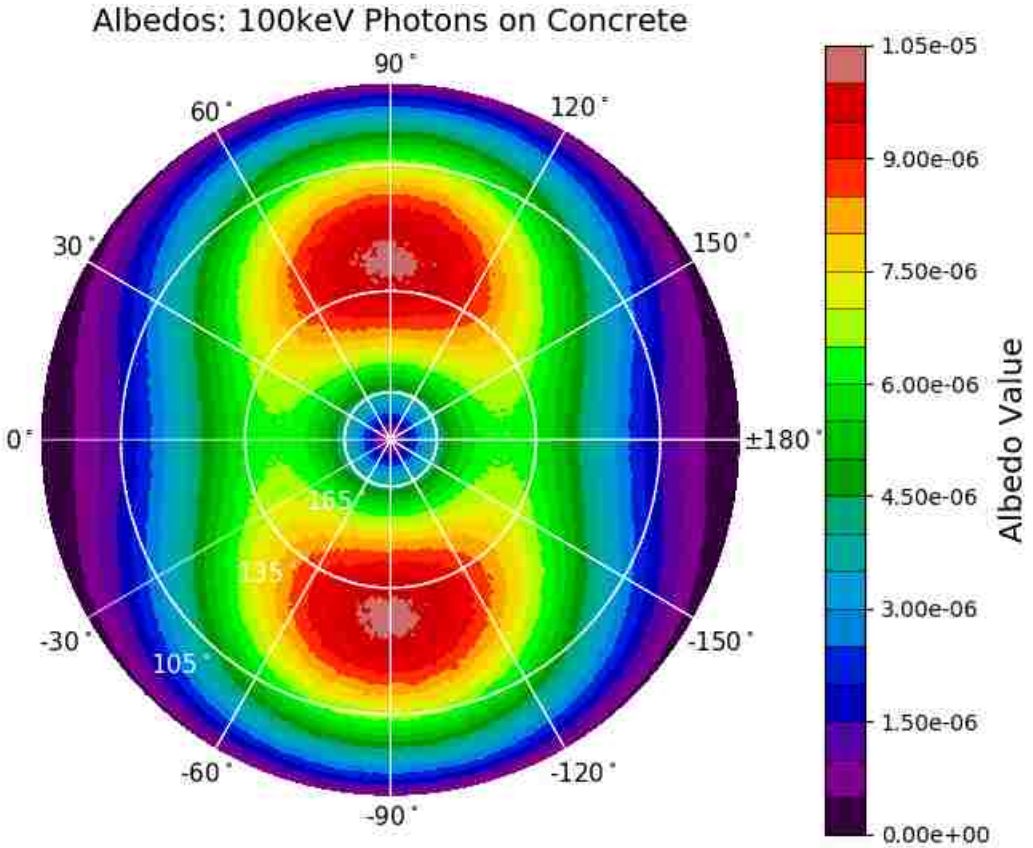

Figure C.19. Albedos for a beam of 100 keV polarized x-rays incident on a slab of concrete.

C.2. Lead Albedo Polar Plots

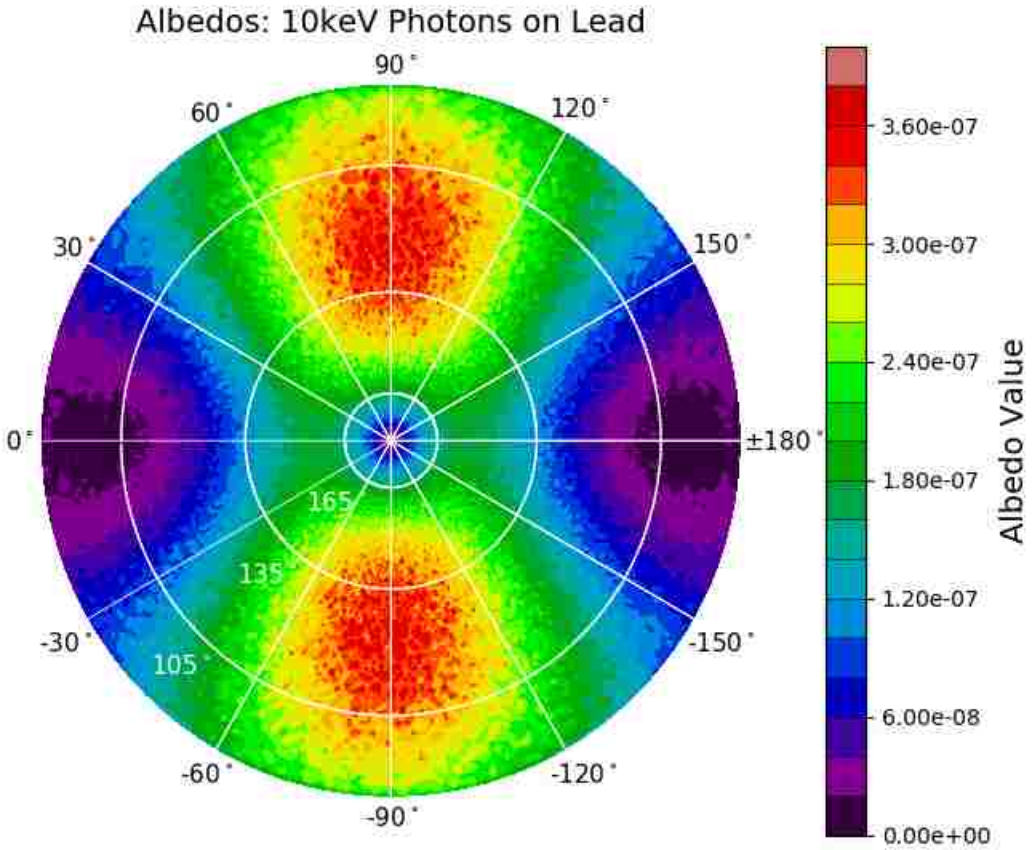

Figure C.20. Albedos for a beam of 10 keV polarized x-rays incident on a slab of lead.

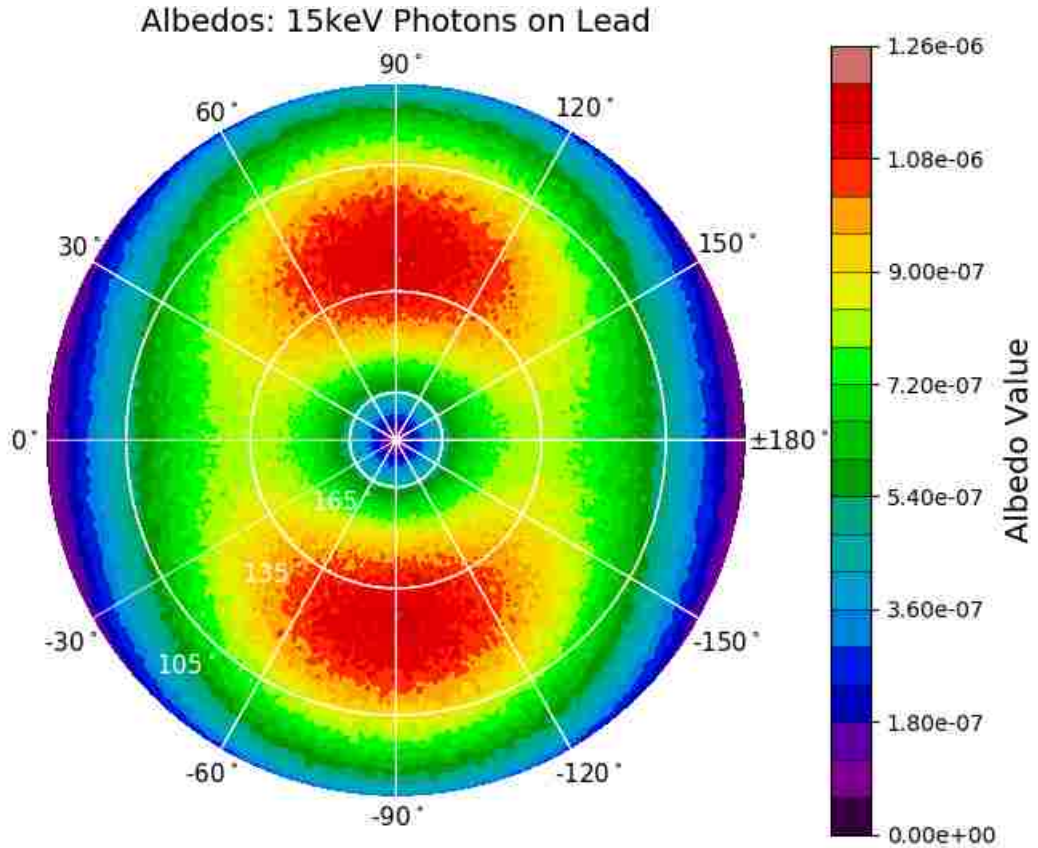

Figure C.21. Albedos for a beam of 15 keV polarized x-rays incident on a slab of lead.

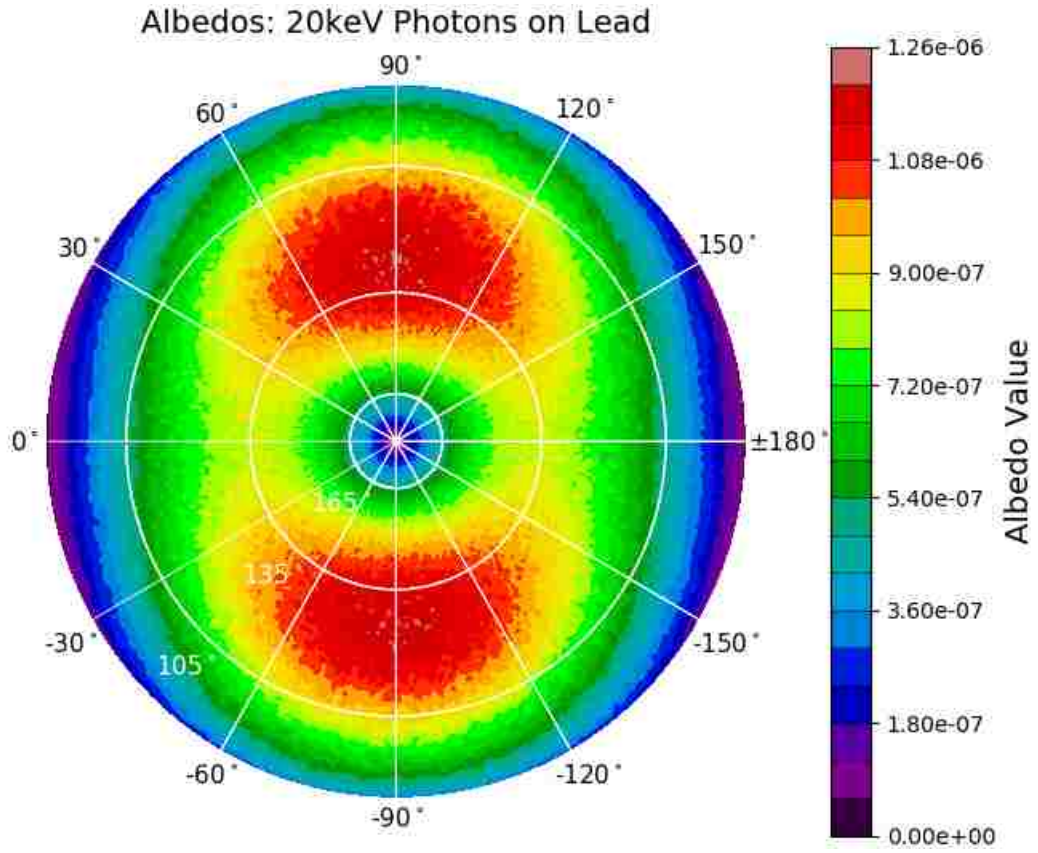

Figure C.22. Albedos for a beam of 20 keV polarized x-rays incident on a slab of lead.

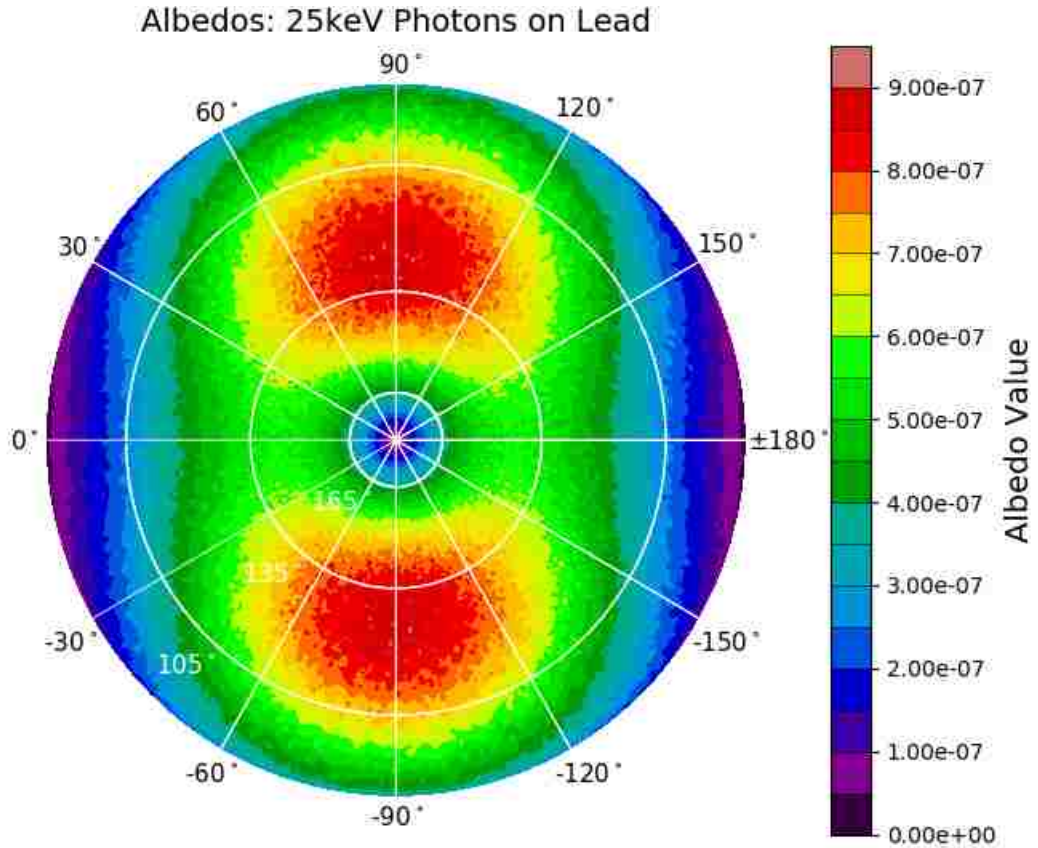

Figure C.23. Albedos for a beam of 25 keV polarized x-rays incident on a slab of lead.

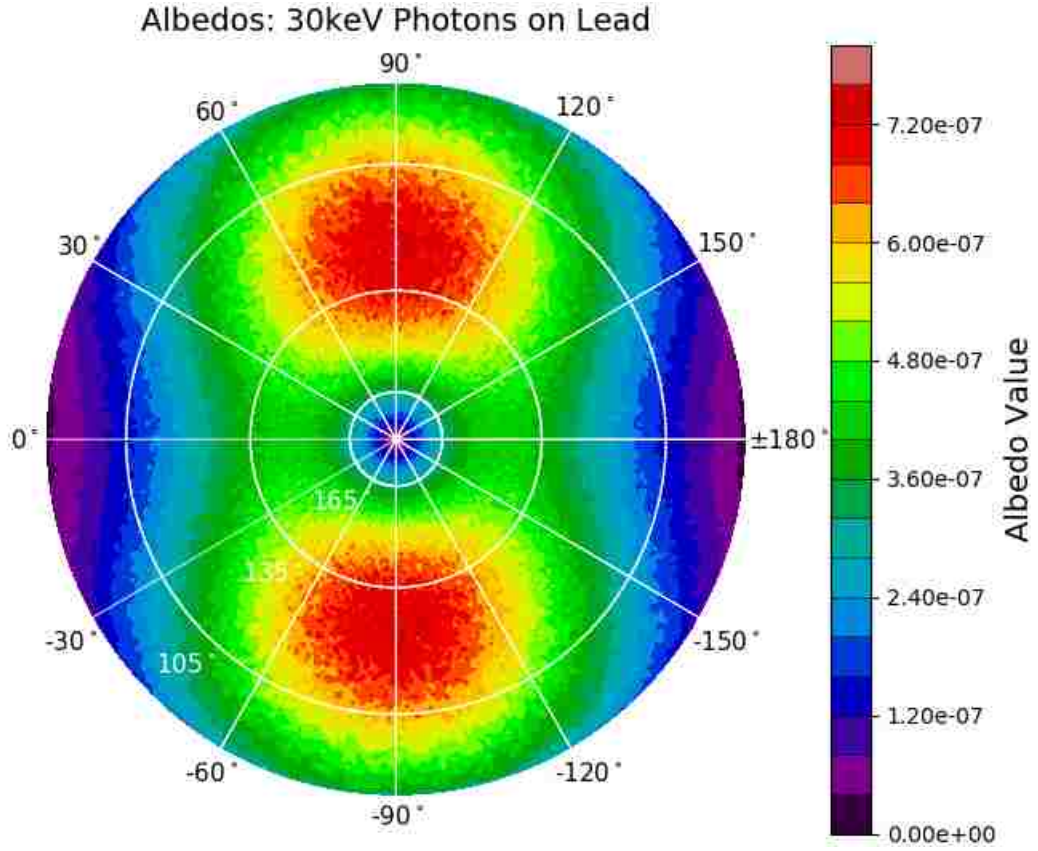

Figure C.24. Albedos for a beam of 30 keV polarized x-rays incident on a slab of lead.

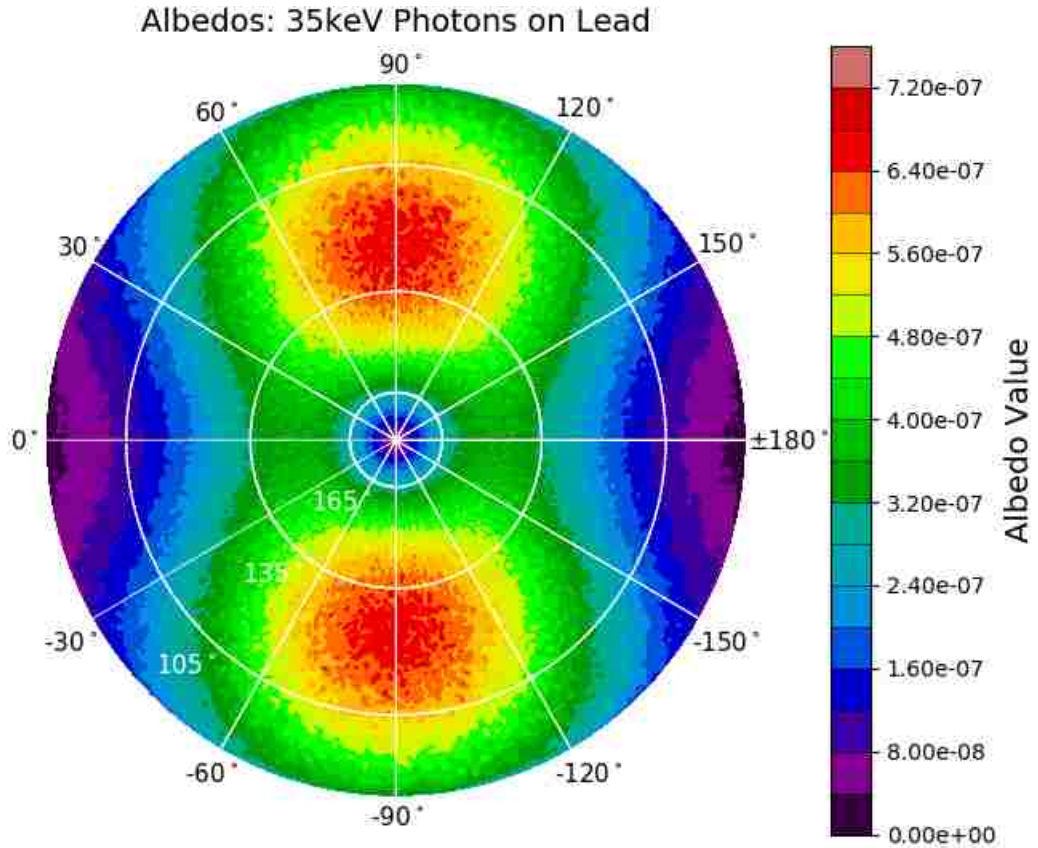

Figure C.25. Albedos for a beam of 35 keV polarized x-rays incident on a slab of lead.

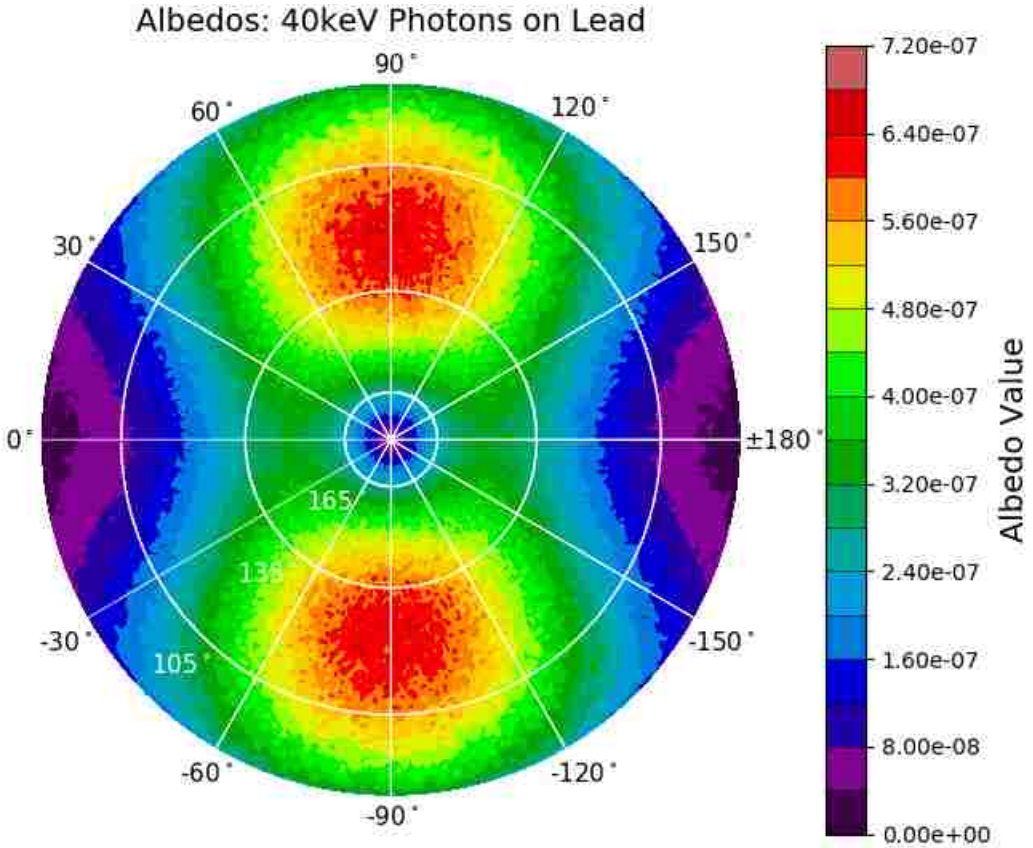

Figure C.26. Albedos for a beam of 40 keV polarized x-rays incident on a slab of lead.

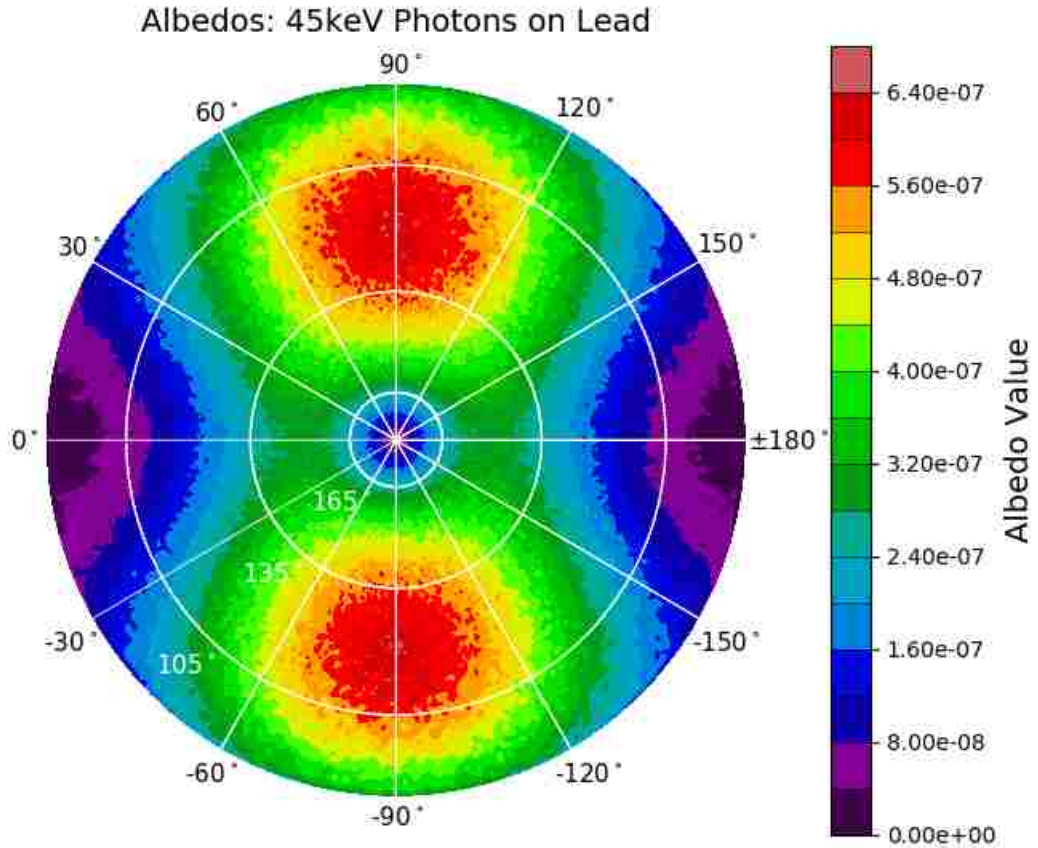

Figure C.27. Albedos for a beam of 45 keV polarized x-rays incident on a slab of lead.

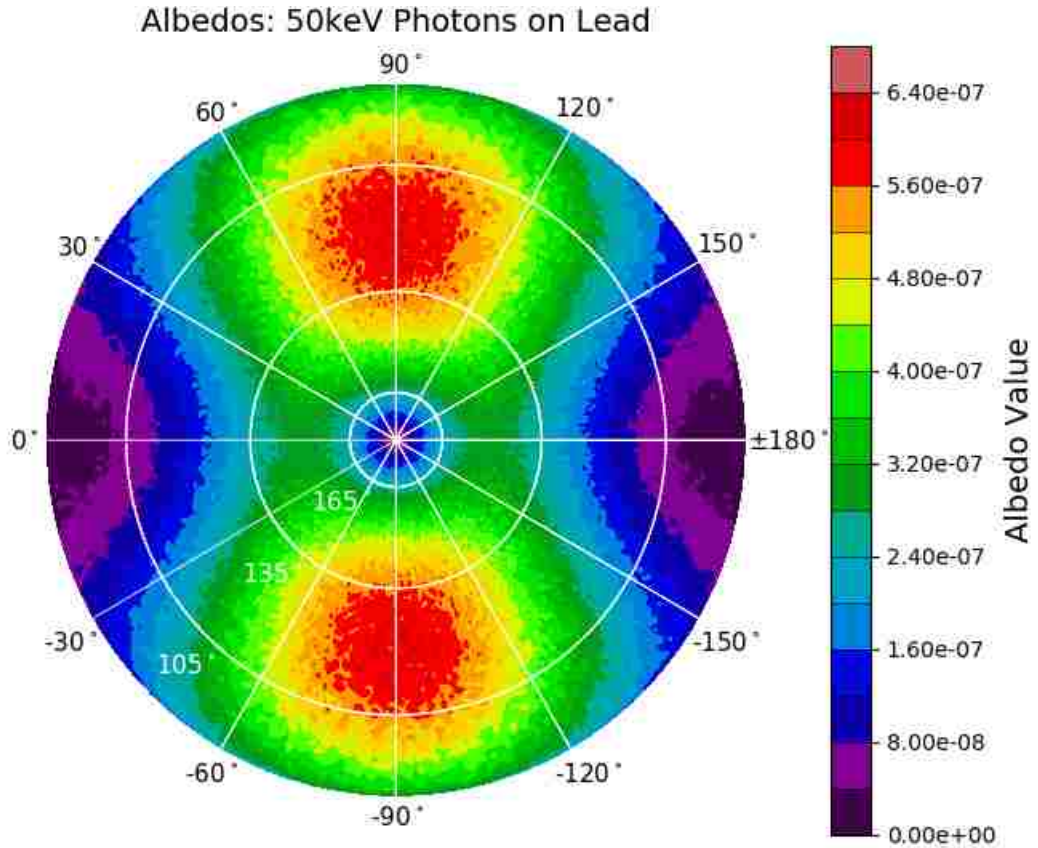

Figure C.28. Albedos for a beam of 50 keV polarized x-rays incident on a slab of lead.

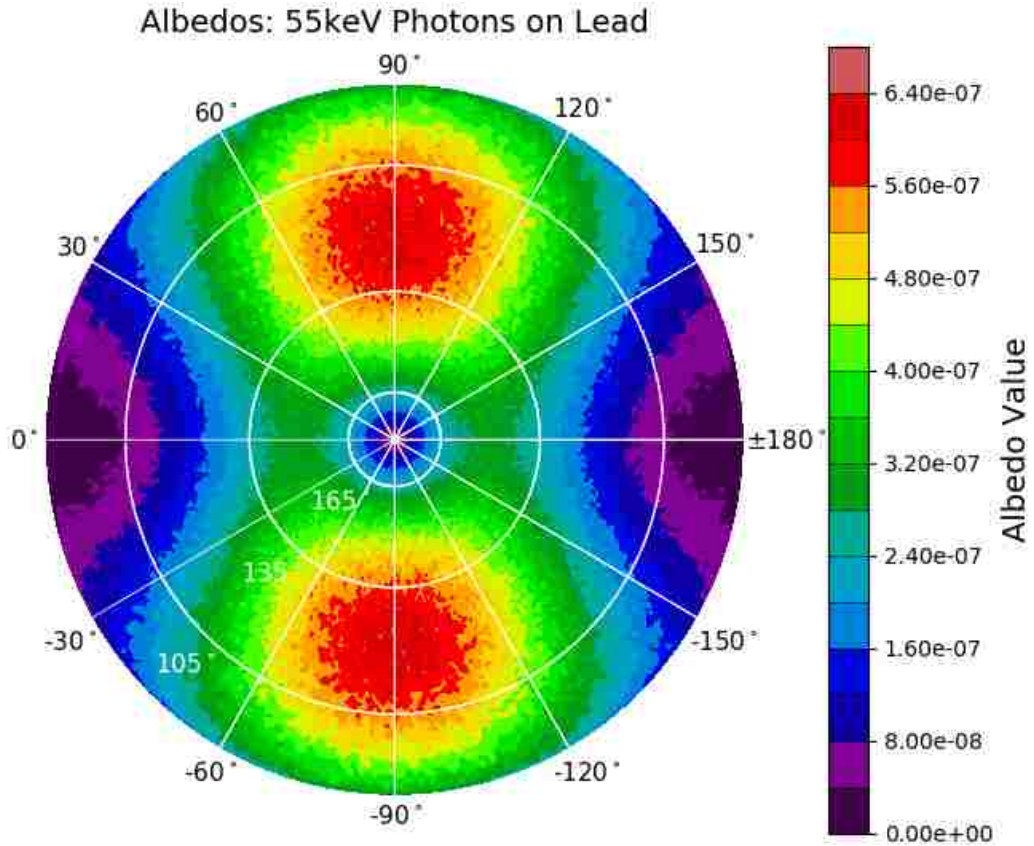

Figure C.29. Albedos for a beam of 55 keV polarized x-rays incident on a slab of lead.

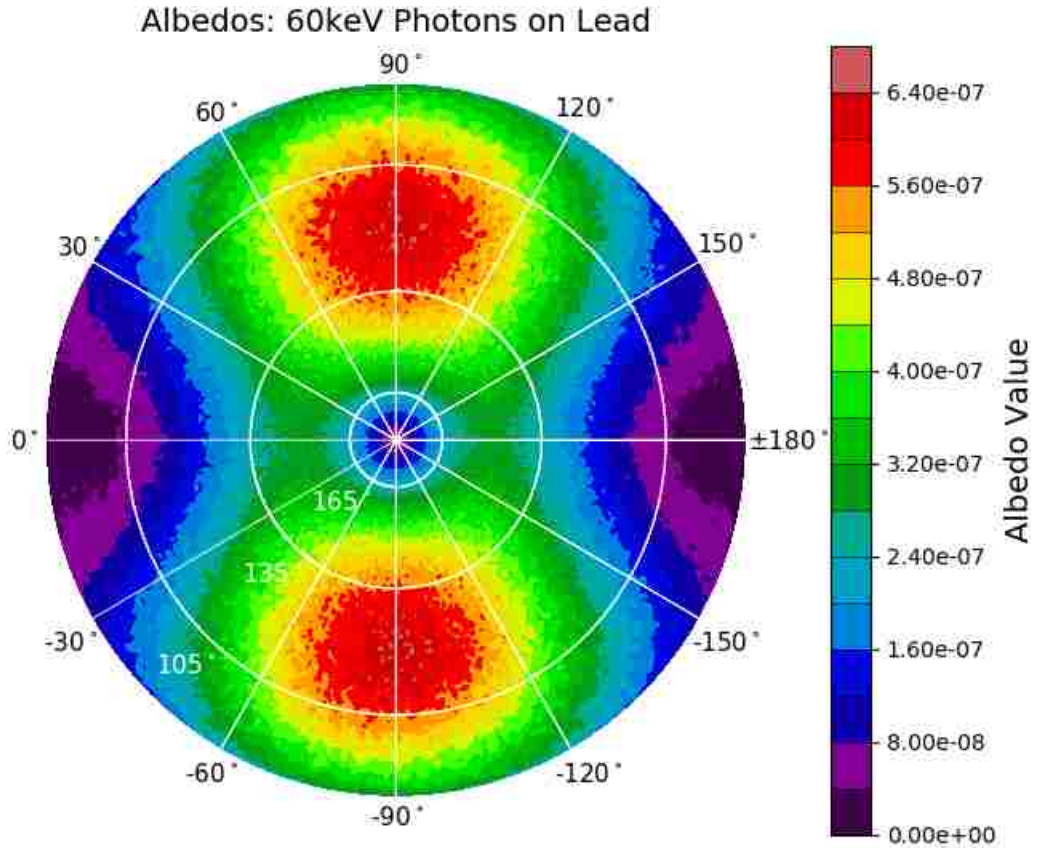

Figure C.30. Albedos for a beam of 60 keV polarized x-rays incident on a slab of lead.

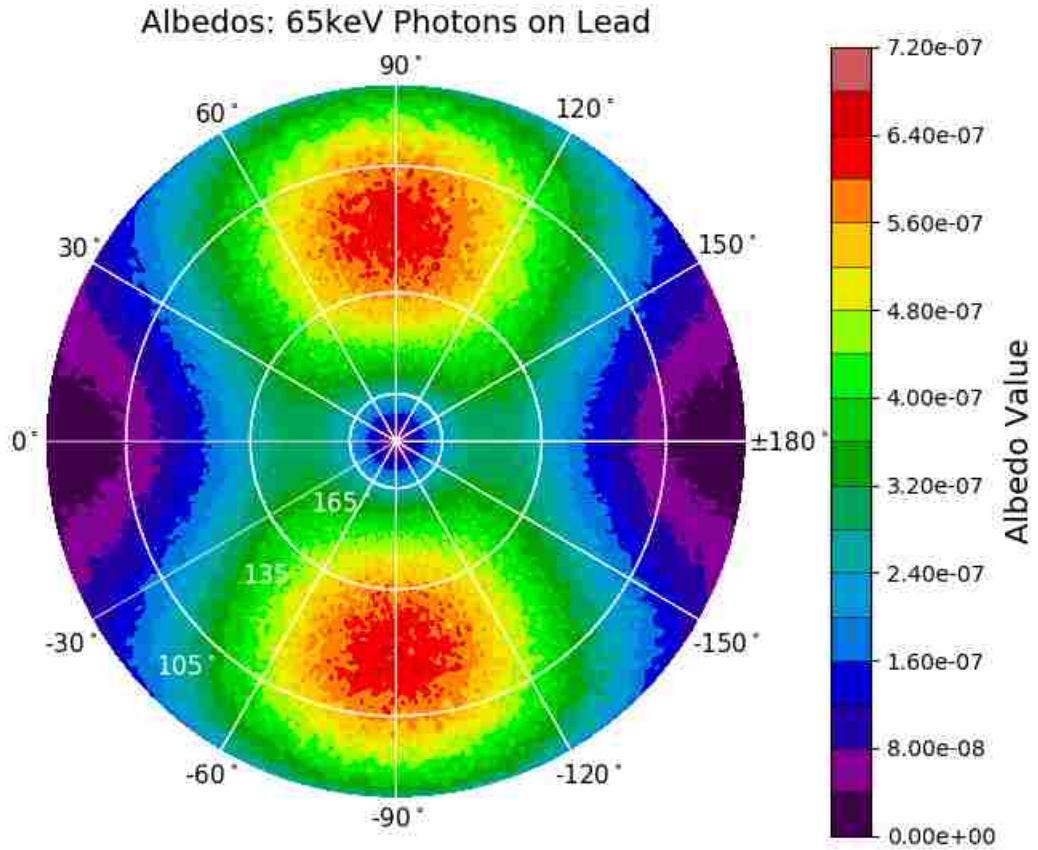

Figure C.31. Albedos for a beam of 65 keV polarized x-rays incident on a slab of lead.

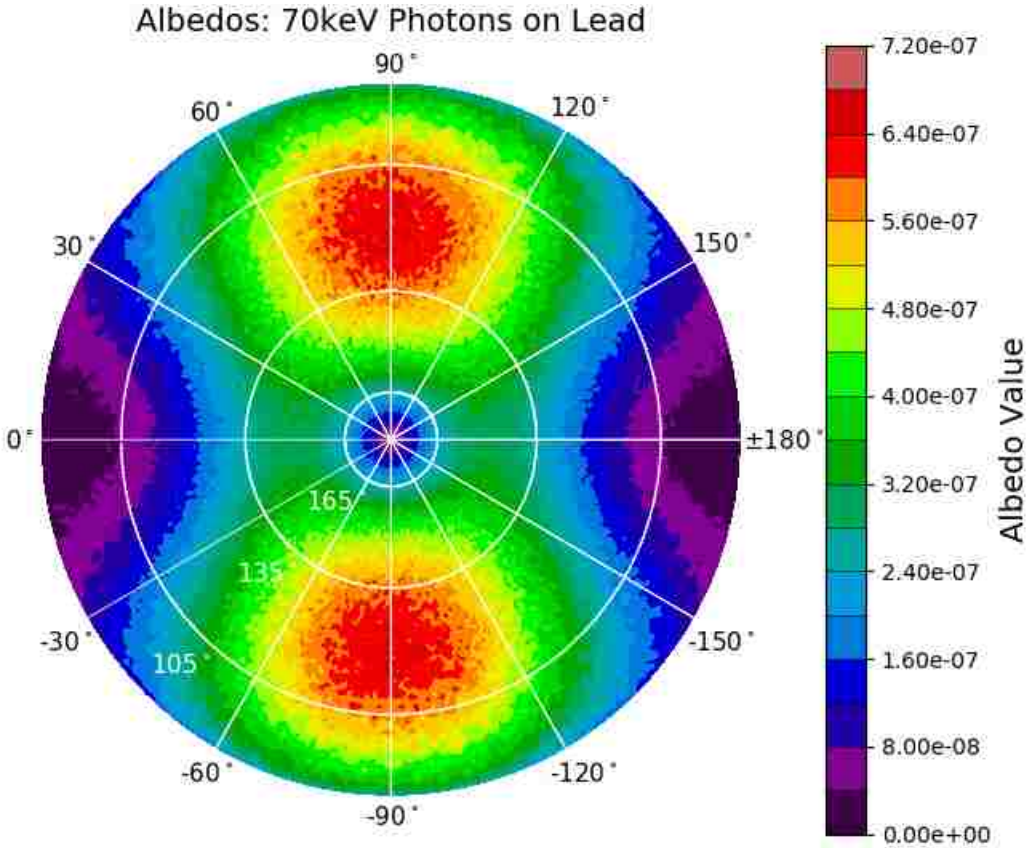

Figure C.32. Albedos for a beam of 70 keV polarized x-rays incident on a slab of lead.

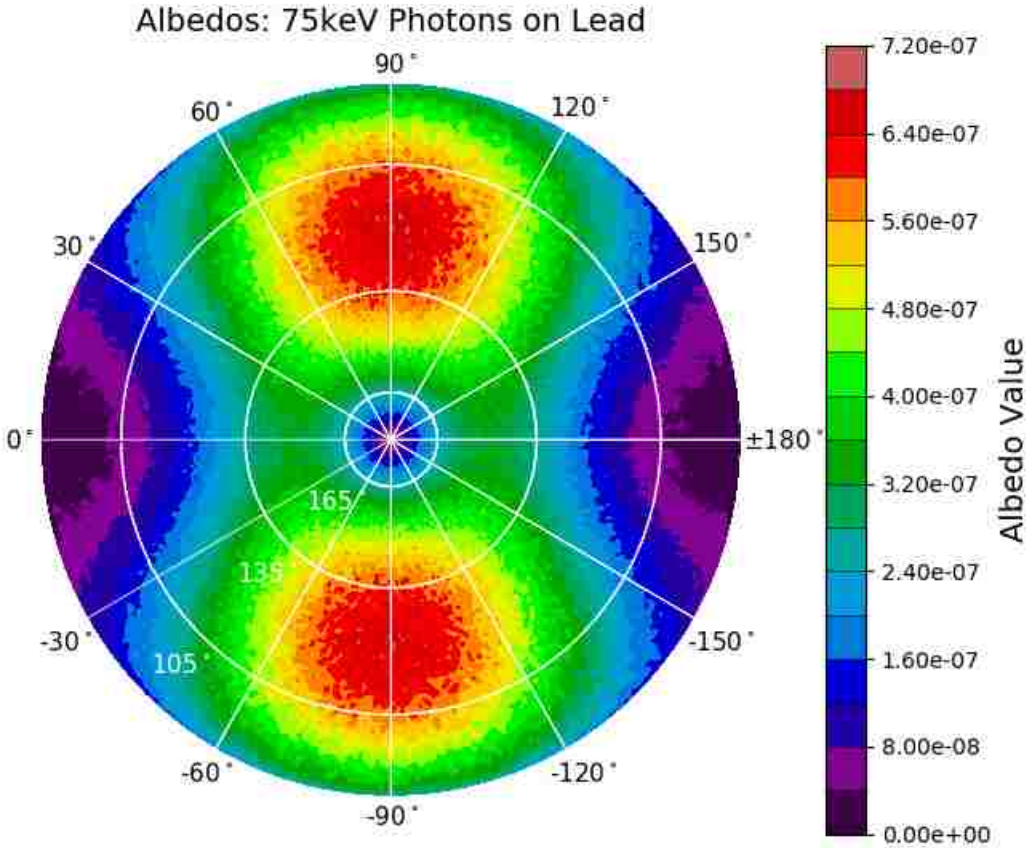

Figure C.33. Albedos for a beam of 75 keV polarized x-rays incident on a slab of lead.

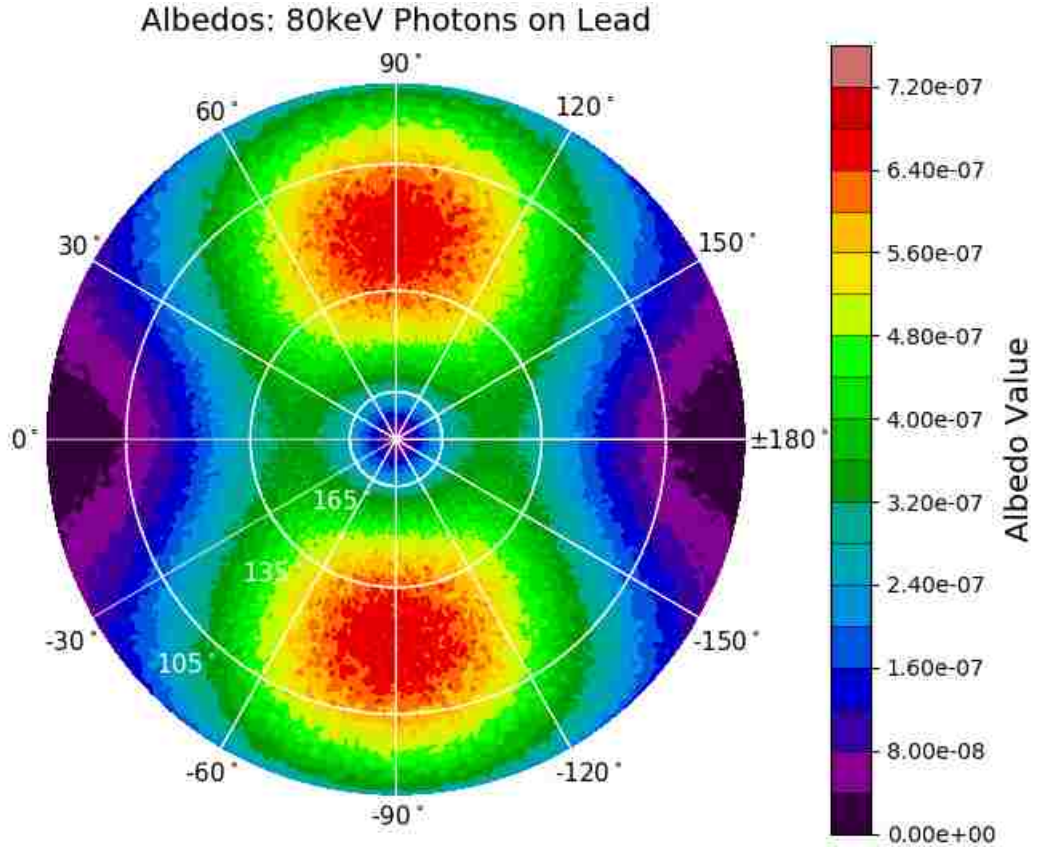

Figure C.34. Albedos for a beam of 80 keV polarized x-rays incident on a slab of lead.

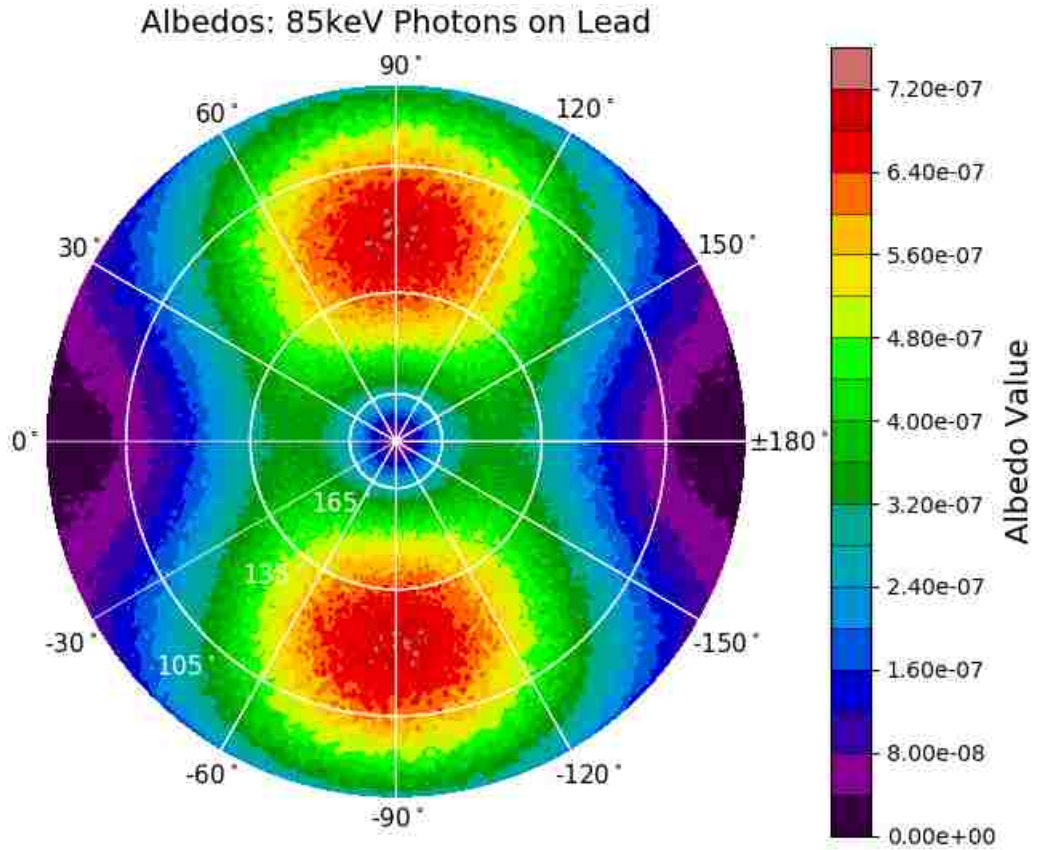

Figure C.35. Albedos for a beam of 85 keV polarized x-rays incident on a slab of lead.

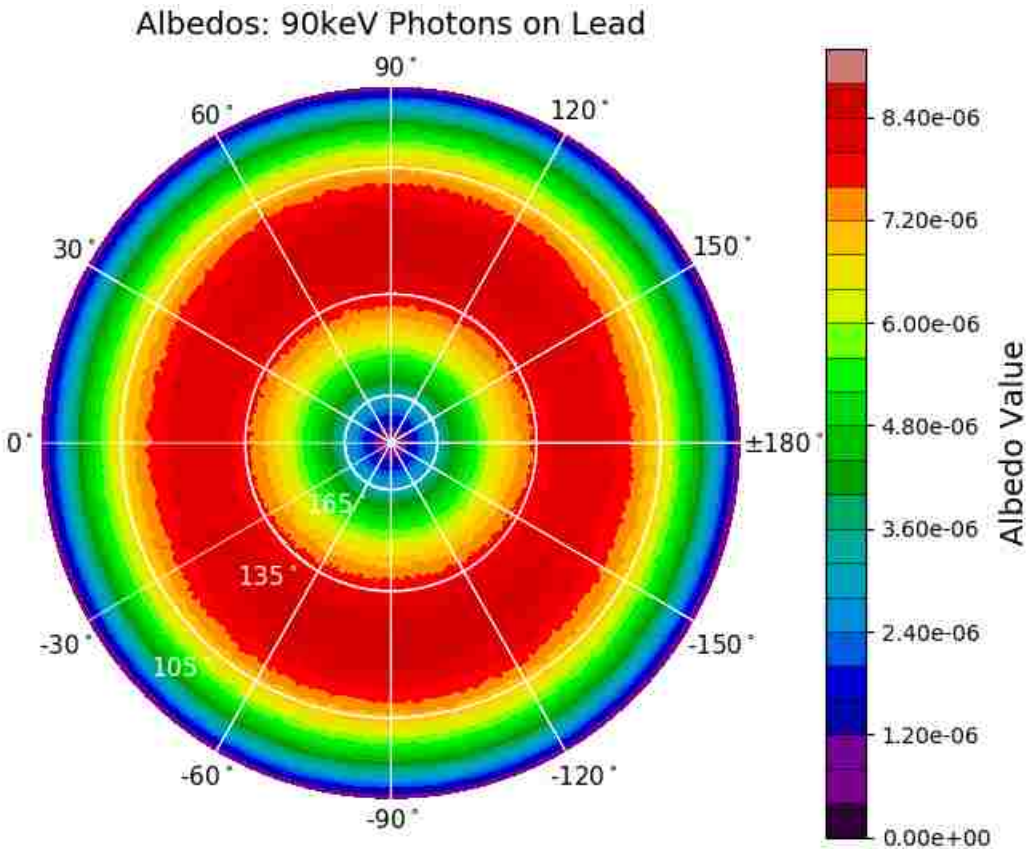

Figure C.36. Albedos for a beam of 90 keV polarized x-rays incident on a slab of lead.

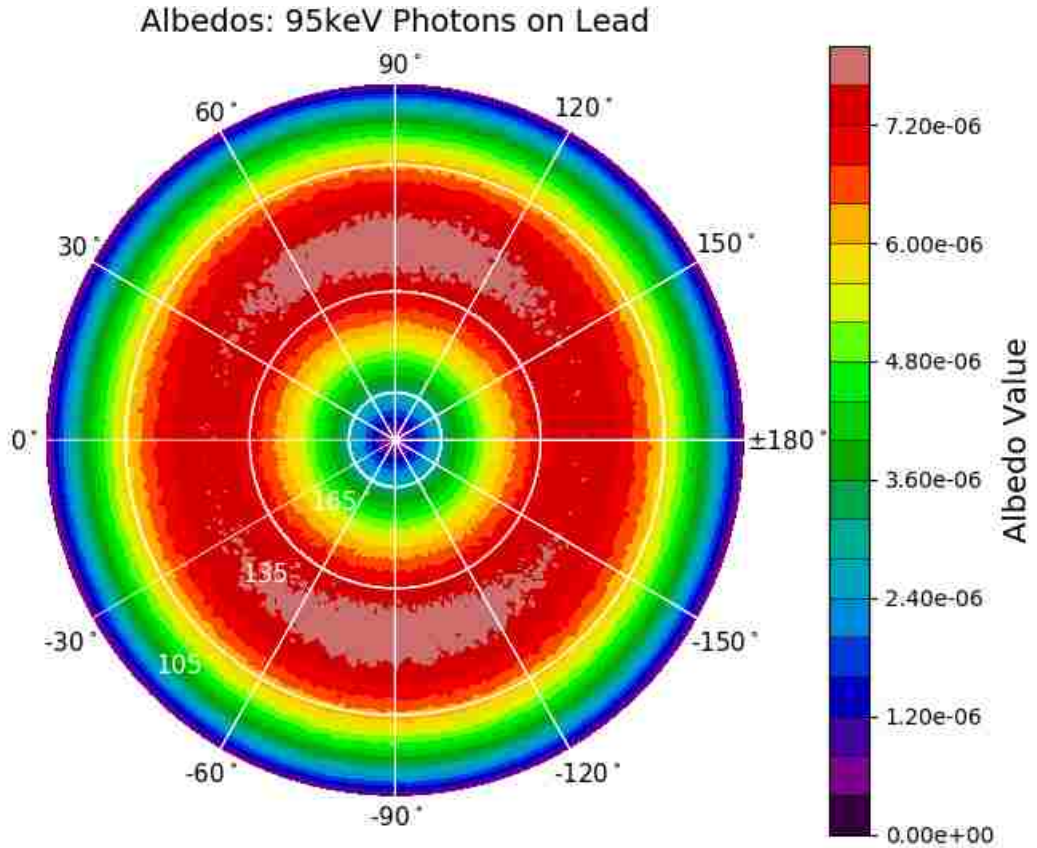

Figure C.37. Albedos for a beam of 95 keV polarized x-rays incident on a slab of lead.

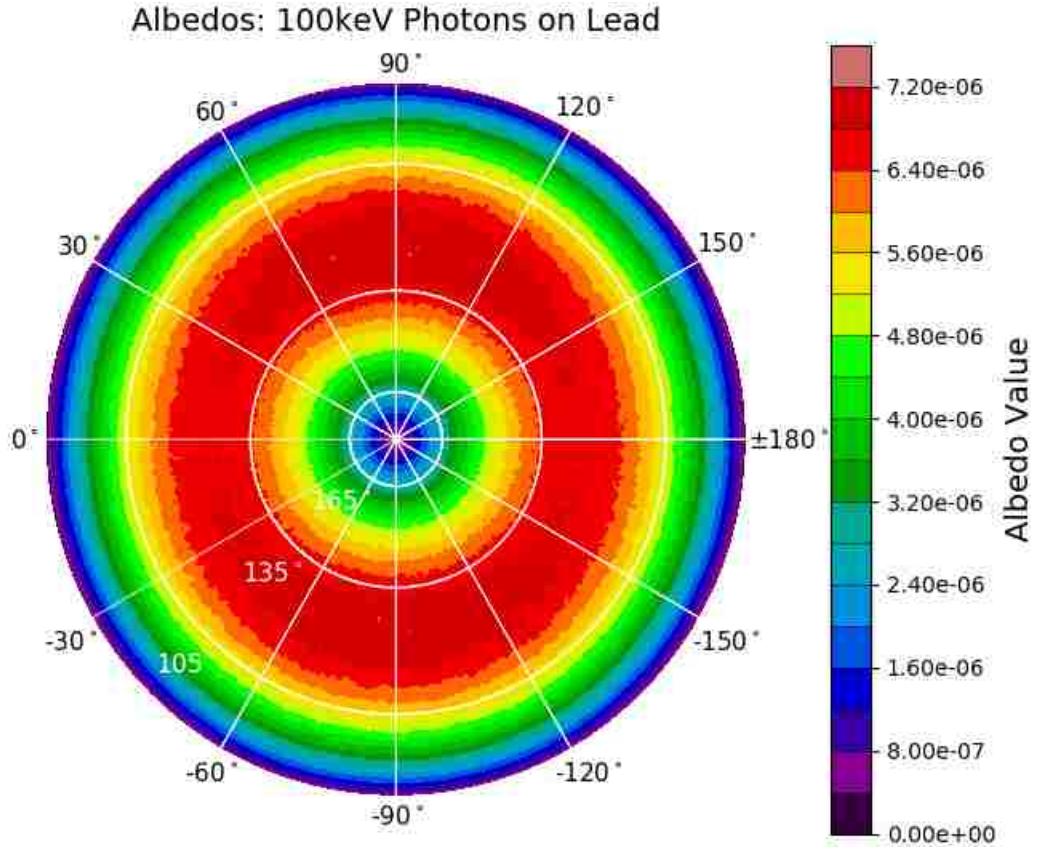

Figure C.38. Albedos for a beam of 100 keV polarized x-rays incident on a slab of lead.

C.3. NIST Defined Steel Albedo Polar Plots

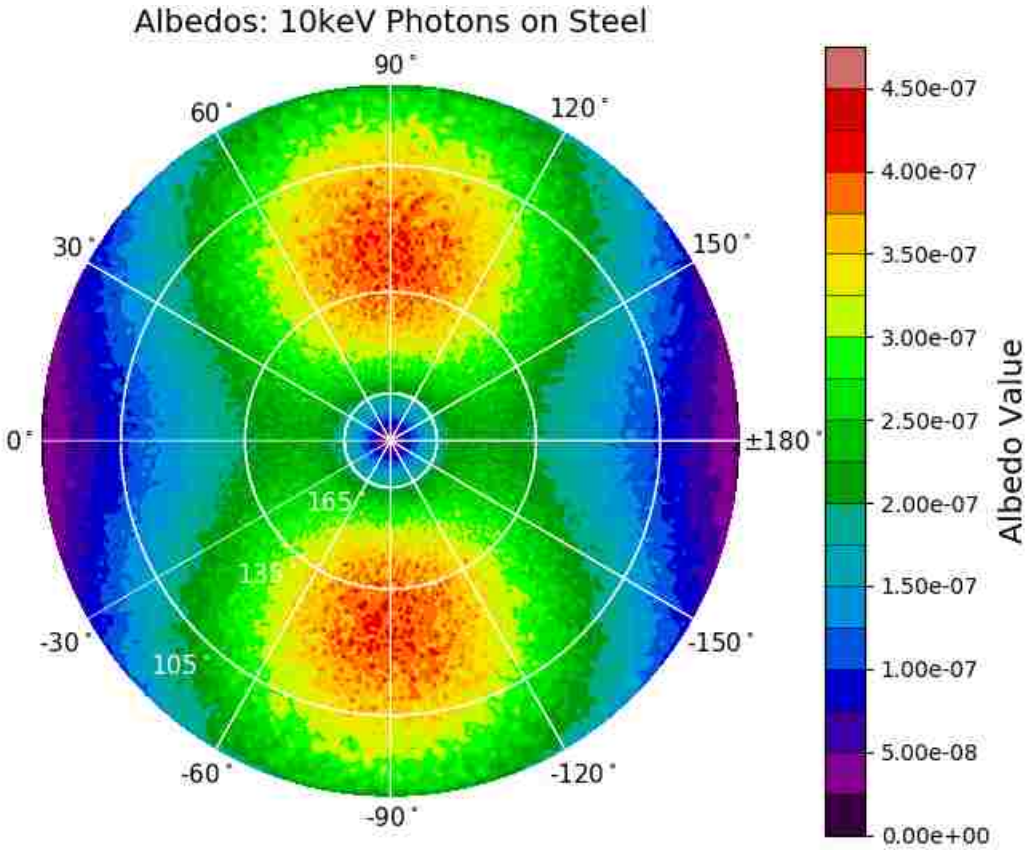

Figure C.39. Albedos for a beam of 10 keV polarized x-rays incident on a slab of steel.

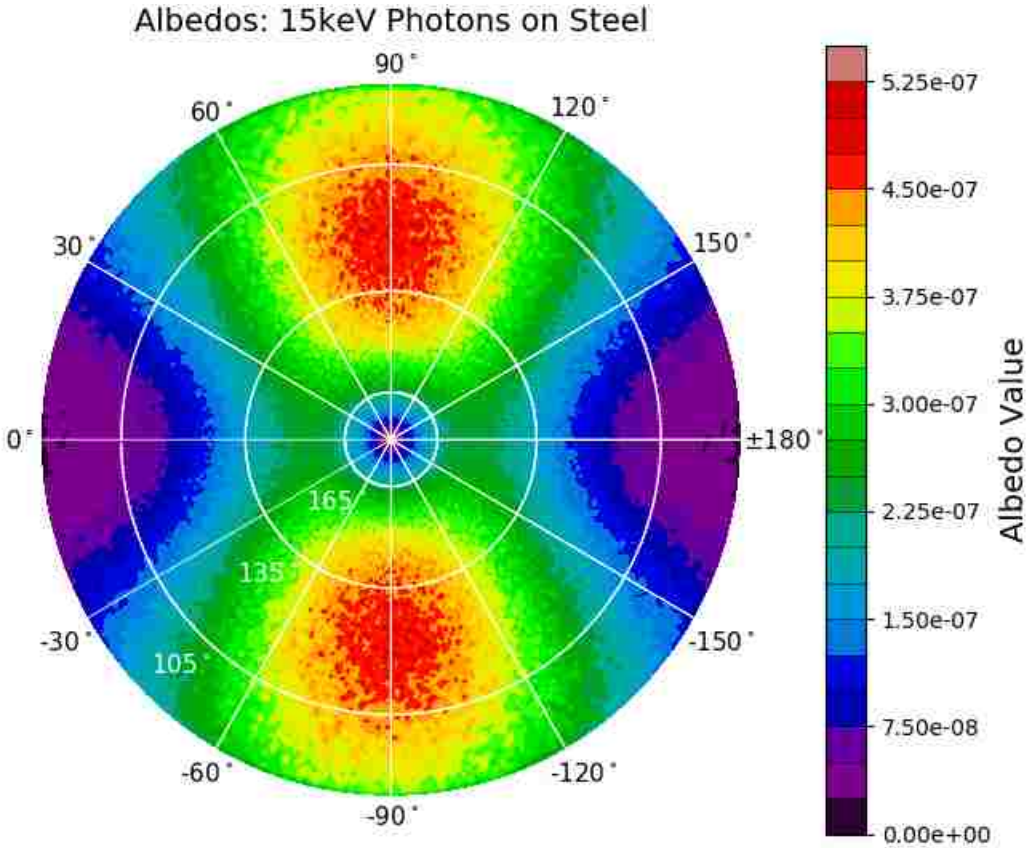

Figure C.40. Albedos for a beam of 15 keV polarized x-rays incident on a slab of steel.

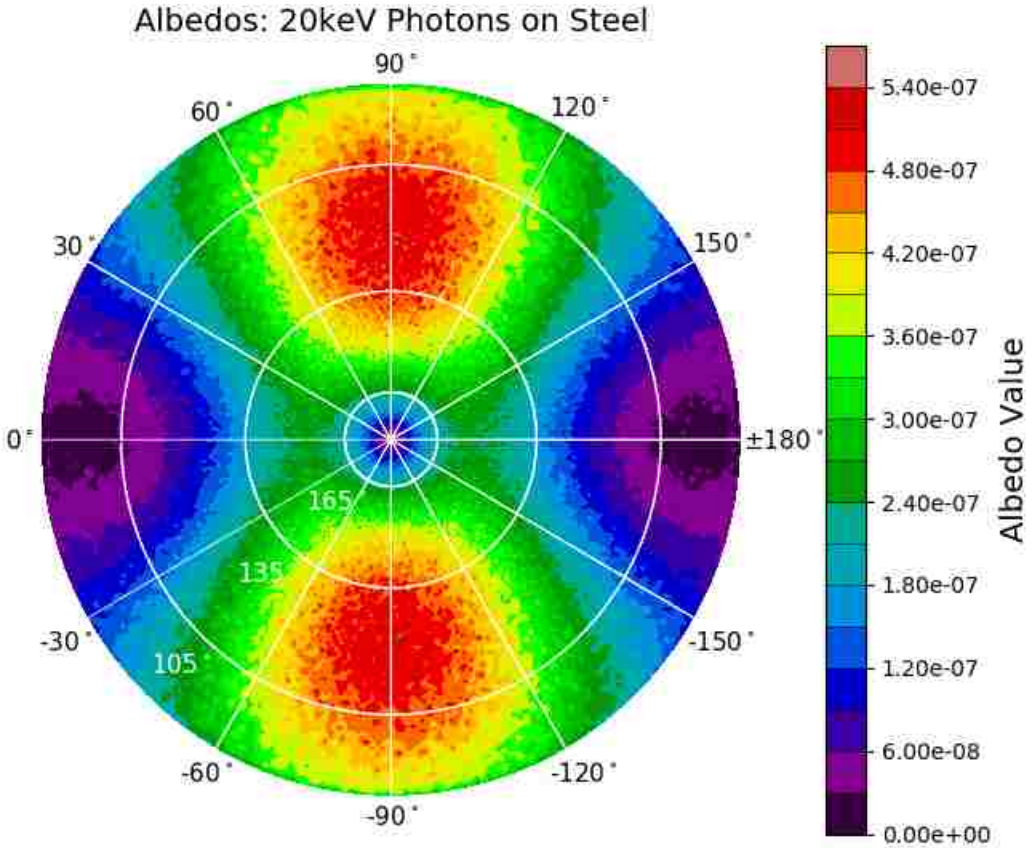

Figure C.41. Albedos for a beam of 20 keV polarized x-rays incident on a slab of steel.

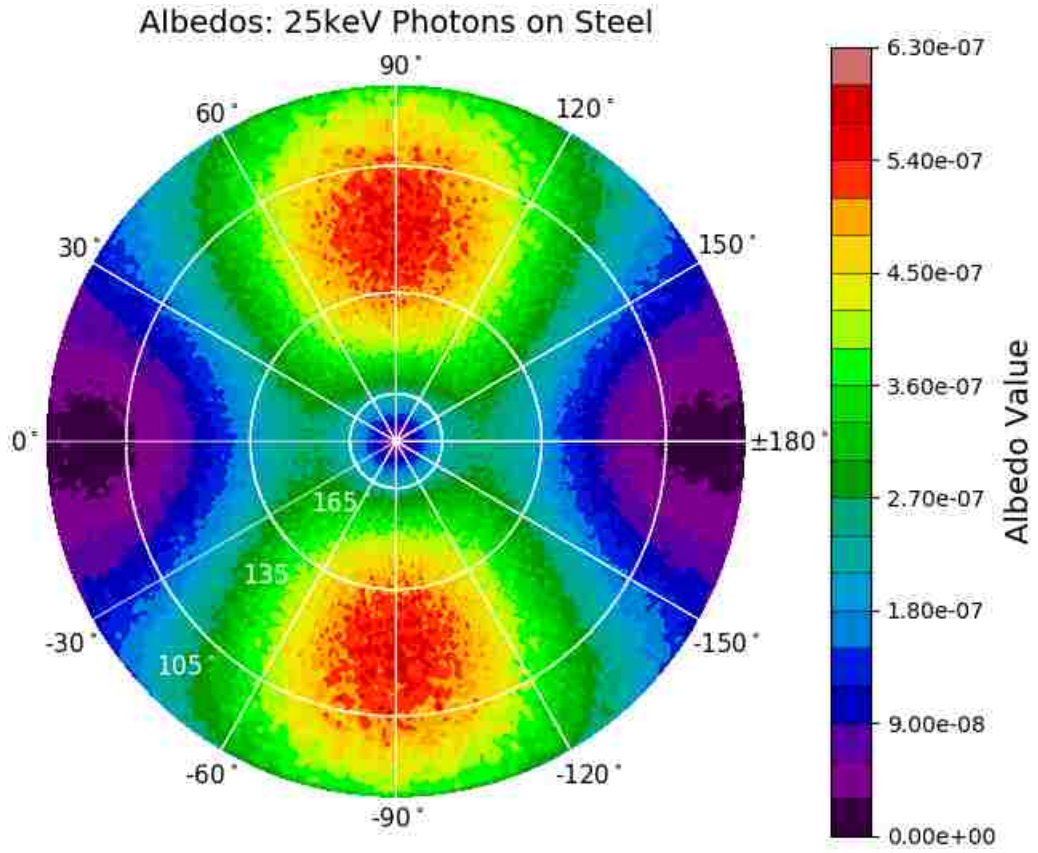

Figure C.42. Albedos for a beam of 25 keV polarized x-rays incident on a slab of steel.

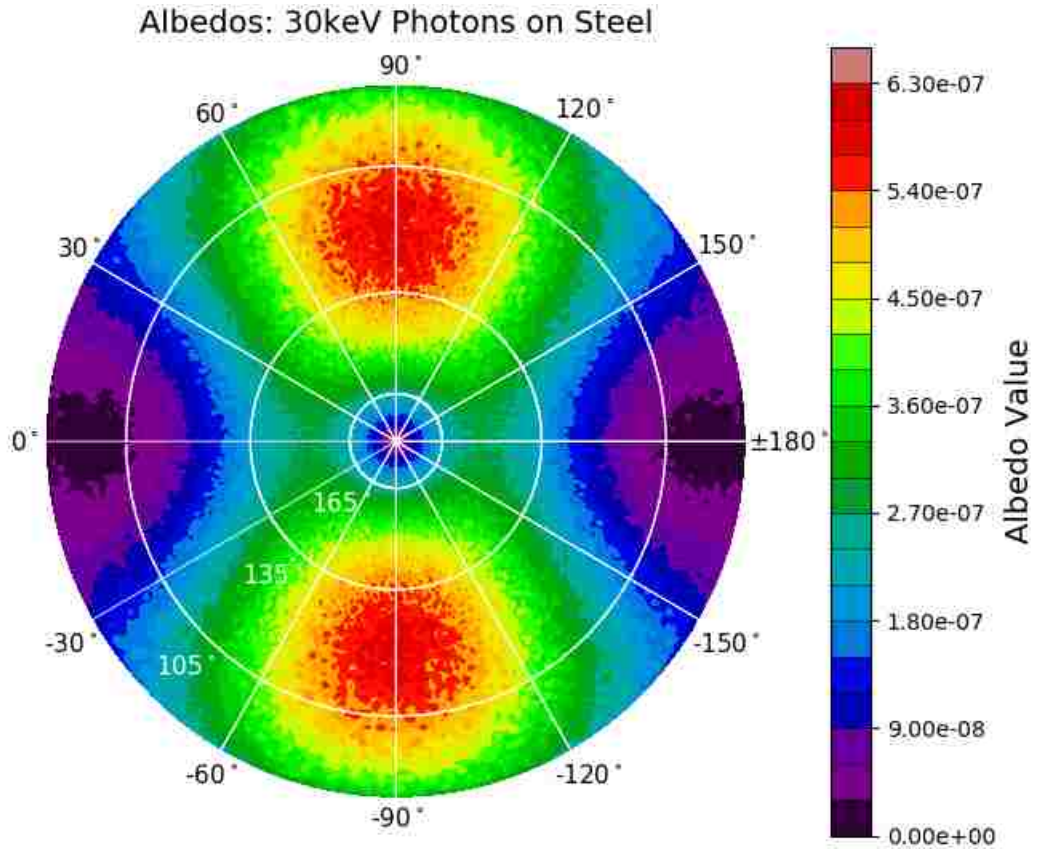

Figure C.43. Albedos for a beam of 30 keV polarized x-rays incident on a slab of steel.

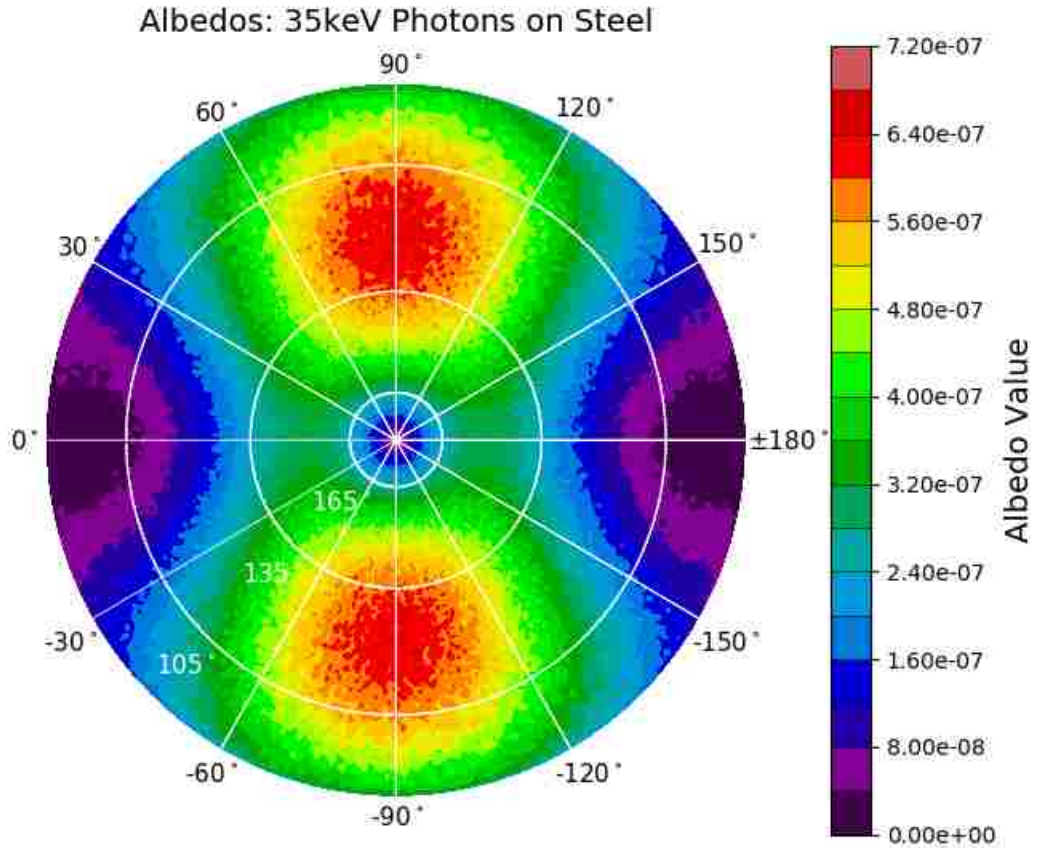

Figure C.44. Albedos for a beam of 35 keV polarized x-rays incident on a slab of steel.

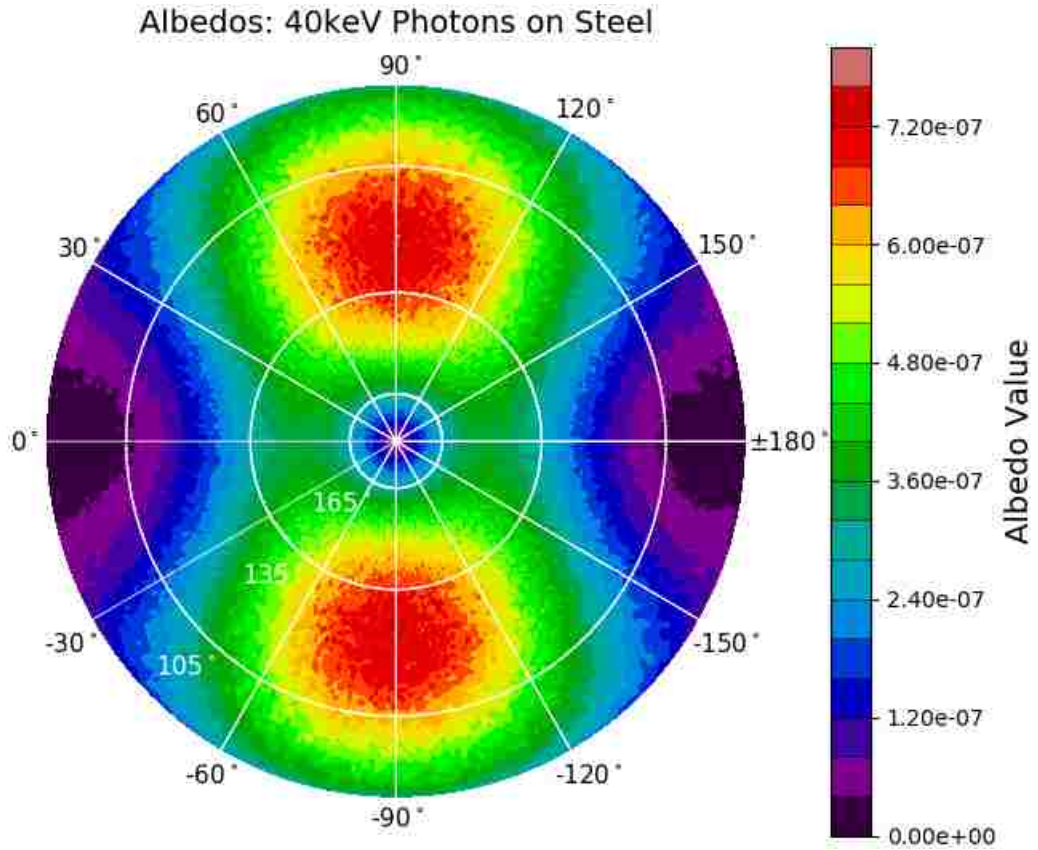

Figure C.45. Albedos for a beam of 40 keV polarized x-rays incident on a slab of steel.

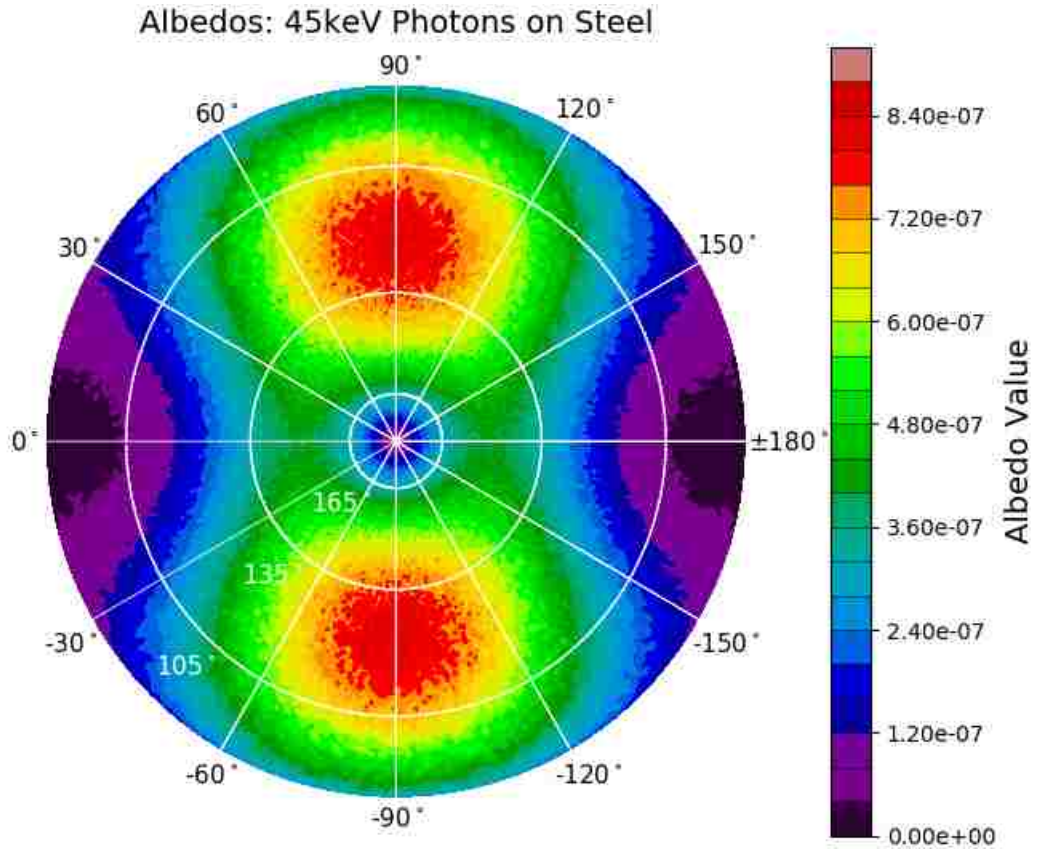

Figure C.46. Albedos for a beam of 45 keV polarized x-rays incident on a slab of steel.

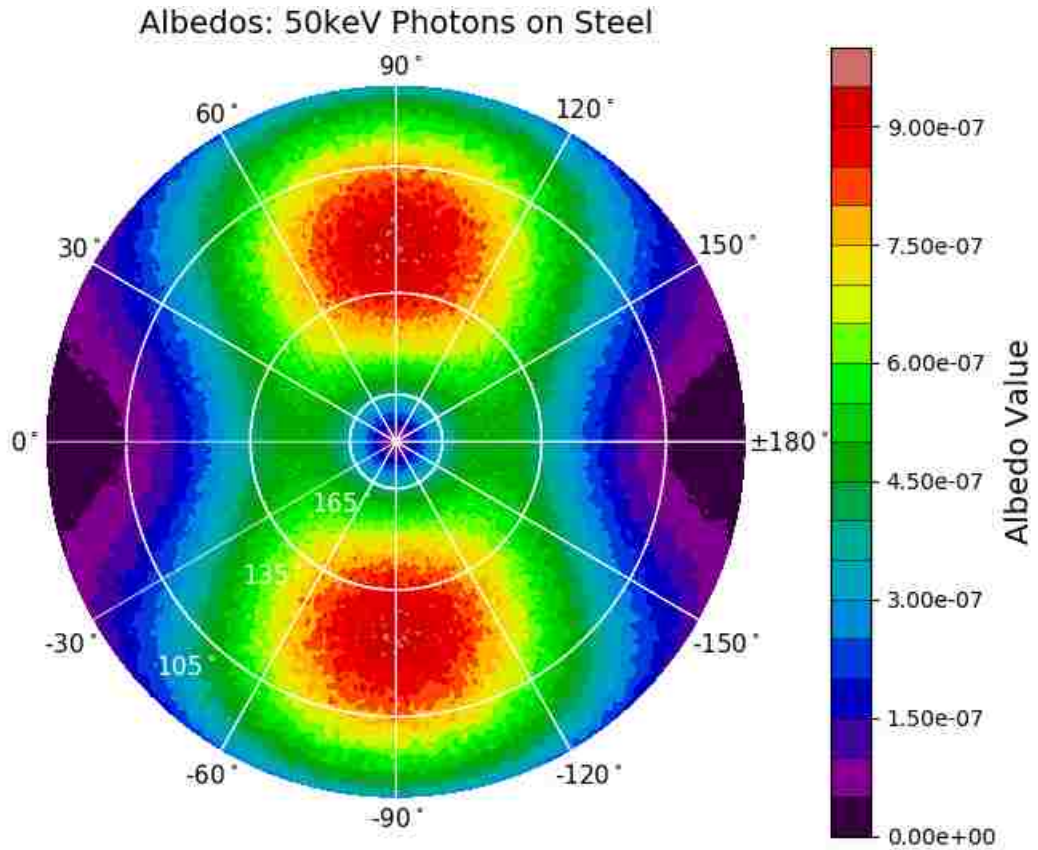

Figure C.47. Albedos for a beam of 50 keV polarized x-rays incident on a slab of steel.

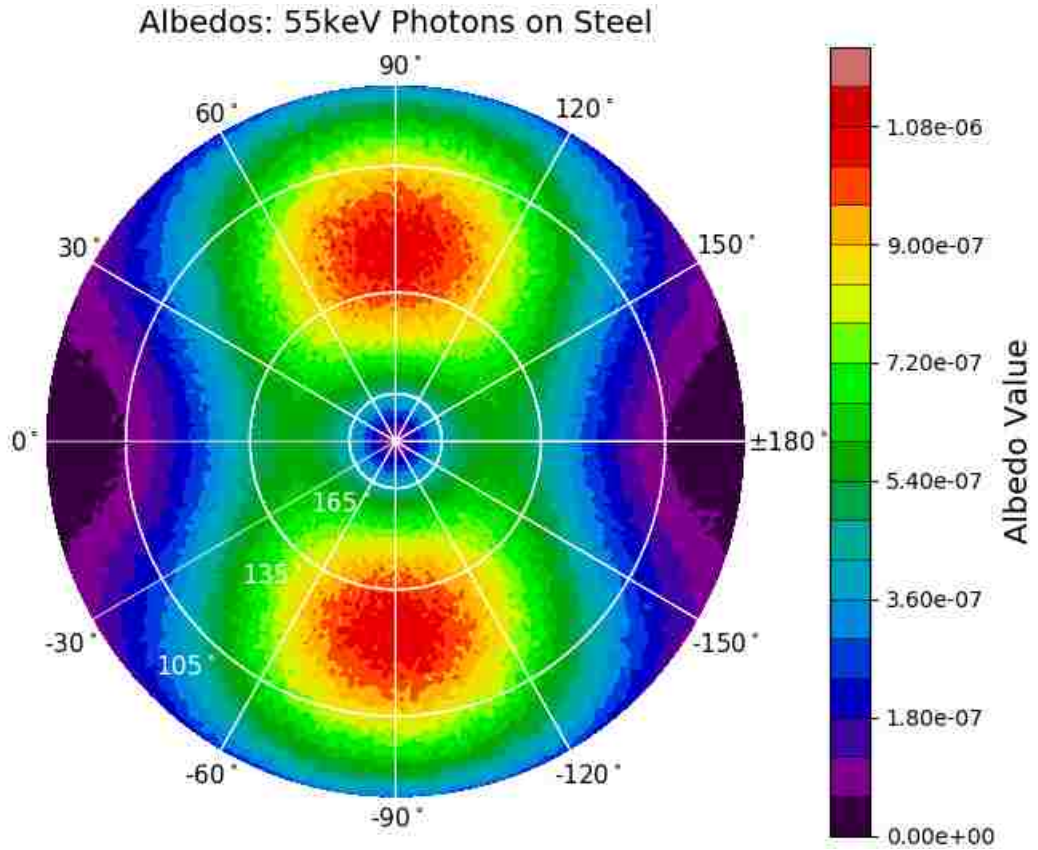

Figure C.48. Albedos for a beam of 55 keV polarized x-rays incident on a slab of steel.

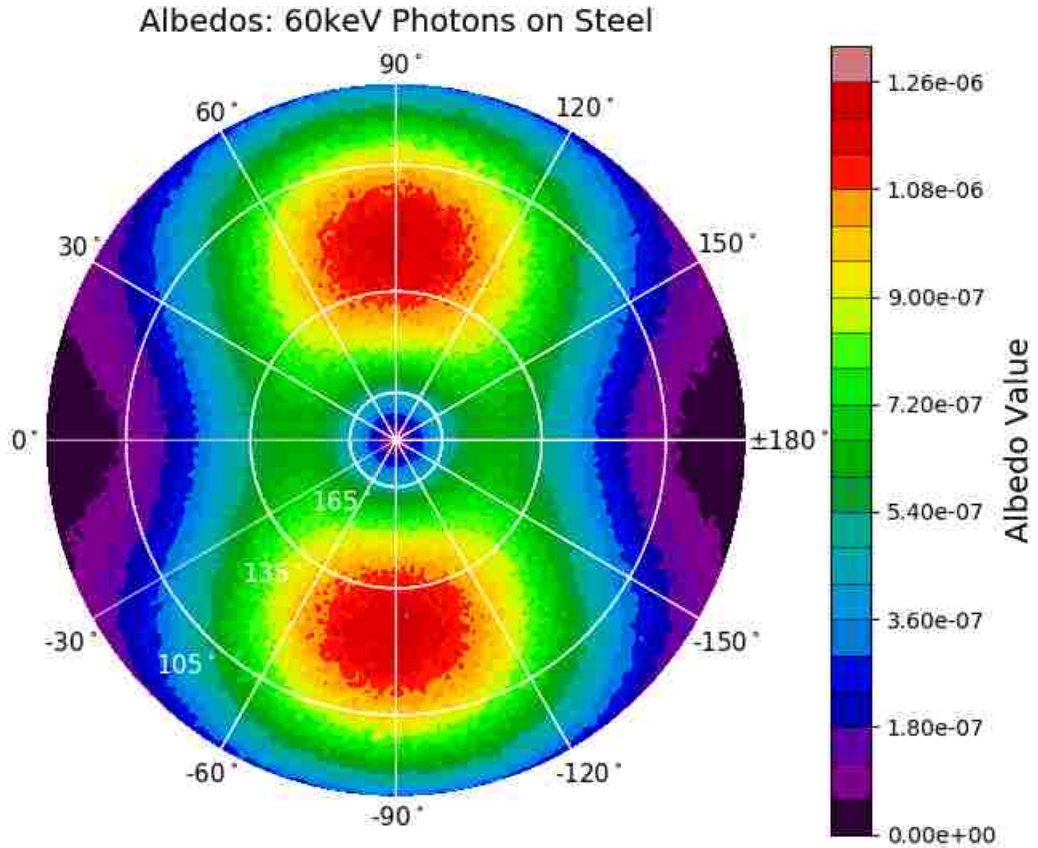

Figure C.49. Albedos for a beam of 60 keV polarized x-rays incident on a slab of steel.

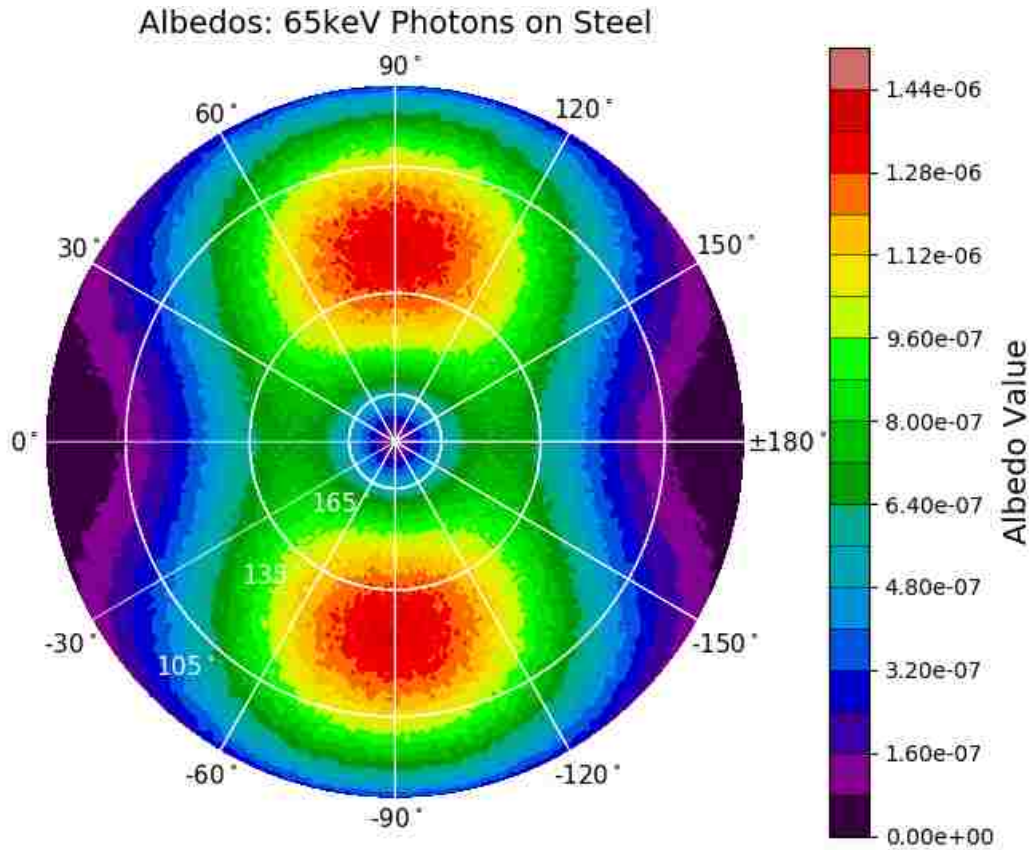

Figure C.50. Albedos for a beam of 65 keV polarized x-rays incident on a slab of steel.

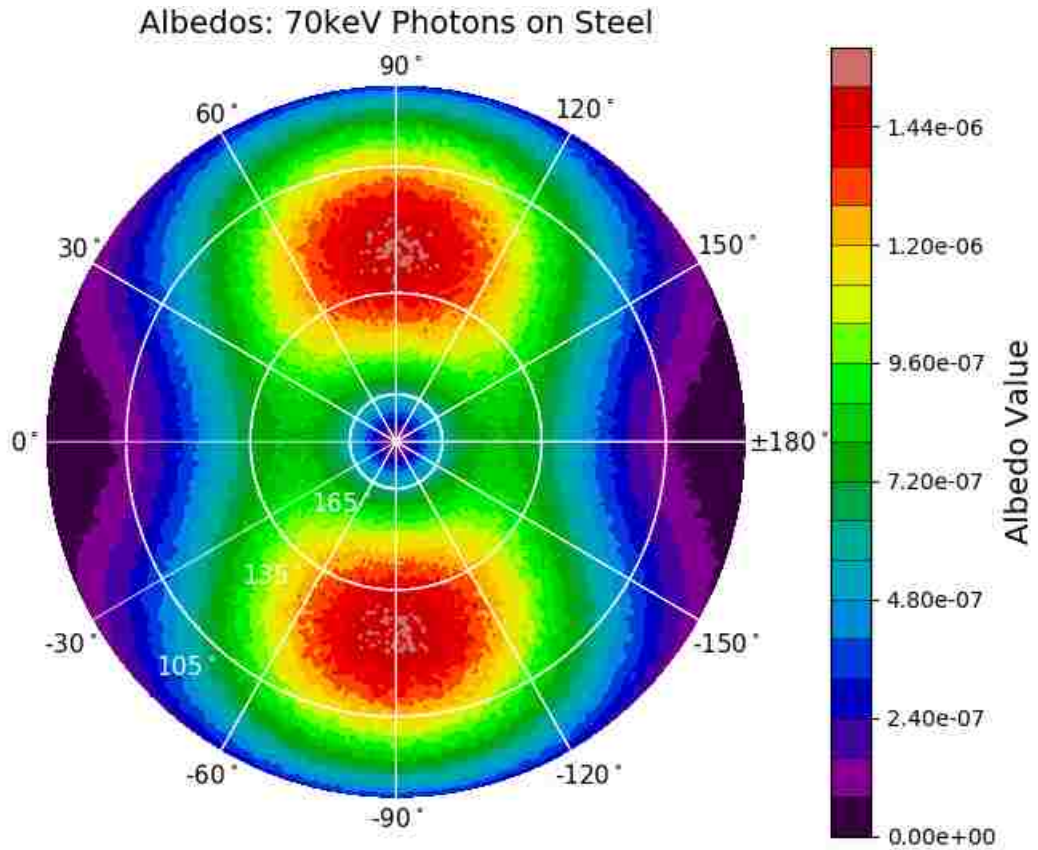

Figure C.51. Albedos for a beam of 70 keV polarized x-rays incident on a slab of steel.

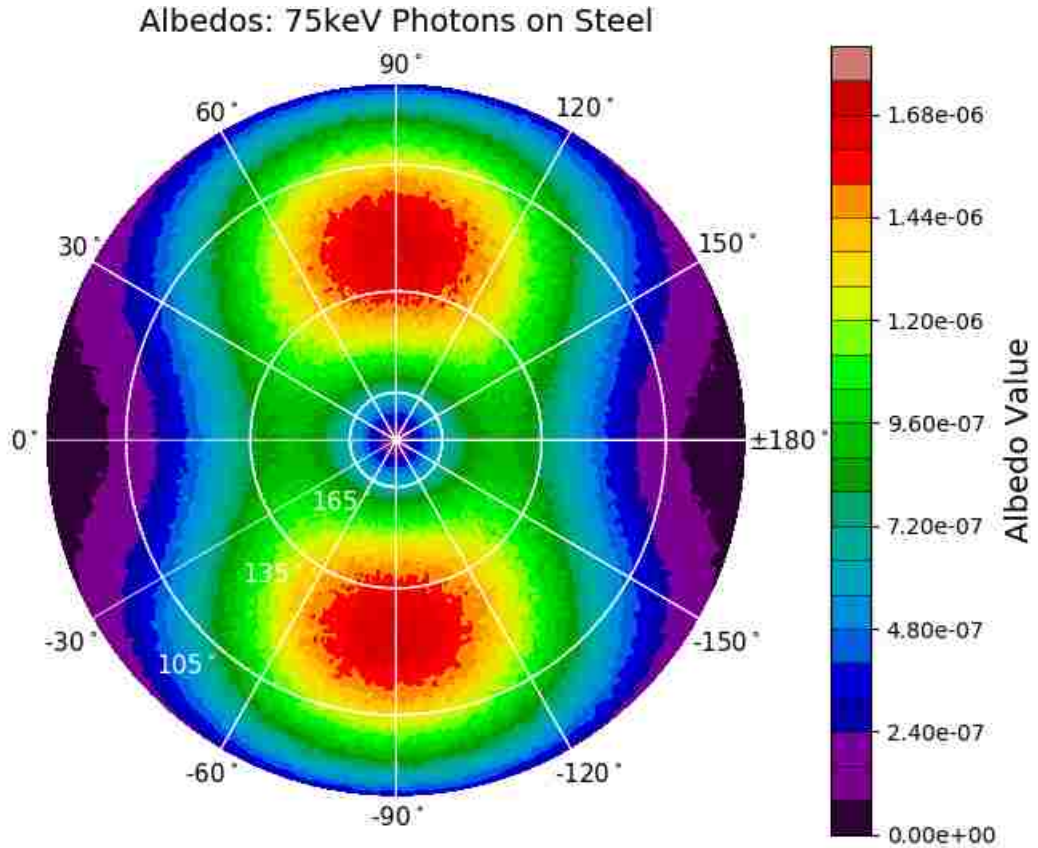

Figure C.52. Albedos for a beam of 75 keV polarized x-rays incident on a slab of steel.

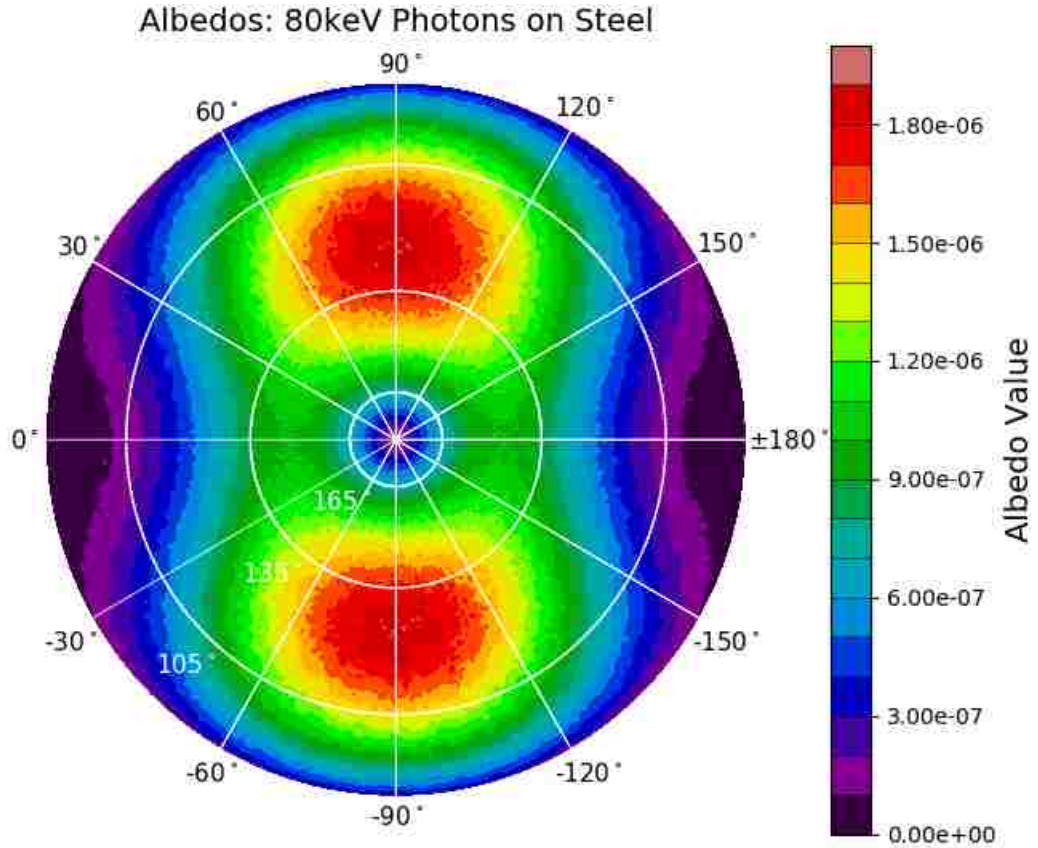

Figure C.53. Albedos for a beam of 80 keV polarized x-rays incident on a slab of steel.

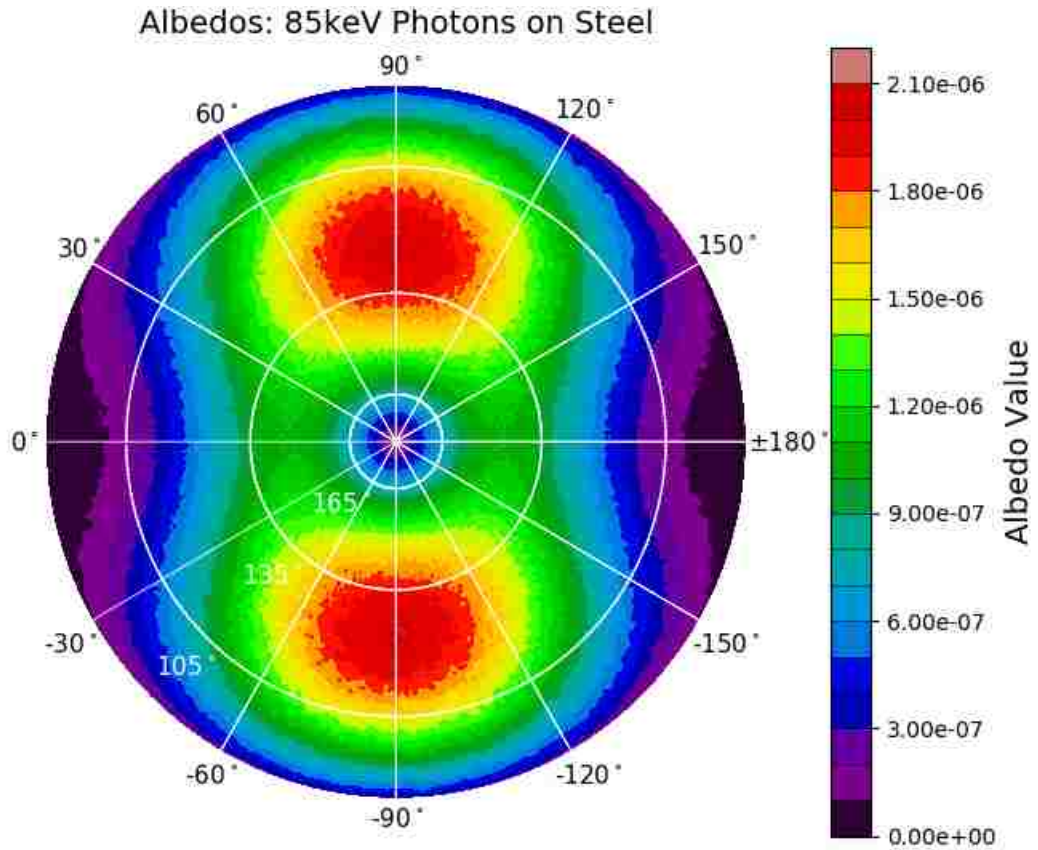

Figure C.54. Albedos for a beam of 85 keV polarized x-rays incident on a slab of steel.

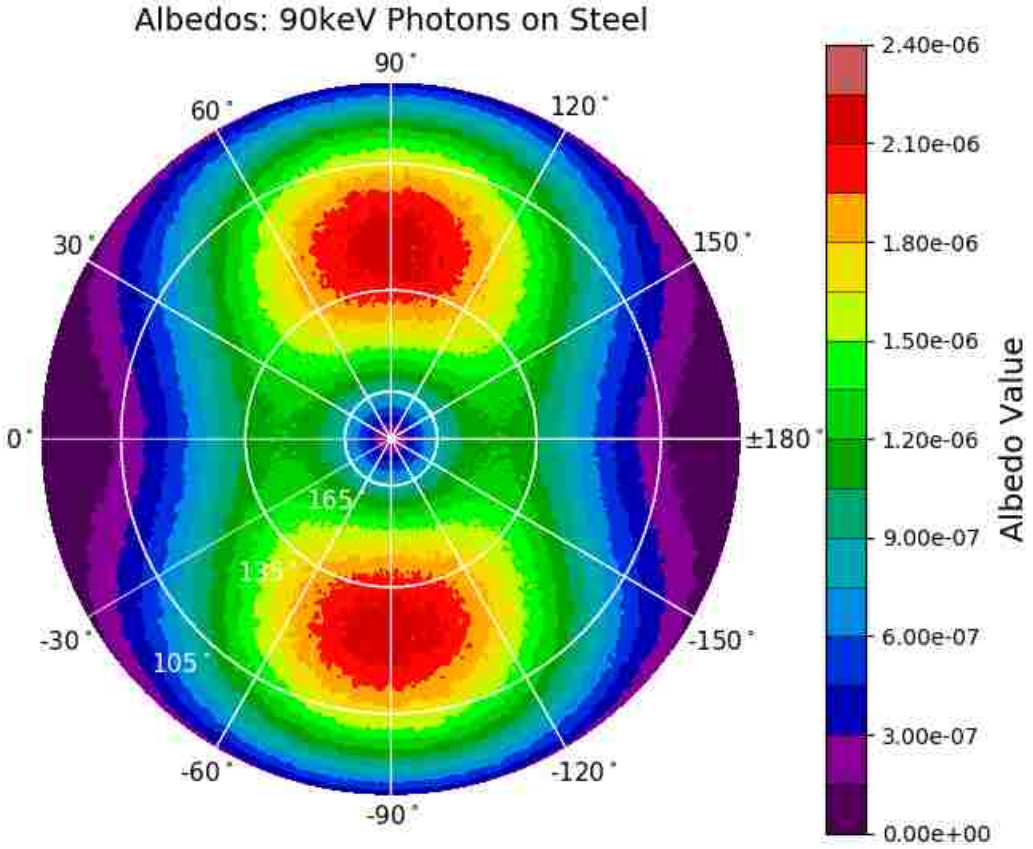

Figure C.55. Albedos for a beam of 90 keV polarized x-rays incident on a slab of steel.

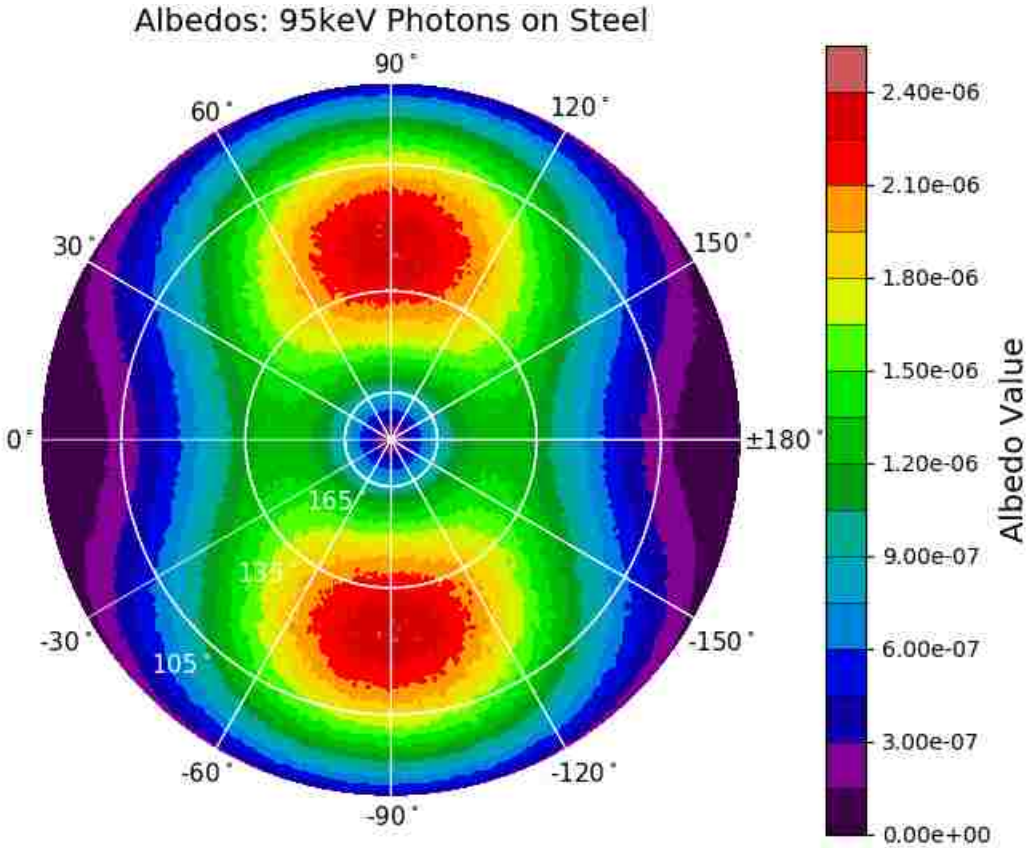

Figure C.56. Albedos for a beam of 95 keV polarized x-rays incident on a slab of steel.

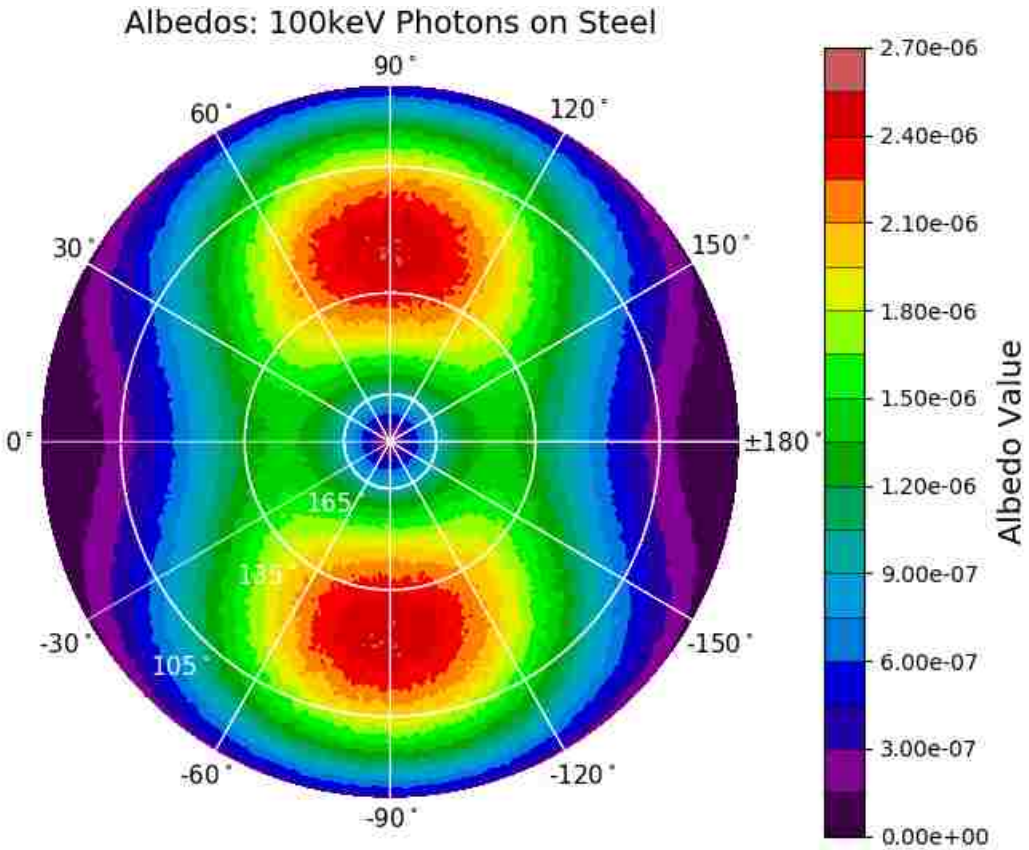

Figure C.57. Albedos for a beam of 100 keV polarized x-rays incident on a slab of steel.

References

Agostinelli, S., et al. (2003). "Geant4—a simulation toolkit." Nuclear Instruments and Methods in Physics Research Section A: Accelerators, Spectrometers, Detectors and Associated Equipment 506(3): 250-303.

Attix, F. H. (1986). Introduction to Radiological Physics and Radiation Dosimetry. New York, Wiley.

Berger, M. J., Hubbell, J. H., Seltzer, S. M., Chang, J., Coursey, J. S., Sukumar, R., Zucker, D. S., and Olsen, K. (2010), XCOM: Photon Cross Section Database (version 1.5). [Online] Available: http://physics.nist.gov/xcom [2019, March 20]. National Institute of Standards and Technology, Gaithersburg, MD.

Cember, H. and Johnson, T. E. (2009). Introduction to Health Physics. New York, McGraw-Hill Education / Medical.

Dong, X., et al. (2010). Multithreaded Geant4: Semi-automatic Transformation into Scalable Thread-Parallel Software, Berlin, Heidelberg, Springer Berlin Heidelberg.

Geant4 Collaboration, (2015) Geant4 User's Guide for Application Developers, Version: geant4 10.2. 4 December 2015.

Khan, F. M. and J. P. Gibbons (2014). The Physics of Radiation Therapy. Philadelphia, PA, Lippincott Williams & Wilkins/Wolters Kluwer.

Knights, P., et al. (2018). "Studying the effect of polarisation in Compton scattering in the undergraduate laboratory." European Journal of Physics 39(2): 025203.

Knoll, G. F. (2010). Radiation Detection and Measurement. Hoboken, N.J., John Wiley.

Matthews, K. (2019). Private communication, April 18, 2019.

NCRP (1993). National Council on Radiation Protection and Measurements. Limitation of Exposure to Ionizing Radiation, NCRP Report No. 116 (National Council on Radiation Protection and Measurements, Bethesda, Maryland).

NCRP (2003). National Council on Radiation Protection and Measurements. Radiation Protection for Particle Accelerator Facilities, NCRP Report No. 144 (National Council on Radiation Protection and Measurements, Bethesda, Maryland).

NCRP (2004). National Council on Radiation Protection and Measurements. Structural Shielding Design for Medical X-Ray Imaging Facilities, NCRP Report No. 147 (National Council on Radiation Protection and Measurements, Bethesda, Maryland).

NCRP (2005). National Council on Radiation Protection and Measurements. Structural Shielding Design and Evaluation for Megavoltage X- and Gamma-Ray Radiotherapy Facilities, NCRP Report No. 151 (National Council on Radiation Protection and Measurements, Bethesda, Maryland).

Rohatgi, A. (2012) WebPlotDigitalizer: HTML5 based online tool to extract numerical data from plot images. Version 4.1 URL http://arohatgi.info/WebPlotDigitizer/ (accessed on February 2019).

Vita

Bethany Broekhoven grew up in a small suburb of New Orleans, Louisiana. She attended Louisiana State University and received her Bachelor of Science degree in physics in 2013 along with a minor in mathematics. After graduation, Bethany worked as a research specialist for three years before returning to LSU to receive her Master of Science degree from the Medical Physics and Health Physics Program. Upon successful completion of her degree requirements, Bethany plans to graduate in the summer of 2019 and continue her medical physics training over the next two years in the therapeutic medical physics residency program at the Medical University of South Carolina.